TiO$_2$ NANOTUBE BASED DYE-SENSITISED SOLAR CELLS

By

FRANSCIOUS RICCARDO CUMMINGS

Submitted in fulfilment of the requirements of the degree of
PhD (Physics) in the Department of Physics,
University of the Western Cape

Supervisor: Prof D. Knoesen, University of the Western Cape

September 2012

To My Loving Family

ACKNOWLEDGEMENTS

I would like to thank the following people and organisations who have guided and assisted me through this journey and without their advice this thesis would not have been possible.

Prof. Dirk Knoesen (Department of Physics, University of the Western Cape), who acted as supervisor during this study, for his constant encouragement and interest in my progress.

The staff of the Physics Department, University of the Western Cape, for their support and encouragement.

The Energy and Processes Competence Area of the CSIR, who granted me the opportunity to conduct research at one of the most outstanding research institutes.

To my immediate, extended family and friends, for their encouragement and support:

Firstly to my wife Melanie and children, Caleb and Miley, I would like to say thank you for your love, patience and understanding through this journey – I love you!

To my mother and grandmother for their believe in me and always inspiring me to greater things!

To the rest of my family - Barry, Merle, Christina, Zonika, Candice, Tessa, Rico, Joeharr, Gail, Carmen, Lee-Ann, Junior, Shannique, Setta, Janera, Lionel, Medwin, Clayton, Candice, Jerome, Ruanita, Rupert, Sarah, Elizabeth, Walter, Emile, and the rest of the family for being there in my time of need when your support was truly needed.

To my closest friends and colleagues, Christopher, Gerald, David, Mathew, Minnie and Rochel – thank you for being very good friends.
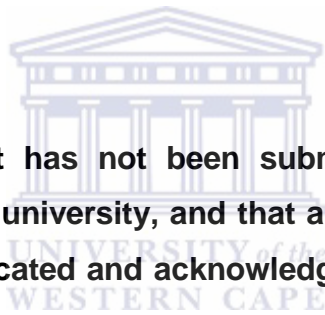
To my Creator and God Almighty!

Thank You!

DECLARATION

I declare that

"TiO$_2$ NANOTUBE BASED DYE-SENSITISED SOLAR CELLS"

is my own work, that it has not been submitted for any degree or examination in any other university, and that all the sources I have used or quoted have been indicated and acknowledged by means of complete references.

Franscious Riccardo Cummings   **September 2012**

Signature: ……………………..

KEY WORDS

TiO$_2$ NANOTUBE BASED DYE-SENSITISED SOLAR CELLS

FRANSCIOUS RICCARDO CUMMINGS

TiO$_2$ Nanotubes

Dye-sensitised Solar Cells

Photovoltaics

Electrochemical Anodisation

Sol-Gel Deposition

Renewable Energy

Core-shell Nanostructures

Materials Science

Opto-electronic Properties

Morphology

Electron Charge Transfer

Crystallinity

SYMBOLS

TiO$_2$ NANOTUBE BASED DYE-SENSITISED SOLAR CELLS

FRANSCIOUS RICCARDO CUMMINGS

c-Si – Single Crystalline Silicon

poly-S – Polycrystalline Silicon

a-Si – Amorphous Silicon

Redox – Reduction-Oxidation Reaction
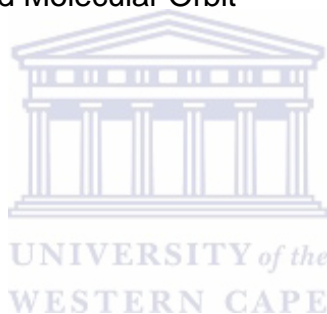
HOMO – Highest Occupied Molecular Orbit

LUMO – Lowest Unoccupied Molecular Orbit

E_g – Optical Bandgap

E_{VB} – Valence Band

E_{CB} – Conduction Band

E_F^n – Quasi-Fermi Level

IPCE – Incident-Photon-Current-Conversion-Efficiency

η_{lh} (LHE) – Light Harvesting Efficiency

η_{ei} – Electron Injection Efficiency

η_{et} – Electron Transport Efficiency

η_{ect} - Electron Collection Efficiency

AM 1.5 – Global Air Mass 1.5

f_g – Anodisation Growth Factor

α-Al$_2$O$_3$ – Corundum Alumina

λ– wavelength

d – interplanar spacing

ɵ - Bragg angle

FWHM/Γ_0/B – full width at half maximum

N_{surf} – concentration of surface atoms

N_{bulk} – concentration of bulk atoms

σ_{surf} - N_{surf}/ N_{bulk}

$\omega(q)$ – phonon dispersion curve

$C(0, q)$ – Fourier coefficients

$\hbar$ – h/2π

k – momentum vector

$Z(\omega)$ – complex impedance, $Z(\omega) = Z_{Re} - jZI_m$ where $j = \sqrt{-1}$

R_s – series resistance

R_{ct} – charge transfer resistance

Z_w – Warburg Impedance

I_{sc} – short circuit current density

I_{MP} – maximum current point

V_{oc} – open circuit voltage

V_{MP} – maximum voltage point

FF – fill factor

P_{max} – maximum power point

η – photon-current conversion efficiency

I_{sat} – saturation current

e_0 – electron charge

m_D – ideality factor

k_B – Boltzmann constant

I_{shunt} – shunt current

R_{sh} – shunt resistance

FIGURE & TABLE CAPTIONS

TiO$_2$ NANOTUBE BASED DYE-SENSITISED SOLAR CELLS

FRANSCIOUS RICCARDO CUMMINGS

Figure 1.1:   South Africa's primary energy supply sources as captured in 2004 [1.1]

Figure 1.2:   (a) Individual PV cells interconnected to form a module and (b) example of a solar farm employing PV modules, connected to form a PV array for high power applications [1.7]

Figure 1.3:   Dye-sensitised solar cells in operation at TIMO Technologies®, South Korea

Figure 1.4:   Schematic representation of the structure of a DSC [1.21]

Figure 1.5:   Energy scheme and electron transfer paths of a dye solar cell [1.22]

Figure 1.6:   Schematic representation of the different interfaces present within a DSC [1.23]

Figure 1.7:   Molecular structure of (a) N3 dye bonded to the TiO$_2$ surface and (b) N719 (or black) dye commonly used in DSCs [1.26, 1.27]

Figure 1.8:   SEM micrographs of the TiO$_2$ nanotubes synthesised by Gong et al [1.40]

Figure 1.9:   Illustration of the interfacial charge-transfer processes occurring at the nanostructured TiO$_2$/dye/electrolyte interface of DSSC

and the employment of a Al_2O_3 insulating layer to retard the recombination reactions between the electrons in the TiO_2 conduction band and holes present in the dye and electrolyte [1.45]

UNIVERSITY *of the*
WESTERN CAPE

ABSTRACT

TiO$_2$ NANOTUBE BASED DYE SENSITISED SOLAR CELLS

FRANSCIOUS RICCARDO CUMMINGS

Ph.D. Thesis, Department of Physics, University of the Western Cape

The first report of a functioning photo-electrochemical solar cell in 1991 attracted a lot of interest from scientists and industrial groups. From an industrial point of view these so-called dye-sensitised solar cells (DSCs) offered the promise of moderate efficiency devices at ultra-low costs, owing to simple processing methods and the use of inexpensive materials. From an academic viewpoint, DSCs raised important scientific questions around the fundamental processes governing their operation and how these processes influence the photon-to-electron conversion efficiency of the cell. Major successes have since been achieved in understanding these processes, however the conversion efficiency of the best manufactured DSCs remains around 11%, significantly lower than that of their silicon photovoltaic counterparts.

In traditional DSCs, charge generation is achieved by ultrafast electron injection from a photo-excited ruthenium-based dye molecule into the conduction band of a film of TiO$_2$ nanoparticles, subsequent dye regeneration by an I^-/I_3^- containing redox electrolyte and finally hole transportation to a platinum-coated counter electrode.

The low DSC efficiencies are attributed to scattering of electrons at the interface between two TiO_2 nanoparticles leading to recombination with holes present in the redox electrolyte. Recent studies have shown that the application of films of highly ordered TiO_2 nanotubes instead of nanoparticles has the potential to improve the overall conversion efficiency of the cell. This is ascribed to the one-dimensional nature of nanotubes, which provides a linear transportation route for electrons generated during operation of the DSC. As a result the recombination probability of the electrons with nearby holes in the device is decreased.

This work investigated the synthesis of Al_2O_3-coated TiO_2 nanotubes via the anodisation technique for application in DSCs. TiO_2 nanotube arrays with an average length of 15 µm, diameter of 50 nm and wall thickness of 15 nm were synthesised via anodisation using an organic neutral electrolyte consisting of 2 M H_2O + 0.15 M NH_4F + ethylene glycol (EG) at an applied voltage of 60 V for 6 hours. In addition, scanning electron microscope (SEM) micrographs showed that anodisation at these conditions yields nanotubes with smooth walls and hexagonally shaped, closed bottoms.

X-ray diffraction (XRD) patterns revealed that the as-anodised nanotubes were amorphous and as such were annealed at 450 °C for 2 hours in air at atmospheric pressure, which yielded crystalline anatase TiO_2 nanotubes. High-resolution transmission electron microscope (TEM) images revealed that the nanotube walls comprised of individual nano-sized TiO_2 crystallites. Photoluminescence (PL) spectroscopy showed that the optical properties, especially the bandgap of the TiO_2 nanotubes are dependent on the

crystallinity, which in turn was dependent on the structural characteristics, such as the wall thickness, diameter and length. The PL measurements were supplemented by Raman spectra, which revealed an increased in the quantum confinement of the optical phonon modes of the nanotubes synthesised at low anodisation voltages, consequently yielding a larger bandgap

The annealed nanotubes were then coated with a thin layer of alumina (Al_2O_3) using a simple sol-gel dip coating method, effectively used to coat films of nanoparticles. Atomic force microscopy (AFM) showed that the average nanotube diameter increased post sol-gel deposition, which suggests that the nanotubes are coated with a layer of Al_2O_3. This was confirmed with HR-TEM, in conjunction with selected area electron diffraction (SAED) and XRD analyses, which showed the coating of the nanotube walls with a thin layer of amorphous Al_2O_3 with a thickness between 4 and 7 nm. Ultraviolet-visible (UV-vis) absorbance spectra showed that the dye-adsorption ability of the nanotubes are enhanced by the Al_2O_3 coating and hence is a viable material for solar cell application.

Upon application in the DSC, it was found by means of photo-current density – voltage (I – V) measurements that a DSC fabricated with a 15 μm thick layer of bare TiO_2 nanotubes has a photon-to-light conversion efficiency of 4.56%, which increased to 4.88% after coating the nanotubes with a layer of alumina. However, these devices had poorer conversion efficiencies than bare and Al_2O_3-coated TiO_2 nanoparticle based DSCs, which boasted with efficiencies of 6.54 and 7.26%, respectively. The low efficiencies of the TiO_2 nanotube based DSCs are ascribed to the low surface area of the layer of

nanotubes, which yielded low photocurrent densities. Electrochemical impedance spectroscopy (EIS) showed that the electron lifetime in the alumina coated nanotubes are almost 20 times greater than in a bare layer of nanoparticles. In addition, it was also found that the charge transfer resistance at the interface of the TiO_2/dye/electrolyte is the lowest for an Al_2O_3-coated TiO_2 layer.

September 2012

CONTENTS

CHAPTER ONE
Background

1.1 Introduction

South Africa's primary energy supply is dominated by coal, as statistically captured in Figure 1.1 by the South African Department of Energy [1.1]. This energy mix can largely be explained by the fact that South African coal is relatively abundant, of high quality and inexpensive when compared to international coals. However, the majority of the local high quality coals are exported off-shore and the low grade coals used in local power stations for power generation, resulting in increased levels of pollution. A pending energy crisis is looming large for the country as the high quality coal reserves for electricity generation are increasingly becoming limited. Added to the increasing health risks and negative environmental impact associated with traditional coal and crude-oil based power generation, it can be seen that South Africa are in urgent need of clean and inexpensive alternative energy sources to diversify its energy mix.

Figure 1.1 shows that only 8% of South Africa's total energy supply originates from renewable energy sources even though these avenues potentially provide an unlimited amount of clean energy. The South African government has earmarked hydro and solar renewable energy sources as possible future large-scale providers of energy for rural areas, where a great percentage of the South African population [1.1, 1.2] lives. However, with the

generally low annual rainfall (average of 450 mm compared with a world average of 860 mm) [1.3], as well as the constant droughts in the interior western regions of the country, utilisation of hydro-electric power generation methods remains limited and generally not well-developed. On the other hand, due to its abundant sunshine South Africa has the potential to become one of the global giants in exploiting solar energy, not only for household, but also industrial application.
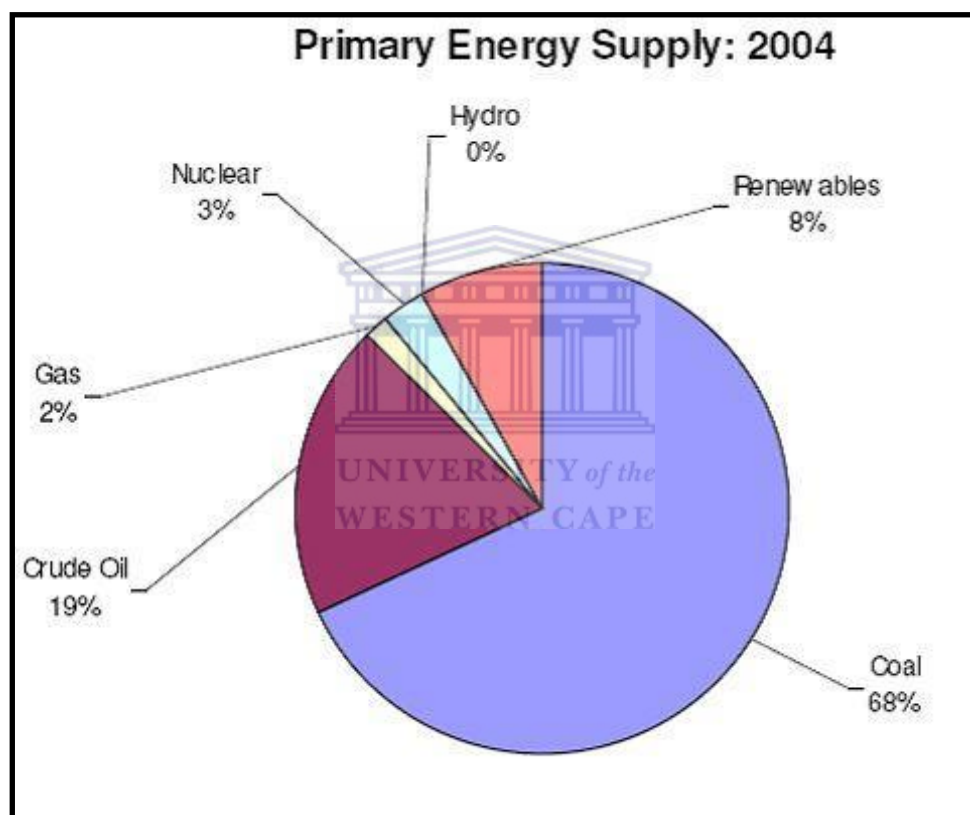
Figure 1.1: South Africa's primary energy supply sources as captured in 2004 [1.1]

The average daily solar radiation in South Africa varies between 4.5 and 6.5 kWh/m^2, which is better than that of the United States with an average radiation of 3.6 kWh/m^2 and Europe and the United Kingdom of 2.5 kWh/m^2 [1.2, 1.4]. With this in mind, it make sense that photovoltaic (PV) research and

development (R&D) requires great attention for it provides the most straightforward method of converting sunlight into electrical energy, requiring less manpower and manufacturing [1.5].

1.2 Photovoltaics

A basic definition of a photovoltaic (PV) device is that it converts light energy into electrical energy and consists primarily of a photovoltaic (or solar) cell and peripheral devices, such as a battery. Typical solar cells produce less than 3 watts at approximately 0.5 volt direct current (DC), therefore in practice they are connected in series-parallel configurations (known as modules) to produce enough power for everyday applications. For high-power applications these modules are connected to form photovoltaic arrays, or hybrid systems, as shown in Figure 1.2 [1.5 - 1.7].
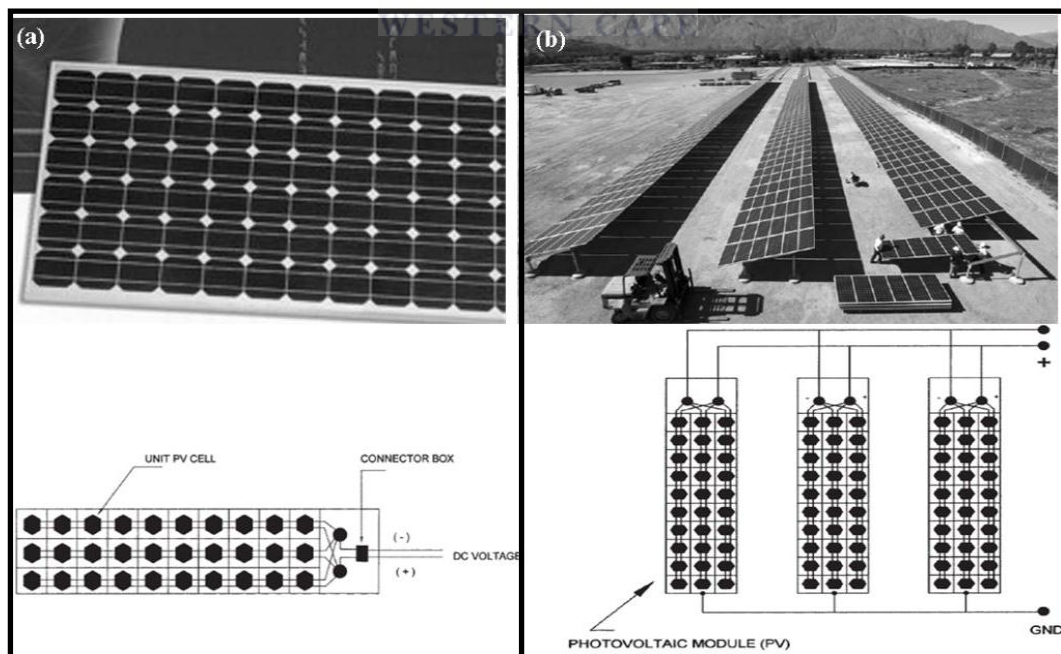
Figure 1.2: (a) Individual PV cells interconnected to form a module and (b) example of a solar farm employing PV modules, connected to form a PV array for high power applications [1.7]

3

Current commercialised solar cell technologies include the traditional single-crystalline (c-Si), poly-crystalline (poly-Si), the less expensive amorphous silicon (a-Si) cells and thin film solar cells such as copper-indium-gallium-selenide (CIGS) cells. However, the main obstacles faced by these technologies for large-scale commercialisation are their high manufacturing costs, relatively low efficiency compared to coal and nuclear power generating methods and the lack of long-term stability of the underlying solar cells [1.5]. In addition, some traditional solid state solar cells employ hazardous materials, such as gallium arsenide (GaAs), which pose risks for the environment within which they are operated [1.7]. Hence the bulk of PV R&D over the last two decades focused on improving efficiencies and long-term stability of the solar cells, while utilising less-volatile materials and keeping the cost of manufacturing at a minimum.

1.3 New Generation Photovoltaics

A major breakthrough in cost-reduction of solar cells was realised in 1991 with the first report of a functioning photo-electrochemical solar cell, based on the dye sensitisation of porous, nanocrystalline titanium dioxide (TiO_2) films by O'Regan and Grätzel [1.8]. Needless to say, this breakthrough attracted a lot of interest from both industry and the scientific community. From an industrial point-of-view these so-called dye-sensitised solar cells (DSCs) or Grätzel cells (named after its inventor, Prof. Michael Grätzel) offered the promise of moderate efficiency devices at ultra-low costs. From an academic stance, DSCs raised important questions around the fundamental processes governing their operation [1.9].

Firstly, much of the theory developed to describe the photo-electrochemical behaviour of bulk semiconductors could not be applied directly to the nanocrystalline TiO_2 films present within the DSC. For instance, the formation of a depletion layer as well as bending of the electronic bands of these nanocrystalline materials were considered highly unlikely, owing to their exceedingly small crystallite sizes. Secondly, the relationship between the surface area of the TiO_2 nanoparticle film and the reported photovoltage values (~ 700 mV) also intrigued researchers. Although the large surface area of the film could well account for the observed photocurrent, it could not explain the magnitude of the observed photovoltage. Finally, scientists battled to understand how electrons could move through insulating particles of TiO_2 to a collecting electrode without undergoing significant recombination, thereby markedly reducing the PV response of the cell [1.9 – 1.11].

Today, 20 years onwards and with the advent of nanoscience and nanotechnology, much progress has been made in advancing the understanding of the science around the operation of the DSC. So much so, that several industrial companies across Europe [1.12– 1.14] and Pacific-Asia [1.15, 1.16] currently actively work towards the commercialisation of Grätzel cells. However, the exact physics and chemistry at the different interfaces within the cell remain a topic of debate [1.9] and currently pose as the biggest challenge in manufacturing DSCs with efficiencies to rival commercialised crystalline solar cells for use in large scale power generation plants. Figure 1.3 shows an exhibition stand of DSCs (both modules and small-scale "master-plates") at TIMO Technologies®, South Korea, during a visit to the company in 2009.

Figure 1.3: Dye-sensitised solar cells in operation at TIMO Technologies®, South Korea

Potentially DSCs can be produced at a cost of less than 1 U.S.$/peak watt [1.17] compared to 4.8 U.S.$/peak watt for silicon based solar cells [1.18] and yield an energy payback life-time of 3 months compared to 4 years for most crystalline silicon technologies. As a result of the photo-electrochemical nature of DSCs, a whole range of complementary and niche market applications, such as small-scale consumer electronics [1.19] and building integrated photovoltaics (BIPV) are envisaged for these novel solar cells [1.20]. Thus it can be seen that upon their commercialisation, DSCs will add a whole new dimension to the photovoltaic industry.

1.4 Operating Principle of the Dye-sensitised Solar Cell

Figure 1.4 shows a schematic representation of the structure of a traditional DSC [1.21]. The heart of the cell comprises of a mesoporous film of anatase TiO_2 nanoparticles (usually between 10 and 20 µm thick) deposited on a transparent conductive oxide (TCO) substrate. The TiO_2 nanoparticles act as the transport medium for electrons from their point of generation to the TCO. A monolayer of a ruthenium (Ru) dye complex is chemically adsorbed onto the TiO_2 surface to act as the light absorber, or sensitiser. The dye-sensitised TiO_2 nanoparticle film then forms the anode (working electrode) of the cell.
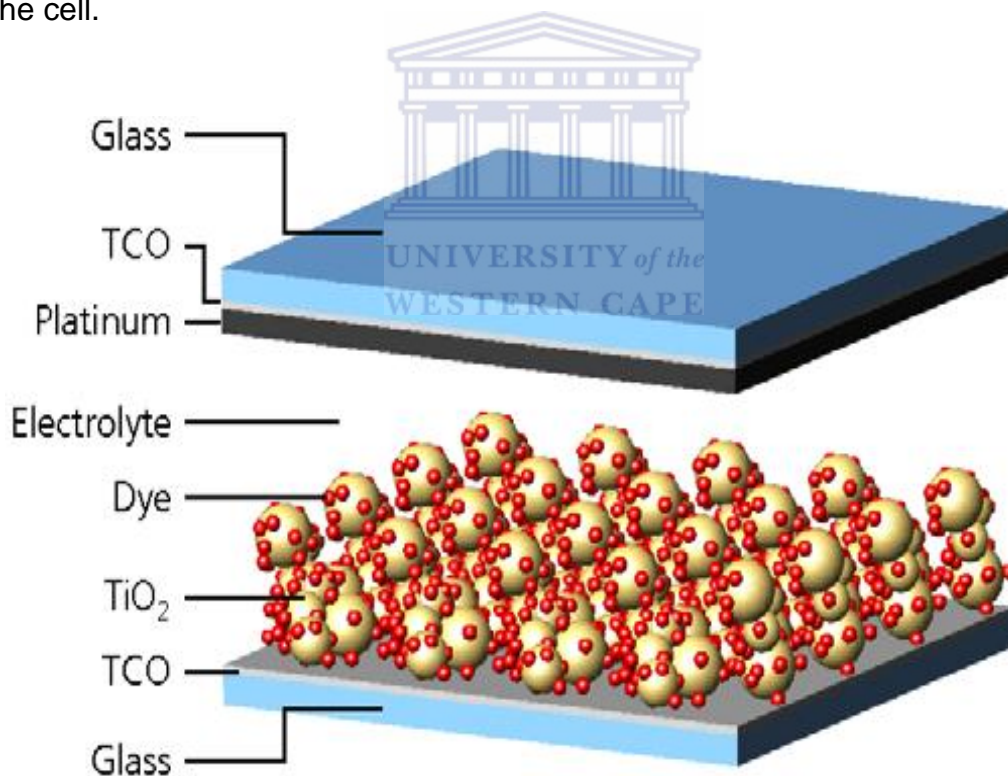
Figure 1.4:   Schematic representation of the structure of a DSC [1.21]

The cathode (counter electrode) comprises of a thin film of platinum (Pt) deposited onto a TCO/glass substrate. The two electrodes are then sealed together and filled with an electrolyte solution containing an iodide/tri-iodide (I^-/I_3^-) red-ox couple, which acts as the hole conducting medium.

Figure 1.5 shows the energy diagram and electron transfer routes of the DSC under light illumination [1.22]. During operation, light is absorbed by the dye molecules, resulting in the excitation of an electron from the highest occupied molecular orbital (HOMO) to the lowest unoccupied molecular orbital (LUMO) within the molecule. Thus the dye molecule is excited from its ground-state (denoted D in Figure 1.5) to an excited state D*. TiO_2 is a semiconductor with a large band gap of 3.2 eV (corresponding wavelength of 390 nm) and thus visible light is not absorbed by the TiO_2 film. Direct absorption of UV-light is unwanted, since the created holes in the valence band (E_{VB}) of the TiO_2 are highly reactive and produce side reactions in the electrolyte, which are destructive for the cell during long term operation [1.22].

The excited electron is then injected into the conduction band (E_{CB}) of the TiO_2 film and diffuses through the interconnected network of nanoparticles to reach the TCO by a random walk process involving multiple trapping and detrapping via states in the bandgap of the TiO_2 [1.23, 1.24]. In Figure 1.5 E_F^n denotes the quasi-Fermi level of the electrons in the conduction band of the TiO_2 and can be interpreted as the displacement of the Fermi level away from equilibrium, caused by the external photon excitation of the device. Upon reaching the TCO, the electron then conducts through the external load towards the counter electrode.
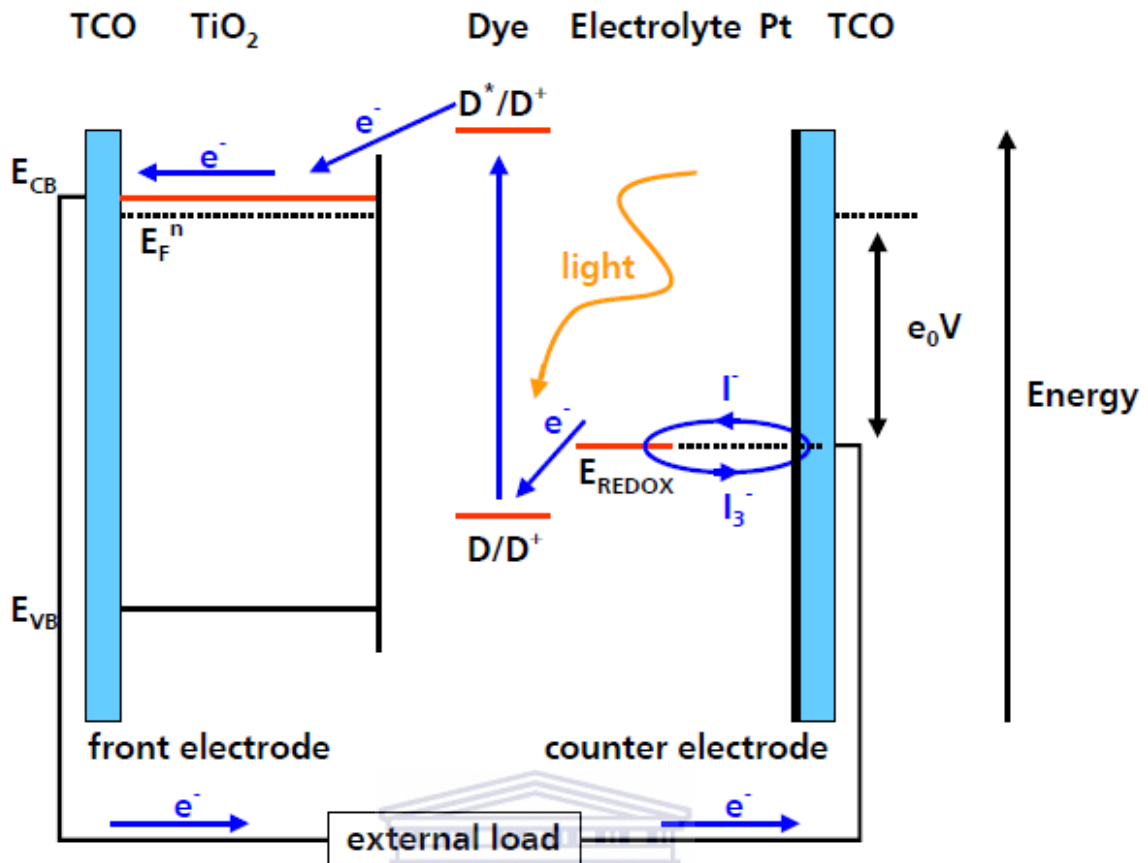
Figure 1.5: Energy scheme and electron transfer paths of a dye solar cell [1.22]

The Pt layer at the counter electrode acts as a catalyst and ignites the redox reactions when the electrons reach the counter electrode. The oxidised dye molecule (D^+) is reduced to its ground state (D) by the negatively charged I^- ions of the electrolyte during the following reaction,

$$2D^+ + 3I^- \rightarrow I_3^- + 2D \tag{1.1}$$

The positively charged tri-iodide ions, I_3^- then diffuses to the Pt counter electrode to regenerate the iodide ions via the reaction

$$I_3^- + 2e^- \rightarrow 3I^- \tag{1.2},$$

thereby completing the electrical circuit. The maximum voltage produced by the DSC (i.e. the open-circuit voltage, denoted e_0V in Figure 1.5) is the

9

difference between E_F^n and E_{REDOX}, the redox potential of the I^-/I_3^- redox couple and is typically between 700 and 800 mV.

1.5 Factors Limiting Cell Performance

The photocurrent produced by a DSC is dependent on the total external quantum efficiency of the cell, called the incident-photon-current-conversion-efficiency (IPCE) and is given by the product of the efficiencies for light harvesting (η_{lh}), electron injection from the dye to the TiO_2 conduction band (η_{ei}), electron transport through the TiO_2 nanostructured film (η_{et}) and electron collection at the TCO (η_{ec}):

$$IPCE = \eta_{lh} \times \eta_{ei} \times \eta_{et} \times \eta_{ec} \tag{1.3}$$

Figure 1.6 sketches a graphical image of the IPCE process. In total there are four areas of importance that provide possible recombination pathways within the DSC, namely the TCO/TiO_2, TiO_2/dye, dye/electrolyte and the electrolyte/Pt interfaces as shown in Figure 1.6. The efficiency for hole collection at the platinised counter electrode (subsequently named hole-conversion efficiency, or HCE) is given by a similar relation to that of (1.3) except that there is no light harvesting term involved, as shown in Figure 1.6 [1.23]. For devices through which the light is shone from the Pt counter electrode side (so-called back-side illuminated DSCs), it is known that certain species of electrolyte as well as the thin Pt layer on the TCO scatter and absorb the incident light, which negatively impacts the light harvesting efficiency (LHE) at the TiO_2/dye interface [1.24]. The product of IPCE and HCE gives the total device efficiency measured during $I - V$ curve

characterisation and thus optimisation of the individual processes that contribute to both IPCE and HCE is paramount to achieving high efficiency devices. In the following sub-sections the factors influencing each of the efficiencies comprising the IPCE and HCE will be discussed in detail. This is done in order to shed some light on reasons behind the generally low device efficiencies often reported for DSCs.
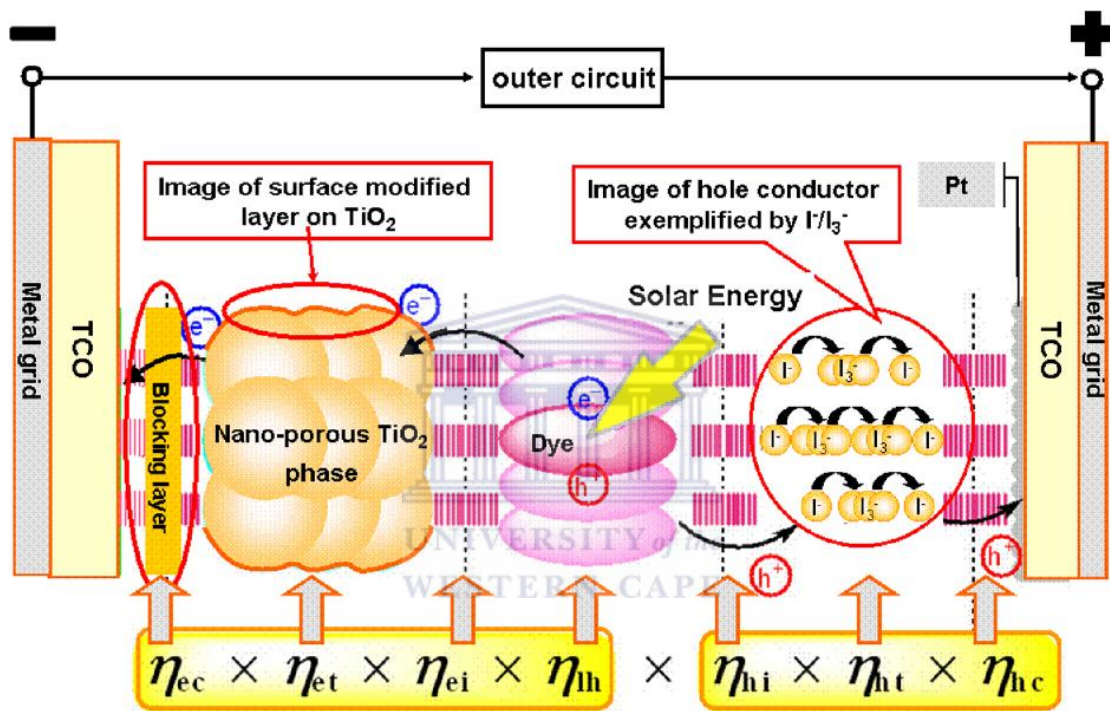
Figure 1.6: Schematic representation of the different interfaces present within a DSC [1.23]

1.5.1 Light Harvesting Efficiency of the DSC

The LHE (η_{lh} in equation 1.3) within the DSC is highly dependent on the type of sensitiser (dye) employed. The ideal sensitiser for converting standard global air mass (AM) 1.5 sunlight to electricity should absorb all light below a threshold wavelength of about 920 nm. In addition, the sensitiser must also carry attachment groups such as carboxylate or phosphonate to firmly attach it to the dangling oxygen atoms on the TiO_2 nanoparticle surface. Upon excitation it should inject electrons into the TiO_2 conduction band with a quantum yield of unity and the energy level of the excited state (LUMO) should be well matched with the conduction band edge of the TiO_2 to minimise energy losses during the electron injection reaction. An excited dye molecule may directly relax back into its ground state without injection of an electron into the TiO_2 bandgap. This process is negligible, however, as it has been shown that injection is about 1000 times faster than relaxation [1.25]. The redox potential of the sensitiser should be sufficiently high that it can be regenerated via electron donation from the redox electrolyte and finally, the sensitiser should be stable enough to sustain about 10^8 turnover cycles corresponding to about 20 years of exposure to natural light [1.26].

The best photovoltaic performance both in terms of conversion yield and long-term stability has so far been achieved with polypyridyl complexes of ruthenium (Ru). More specifically, sensitisers with the chemical structure of the form $ML_2(X)_2$, where L stands for 2,2'-bipyridyl-4,4'-dicarboxylic acid, M is a metal and X presents a halide, cyanide, thiocyanate, acetyl acetonate, thiacarbamate or water substituent, have shown to perform the best when

incorporated within a DSC [1.25, 1.26]. For close to a decade, the Ru complex *cis*-RuL$_2$(NCS)$_2$, discovered in 1993 [1.25] and best known as N3 dye, was the paradigm for heterogeneous charge transfer sensitisers in DSCs.

The fully protonated N3 dye has absorption maxima at 518 and 380 nm, respectively and emits at 750 nm, which equates to a lifetime of 60 ns. The electron generation process within the N3 dye has metal-to-ligand charge transfer (MLCT) character. This implies that upon illumination an electron is transferred from the Ru metal to the p* orbital of the surface anchoring carboxylated bipyridyl ligand, from where it is released within femto- to picoseconds into the conduction band of TiO$_2$, thereby generating electric charges with unit quantum yield [1.28]. In 2001 the N719 or "black" dye, RuL'$_3$(NCS)$_3$, where L' is (cyanato)-2,2'2"-terpyridyl-4,4'4"-tricarboxylate, achieved a then record 10.4% (AM 1.5) solar-to-power conversion efficiency in full sunlight [1.29]. This dye has since been the most popular dye among researchers and will also be the sensitiser used throughout this study. Figure 1.7 shows the chemical structure of the N3 and N719 dye molecules, as well as the bonding of the N3 to the surface of the TiO$_2$ semiconductor.
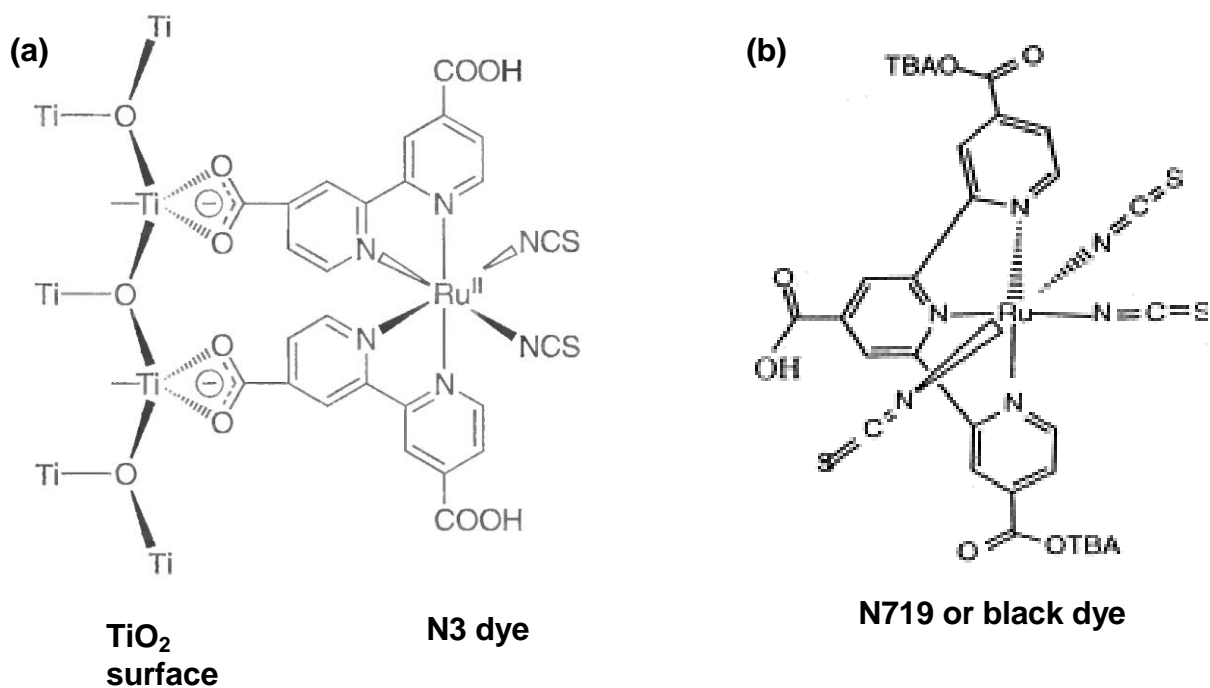
(a)

(b)

TiO$_2$ surface

N3 dye

N719 or black dye

Figure 1.7: Molecular structure of (a) N3 dye bonded to the TiO$_2$ surface and (b) N719 (or black) dye commonly used in DSCs [1.26, 1.27]
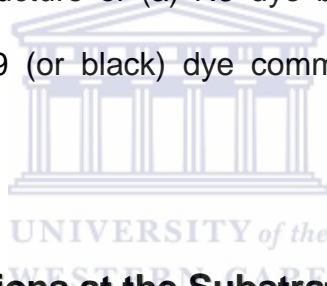
1.5.2 Interfacial Reactions at the Substrates

If the charge transfer resistance at the TCO is the same as at the counter electrode, the DSC would not operate properly. However, the charge transfer resistance at the counter electrode is reduced by many orders of magnitude by the platinum catalyst, whereas the charge transfer resistance at the TCO/electrolyte interface is sufficiently high to create a potential difference across the external load [1.22].

The electrolyte penetrates the TiO$_2$ nanostructured architecture and is also in contact with the front TCO electrode. It has been demonstrated that the fluorine-doped tin oxide (FTO) substrates must be covered by a thin,

compact layer of TiO$_2$ (called a "blocking" layer) in order to prevent efficiency loss due to electron transfer to the hole-conducting electrolyte from the FTO, which typically has a doping density in excess of 10^{20} cm^{-1} [1.30, 1.31]. Hence, modern day DSCs employ these TiO$_2$ blocking layers, as shown in Figure 1.6, to overcome charge loss at the conductive substrate.

The principle task of the counter electrode (CE) in the DSC is to reduce the hole conducting species of the electrolyte, as depicted by reaction (1.2) above [1.32]. Thus the counter electrode-electrolyte interface kinetics is an important study to pursue. At present, several CEs have been introduced such as platinised transparent CEs [1.33], carbon CEs [1.34] and conductive polymer CEs [1.35]. Similarly different electrolyte systems have been employed, however the best performing CE-electrolyte system employed today remains the platinised transparent CE in conjunction with the iodide/tri-iodide redox system. This system will also be used exclusively in this study.

1.5.3 Interfacial Reactions at the TiO$_2$/dye/electrolyte Interfaces

The extended interface between the TiO$_2$ nanoparticle film and the electrolyte solution allows for efficient light harvesting and charge carrier (electron-hole, or e-h pair) generation in the DSC. However, this extended surface area also increases the probability of recombination between the e-h pairs because the holes in the electrolyte, i.e. I$_3^-$, is in close proximity to the generated electrons in the dye and the TiO$_2$ nanoparticle film. This interface is the most important interface in the DSC and thus the majority of the current

research is focused at optimising the charge transfer/recombination rates at this point in the cell.

Electrons from the conduction band of the TiO_2 may recombine with the oxidised dye molecule before the dye is reduced by the electrolyte. However, reduction by the electrolyte is about 100 times faster than recombination [1.36] and thus no significant recombination between the electron in the TiO_2 and the oxidised dye is usually noted. The major recombination at the TiO_2/dye/electrolyte interface is between the electrons in the TiO_2 conduction band and the I_3^- ions of the electrolyte. The two main factors that contribute to this recombination reaction are the slow diffusion of electrons through the random polycrystalline network of TiO_2 nanoparticles [1.37] and the loss of electrons at the grain boundary of two nanoparticles [1.38]. The factors controlling the rate of charge carrier percolation across the nanocrystalline film are presently under intense scrutiny with various groups experimenting with a range of semiconducting architectures and materials. This will be discussed in more detail below.

1.6 Strategies to Improve the DSC Performance

As described above, recombination is primarily an interfacial process in DSCs, in contrast to the bulk process that occurs in conventional p-n junction solar cells. In principle, therefore, interfacial engineering rather than improved materials quality may be used to decrease the recombination rate in dye-sensitised nanoporous films [1.39]. In this regard, an attractive option is the

fabrication of TiO_2 structures with a higher degree of order than the random fractal-like assembly of nanoparticles, employed by conventional DSCs.

In 2001 Gong et al [1.40] reported the synthesis of ordered arrays of TiO_2 nanotubes by means of an electrochemical process involving oxidation and etching (better known as anodisation) of titanium foil sheets in the presence of a fluoride-containing electrolyte solution. Figure 1.8 shows scanning electron microscopy (SEM) micrographs of the resulting nanotubular architectures synthesised by Gong et al.
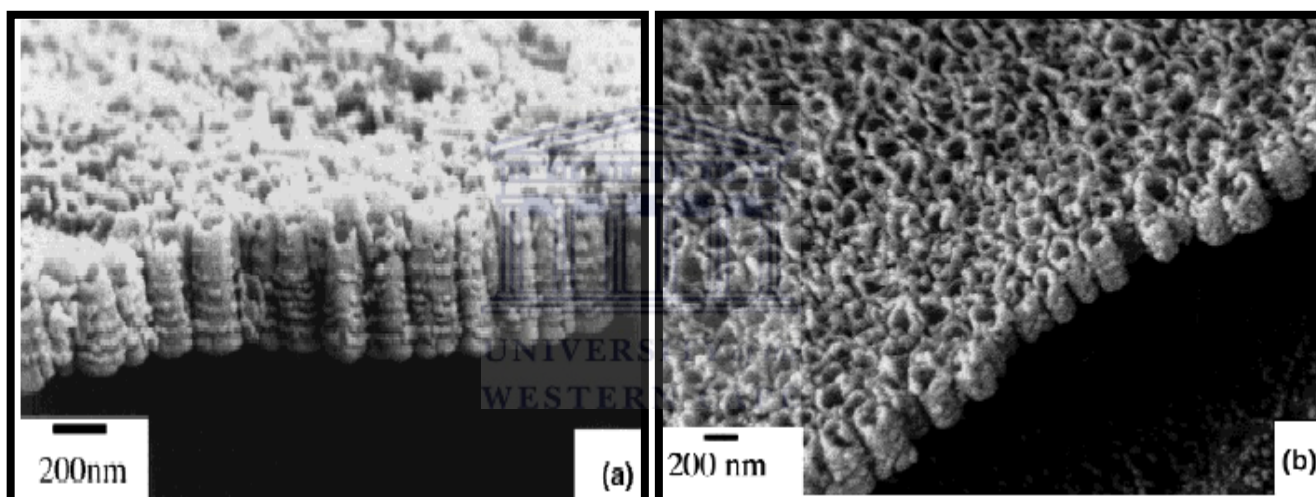
Figure 1.8: SEM micrographs of the TiO_2 nanotubes synthesised by Gong et al [1.40]

The finding above sparked vast interest among scientists in the DSC community, as this ordered form of TiO_2 could provide the solution to the excessive interfacial recombination reactions at the TiO_2/dye/electrolyte interface within the DSC. However, as a result of the short nanotube lengths achievable at the time as well as difficulties in synthesis on TCO/glass substrates, this novel TiO_2 architecture did not feature in a DSC until 2005

when the same group published their findings on the use of 6.2 μm long TiO_2 nanotubes in DSCs [1.41]. The performance of the resulting DSCs employing the arrays of nanotubes was quite satisfactory, with an overall efficiency of 4.7% achieved for front-side illuminated DSCs and 4.4% for back-side illuminated DSCs.

However, not much improvement in the cell efficiency of TiO_2 nanotube based DSCs have since been reported. This may be attributed to the variable morphologies often obtained during the anodisation process, the low surface area of the nanotubes compared to a film of nanoparticles and the presence of a remnant Ti layer at the bottom of the TiO_2 nanotubes, which prevents photon absorption from the working electrode side. Recently, the efficiency of front-side illuminated TiO_2 nanotube based DSCs was improved to 5.36% after $TiCl_4$ treatment of 20.0 μm thick TiO_2 nanotube arrays, which were detached from the Ti foil substrate [1.42]. Also, Roy et al [1.43] reported a solar cell efficiency of 5.2% for DSCs using a layer of TiO_2 nanotubes with well defined pore openings.

Although these arrays of TiO_2 nanotubes provide a vectorial and potentially rapid transport route (i.e. a high diffusion coefficient) for photo-generated electrons to the TCO substrate, the nanotubes remain in contact with the holes in the electrolyte and thus the probability of recombination of electrons in the TiO_2 nanotube conduction band with the I_3^- ions persists. In order to distance the TiO_2 from the electrolyte, some groups have shown that coating of nanoparticles with various metal-oxides with a higher conduction band edge than TiO_2, e.g. niobium pentoxide (Nb_2O_5) [1.43], strontium titanate

(SrTiO$_3$) [1.44], aluminium oxide (Al$_2$O$_3$) [1.45], etc., delays the recombination rates between the TiO$_2$ and holes. Figure 1.9 shows the energy diagram of a TiO$_2$ nanoparticle film coated with aluminium-oxide insulating layer, during which the Al$_2$O$_3$ coating delays reactions (3) and (5). DSC working electrodes of this nature are called core-shell electrodes, with the core consisting of the TiO$_2$ nanoparticle, whereas the Al$_2$O$_3$ layer acts as a shell. Core-shell electrodes consisting of Al$_2$O$_3$-coated TiO$_2$ nanoparticles have shown the most promise when incorporated in a DSC with enhancement in the cell efficiencies of up to 60% reported in comparison to DSCs with bare TiO$_2$ nanoparticle films [1.46].
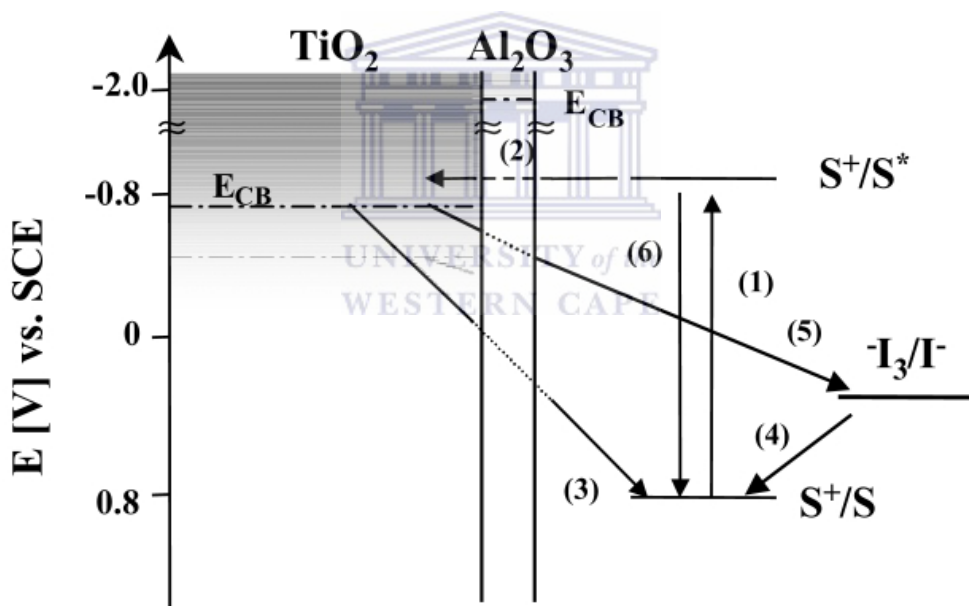
Figure 1.9: Illustration of the interfacial charge-transfer processes occurring at the nanostructured TiO$_2$/dye/electrolyte interface of DSSC and the employment of a Al$_2$O$_3$ insulating layer to retard the recombination reactions between the electrons in the TiO$_2$ conduction band and holes present in the dye and electrolyte [1.45]

Aims and Outline

The overall objective of this study is to develop a novel, previously unexplored Al_2O_3-coated TiO_2 nanotube architectures for application in a DSC. To achieve this goal, the innovation of the core-shell approach, as described above, will be applied to an array of anodised TiO_2 nanotubes. These novel architectures have the potential to (a) maintain vectorial electron transport through the TiO_2 film and (b) separate the electrons in the TiO_2 conduction band from the holes in the liquid electrolyte during operation of the DSC. The individual tasks/milestones of the study are as follow:

- *Optimisation of a two-electrode anodisation set-up:* A requirement of the traditional TiO_2 nanoparticle film is that it should be porous while maintaining a high surface area upon incorporation in a DSC; with film thicknesses of between 10 and 20 μm and porosity of 66% usually employed [1.21]. Therefore the bulk of the experimental work during this study will be focused on having accurate control of the physical dimensions of the nanotubes during anodisation and thus fabrication of TiO_2 nanotubes of length in excess of 15 μm, average nanotube diameter of 100 nm and wall thickness of 50 nm were aimed for. A major drawback of employing anodised TiO_2 nanotubes in the DSC is the presence of a remnant Ti metal layer at the bottom of the nanotubes, which prevents light absorption from the working electrode side and often results in low efficiency devices.

- *Synthesis of Al$_2$O$_3$-coated TiO$_2$ nanotubes:* During this stage of the study a simple sol-gel dip-coating process will be developed to coat the nanotubes with a thin layer of Al$_2$O$_3$ while maintaining the porosity of the nanotubes.

- *Manufacturing of front-side illuminated TiO$_2$ nanotube DSCs:* This part of the study will focus on manufacturing solar cells with TiO$_2$ nanotubes as the electron transport medium and comparing their performance with conventional cells employing films of TiO$_2$ nanoparticles.

- *Manufacturing of front-side illuminated Al$_2$O$_3$-coated TiO$_2$ nanotube DSCs:* The final stage of the study involves monitoring the photovoltaic performance of the Al$_2$O$_3$-coated TiO$_2$ nanotube solar cells with DSCs employing uncoated nanotubes, as well as uncoated TiO$_2$ nanoparticles.

The outline of this thesis is as follows:

Chapter One summarised South Africa's energy status and how photovoltaics, specifically DSCs, can help alleviate the strain on the country's coal reserves. The chapter highlighted the history of the DSC, the potential application of these novel solar cells in small scale electronics and BIPVs, the working principle of the cell, the concerns around the low performance of these cells and strategies that can be employed to improve the efficiency of the DSC.

Chapter Two will provide a description of the experimental techniques that were used in this study. More specifically the anodisation of Ti foil in fluoride-based electrolytes will be covered in detail. The chapter will also discuss the

sol-gel dip-coating technique used to synthesise Al_2O_3-coated TiO_2 nanotubes, the laboratory manufacturing of the various DSCs as well as the analytical techniques used to characterise the fabricated materials and solar cells.

Chapter Three will cover the results obtained from the anodisation process, in particular the morphology of the nanotubes, their crystallinity and optical properties.

Chapter Four will discuss the application of the TiO_2 nanotubes in the DSC, and the comparison of the photovoltaic performance of these cells to conventional DSCs with a film of nanoparticles as the charge transport medium.

Chapter Five gives details on the results obtained from the synthesis of core-shell Al_2O_3-coated TiO_2 nanotubes during dip-coating of the anodised TiO_2 nanotube arrays in an Al_2O_3 sol-gel solution. The Chapter will also cover the application of these structures in the DSC and their photovoltaic performance will be compared to that of DSCs with uncoated nanotubes and uncoated TiO_2 nanoparticles. A final chapter will summarise the major findings of the study and provide details on possible future studies.

References

[1.1]   Department of Minerals and Energy, Republic of South Africa. 2010. *Digest of South African Energy Statistics 2006*, ISBN: 0-9584376-4-5. [Online]. Available: www.dme.gov.za/energy/statistics.stm [Accessed: 06 May 2010]

[1.2]   Department of Minerals and Energy, Republic of South Africa. 2010. *White Paper on Renewable Energy November 2003*. [Online]. Available: www.dme.gov.za/energy/renewable.stm [Accessed: 06 May 2010]

[1.3]   South African Government Information, Republic of South Africa. 2010. *South African Yearbook 2007/8.* [Online]. Available: www.info.gov.za/aboutsa/landpeople.htm#intro [Accessed: 06 May 2010]

[1.4]   G. Stassen, *Towards a Renewable Energy Strategy for South Africa*, Ph.D. Thesis, University of Pretoria, South Africa, 1996

[1.5]   T. Markvart, L. Castafier, *Practical Handbook of Photovoltaics: Fundamentals and Applications*, Elsevier Ltd., Oxford, U. K., 2003

[1.6]   R. A. Messenger, J. Ventre, *Photovoltaic Systems Engineering*, 2nd Ed., CRC Press, Florida, USA, 2004

[1.7]   P. Gevorkian, *Sustainable Energy Systems in Architectural Design: A Blueprint for Green Building*, McGraw-Hill, New-York, USA, 2006

[1.8]   B. O'Regan, M. Grätzel, Nature 353 (1991) 737

[1.9]   A. J. Frank, N. Kopidakis, J. Van De Lagemaat, Coord. Chem. Rev. 248 (2004) 1165

[1.10] M. Grätzel, A. J. Frank, J. Phys. Chem. 86 (1982) 2964

[1.11] A. Hagfeldt, M. Grätzel, Chem. Rev. 95 (1995) 49

[1.12] SolarPrint Ltd, Dublin Ireland. 2010. *SolarPrint.* [Online]. Available: www.solarprint.ie [Accessed 06 May 2010]

[1.13] G24 Innovations Ltd Cardiff Wales. 2010. g24i [Online], Available www.g24i.com [Accessed on 20 August 2010]

[1.14] Solaronix, Aubonne Switzerland. 2010. Solaronix [Online], Available www.solaronix.com [Accessed on 20 August 2010]

[1.15] Dyesol Ltd, Queanbeyan New South Wales Australia. 2010 Dyesol [Online], Available www.dyesol.com [Accessed 10 August 2010]

[1.16] Timo Technology Co. Ltd, Seoul South Korea. 2010. Timo [Online], Available www.timo.co.kr [Accessed 21 July 2010]

[1.17] M. Grätzel, Accounts of Chemical Research 42 (2009) 1788

[1.18] Solarbuzz: Solar Energy Research and Consultancy. 2010. Solarbuzz [Online], Available www.solarbuzz.com [Accessed 20 August 2010]

[1.19] Samsung SDI, Seoul, South Korea. 2010 SamsungSDI [Online], Available www.samsungsdi.com [Accessed 06 October 2010]

[1.20] 3GSolar, Jerusalem, Israel. 2010 3gsolar [Online], Available www.3gsolar.com [Accessed 06 October 2010]

[1.21] M. Grätzel, C. R. Chimie 9 (2006) 578

[1.22] R. Sastrawan, *Photovoltaic Modules of Dye Solar Cells*, Ph.D Thesis, Albert-Ludwigs-Universität, Freiburg, Germany, 2006

[1.23] J. Xia and S. Yanagida, Sol. Energy (2009), doi:10.1016/ j.solener.2009.10.005

[1.24] H. Park, W.-R. Kim, H.-T. Jeong, J.-J. Lee, H-G. Kim, and W.-Y. Choi, Sol. Energy Mater. Sol. Cells (2010), doi:10.1016/j.solmat.2010.02.017

[1.25] M.K. Nazeeruddin, I. Kay, A. Rodicio, R. Humphry-Baker, E. Müller, P. Liska, N. Vlachopouloss, M. Grätzel, J. Am. Chem. Soc. 115 (1993) 6382

[1.26] M. Grätzel, J. Photochem. Photobio. C: Photochem. Rev. 4 (2003) 145

[1.27] A. Tolvanen, *Characterisation and Manufacturing Techniques of Dye-sensitised Solar Cells*, M.Sc Thesis, Helsinki University of Technology, Helsinki, Finland. 2003

[1.28] G. Benkö, J. Kallioinen, E. Jouko. I. Korppi-Tommola, A.P. Yartsev and V. Sundström, J. Am. Chem. Soc. 124 (2002) 489

[1.29] M.K. Nazeeruddin, P. Pechy, T. Renouard, S.M. Zakeeruddin, R. Humphry-Baker, P. Comte, *et al.*, J. Am. Chem. Soc. 123 (2001) 1613

[1.30] P.J. Cameron and L.M. Peter, J. Phys. Chem. B 107 (2003) 14394

[1.31] J. Kruger, R. Plass, L. Cevey, M. Piccirelli, M. Grätzel and U. Bach, Appl. Phys. Lett. 79 (2001) 2085

[1.32] T.N. Murakami and M. Grätzel, Inorg. Chim. Acta 361 (2008) 572

[1.33] N. Papageorgiou, W.F. Maier and M. Grätzel, J. Electrochem. Soc. 144 (1997) 876

[1.34] A. Kay and M. Grätzel, Sol. Energy Mater. Sol. Cell 44 (1996) 99

[1.35] T. Ma, X. Fang, M. Akiyama, K. Inoue, H. Noma and E. Abe, J. Electroanal. Chem. 574 (2004) 77

[1.36] A. Hagfeldt and M. Grätzel, Chem. Rev 95 (1995) 49

[1.37] L. Peter, J. Electroanal. Chem. 599 (2007) 233

[1.38] N. W. Duffy, L. M. Peter and K. G. U. Wijayantha, Electrochem. Commun. 2 (2000) 262

[1.39] B.A. Gregg, F. Pichot, S. Ferrere and C.L. Fields, J. Phys. Chem. B 105 (2001) 1422

[1.40] D. Gong, C.A. Grimes, and O.K. Varghese, J. Mater. Res. 16 (2001) 3331

[1.41] M. Paulose, K. Shankar, O.K. Varghese, G.K Mor and C.A. Grimes, J. Phys. D: Appl. Phys. 39 (2006) 2498

[1.42] H. Park, W.-R. Kim, H.-T. Jeong, J.-J. Lee, H.-G. Kim and W.-Y. Choi, Sol. Energy Mater. Sol Cells, doi:10.1016/j.solmat.2010.02.017

[1.43] P. Roy, S.P. Albu and P. Schmuki, Electrochem. Commun. (2010), doi: 10.1016/j.elecom.2010.04.029

[1.44] S.M. Yang, Y.Y. Huang, C.H. Huang and X.S. Zhao, Chem. Mater. 14 (2002) 1500

[1.45] E. Palomares, J.N. Clifford, S.A. Haque, T. Lutz and J.R. Durrant, Chem. Commun J. Am. Chem. Soc. 125 (2003)

[1.46] J.Y. Kim, S. Lee, J.H. Noh, H.S. Jung and K.S. Hong, J. Electroceram. 23 (2009) 422

CHAPTER TWO
Experimental Techniques

In this chapter an overview will be given of the experimental route taken to synthesise Al_2O_3-coated TiO_2 nanotubes and the construction of dye-solar cells (DSCs) incorporating both bare TiO_2 nanotubes and Al_2O_3-coated nanotubes. Section 2.1 will give a broad background of the anodisation technique, its evolution towards the fabrication of TiO_2 nanotubes and the growth model of these nanotube structures under specified experimental conditions. Section 2.2 will cover the sol-gel synthesis technique developed for the synthesis of Al_2O_3-containing sol-gel, which was then used to coat the nanotubes. This is followed by a discussion of the steps taken to manufacture lab-scale DSCs in Section 2.3.
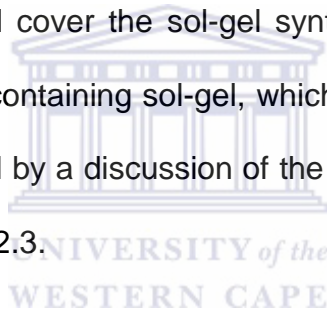
2.1 Electrochemical Anodisation

2.1.1 Background

Since its introduction in 1923 [2.1], the anodisation process has mainly been employed for the synthesis of porous films of aluminium oxides in highly concentrated sulphuric acid electrolytes; and compact oxide layers in the presence of neutral electrolytes [2.2 – 2.4]. During the late nineties anodisation of different valve metals, most notably zirconium (Zr) [2.5], niobium (Nb) [2.6], tungsten (W) [2.7] and titanium (Ti) [2.8, 2.9] in hydrofluoric and phosphoric electrolytes was attempted with the specific goal of

synthesising self-organised, porous metal-oxide structures. Of particular interest was the work published by Gong et al. in 2001 [2.8] on the formation of arrays of TiO_2 nanotubes during anodisation of Ti foil in a fluoride-based electrolyte solution. TiO_2 is a material with a host of almost unique properties, used for many years in various applications such as photo-catalysts [2.10], sensors for gas detection [2.11] and solar cells [2.12]; thus the work of [2.8] can be considered groundbreaking in the materials science of this important material.

A typical two-electrode anodisation setup is shown in Figure 2.1. The set up comprises of an anode, which is the metal (M) under consideration (e.g. Al, Ti, Zr, etc.), whereas the cathode is typically a platinum (Pt) or nickel (Ni) plate or mesh grid. The two electrodes are connected to a voltage source and immersed in a liquid electrolyte. Depending on the anodisation conditions applied (e.g. applied voltage, electrolyte and temperature), a compact, porous, or tubular oxide layer can be synthesised [2.13]. The formation of the thick metal oxide (MO) layer on the metal surface at the anode involves a two step process as given by the following reactions,

$$M^0 \rightarrow M^{2+} + 2e^- \qquad (2.1)$$

$$M^{2+} + H_2O/OH^- \rightarrow M(OH)_2 \rightarrow MO \qquad (2.2)$$
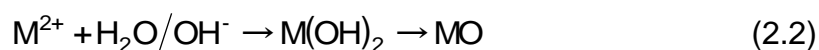
Typically growth occurs proportional to the applied potential with a growth factor, $f_g \sim 1 - 5$ nm/V [2.14] up to a voltage where dielectric breakdown of the oxide occurs [2.15, 2.16]. The structure of the as grown oxide can be amorphous or crystalline dependent on the electrochemical parameters such

as the applied potential, the time of anodisation, or the sweep rate of the potential ramp [2.13].
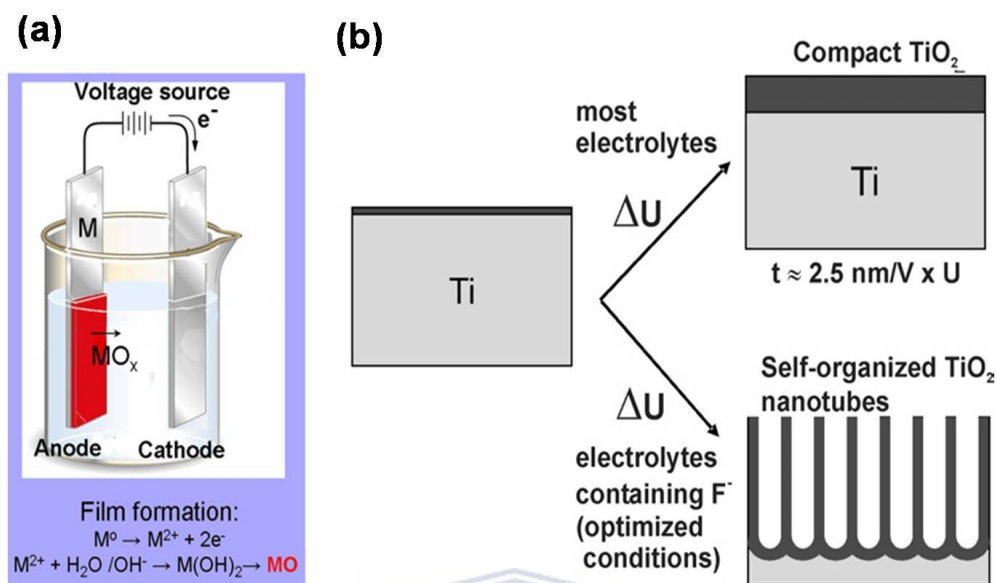
Figure 2.1: (a) Schematic of a simple set-up for anodisation experiments and (b) formation of self-organised TiO_2 nanotubes during anodisation [2.13]
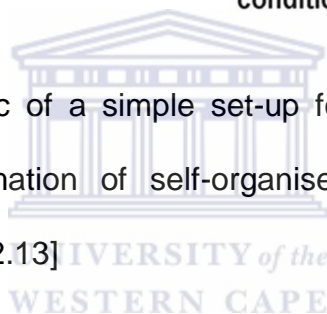
2.1.2 Growth Model of TiO_2 Nanotubes during Anodisation

The anodic growth of compact titanium oxides on Ti surfaces and the formation of tubes in the presence of fluoride ion containing electrolytes are, in the simplest approach, governed by a competition between anodic oxide formation according to reaction (2.3)

$$Ti + 2H_2O \rightarrow TiO_2 + 4H^+ + 4e^- \qquad (2.3)$$
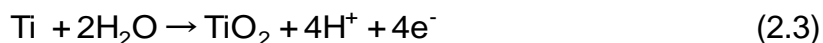
and the chemical dissolution of the oxide as soluble fluoride complexes according to the reaction

$$TiO_2 + 6F^- \rightarrow [TiF_6]^{2-} \qquad (2.4).$$

Reaction (2.3) is depicted schematically in Figure 2.2 (a) in the presence of fluoride-free electrolytes. Oxidised Ti species react with O^{2-} ions (from H_2O) to form an oxide layer. Further oxide growth is controlled by field-aided ion transport (O^{2-} and Ti^{4+} ions) through the growing oxide. As the system is under a constant applied voltage, the field within the oxide is progressively reduced by the increasing oxide thickness and thus the process is self-limiting. If the Ti^{4+} ions arriving at the oxide/electrolyte interface are not made soluble by complexation (reaction (2.4) above), a hydroxide layer will precipitate in most electrolytes [2.17].
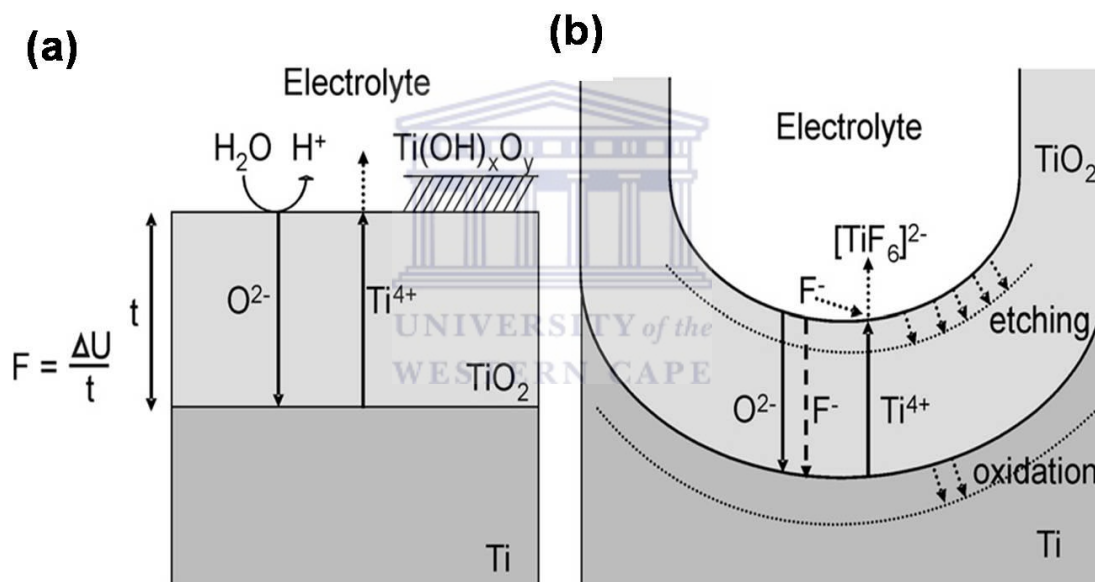
Figure 2.2: Ti anodisation in (a) absence of fluorides and (b) in presence of fluorides [2.13]

In the presence of F^- ions the situation becomes more complex as shown schematically in Figure 2.2 (b). This is mainly attributable to two effects of the F^- ion: (i) its ability to form water-soluble $[TiF_6]^{2-}$ complexes according to reaction (2.4) and (ii) its small ionic radius that allows the F^- ion to enter the growing TiO_2 lattice and be transported through the oxide by the applied field; thus competing with O^{2-} transport in the opposite direction as shown in Figure

2.2 (b). The complex formation ability leads to a permanent chemical etching (or dissolution) of the formed TiO_2 layer and prevents $Ti(OH)_xO_y$ precipitation as the Ti^{4+} ions arriving at the oxide/solution interface reacts with the incoming F^- ions to form $[TiF_6]^{2-}$ complexes.

Figure 2.3 shows a typical current-time graph of Ti anodisation in the absence (black graph) and in the presence (red graph) of fluoride ions. Three stages of the growth process can readily be identified in the red graph. During stage I an exponential IR drop is observed caused by the formation the thick insulating TiO_2 layer according to reaction (2.2). During stage II an increase in the current is observed where after a quasi-steady state is reached during stage III, which is markedly different from the anodisation process in fluoride free electrolytes (black curve).
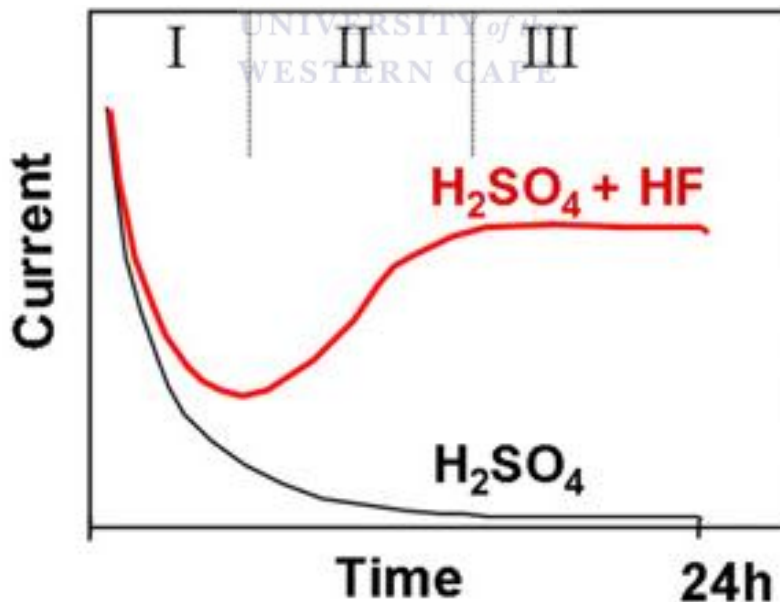
Figure 2.3: Characteristic current transients for Ti anodisation with and without fluorides in the electrolyte [2.13]

31

The current behaviour of the red curve in Figure 2.3 can be ascribed to different stages of the pore formation as illustrated in Figure 2.4. During stage I a compact oxide layer is formed on top of the Ti metal. Hereafter, during stage II the surface is locally activated and pores start to grow randomly. As a result of this pore formation the active area of the oxide layer increases and thus the current increases, as shown by the red curve of Figure 2.3. With time, the individual pores start interfering with each other and start competing for the available current, which leads to tree-like growth of the oxide layer and formation of the nanotube structure during stage III, as can be observed in Figure 2.4. These different stages of growth have been observed experimentally during scanning electron microscopy analyses of Ti foil after the individual stages of growth [2.17].
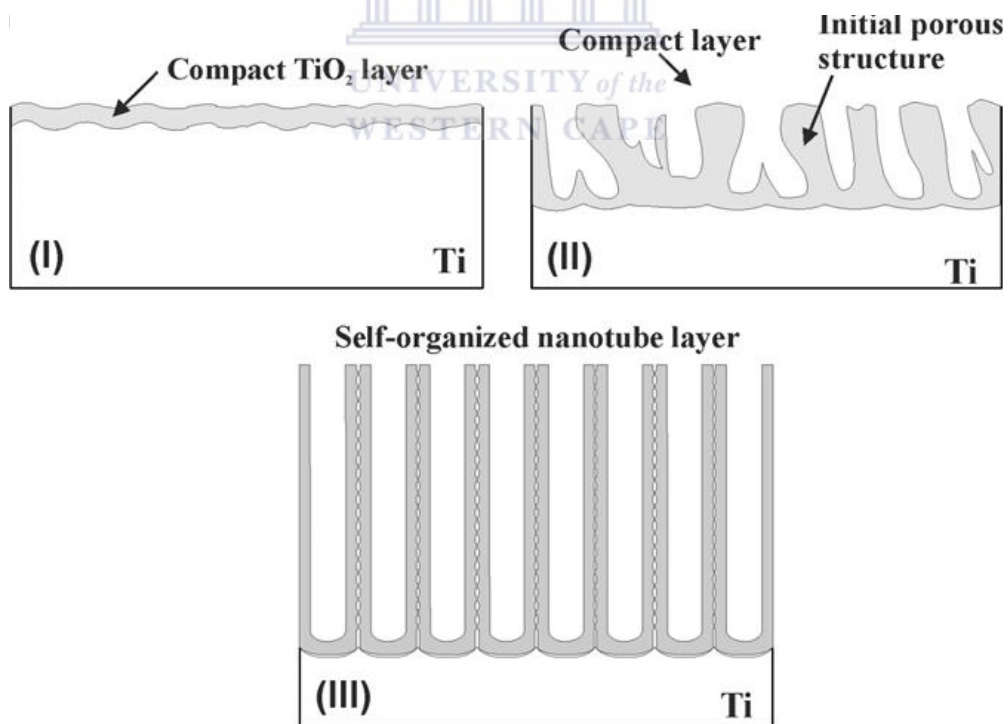
Figure 2.4   Evolution of the TiO_2 morphology during different stages of growth during anodisation [2.13]

2.1.3 Experimental Procedure

Figure 2.5 shows the anodisation set-up employed during this study and is based on a standard two-electrode set-up as previously reported [2.18].
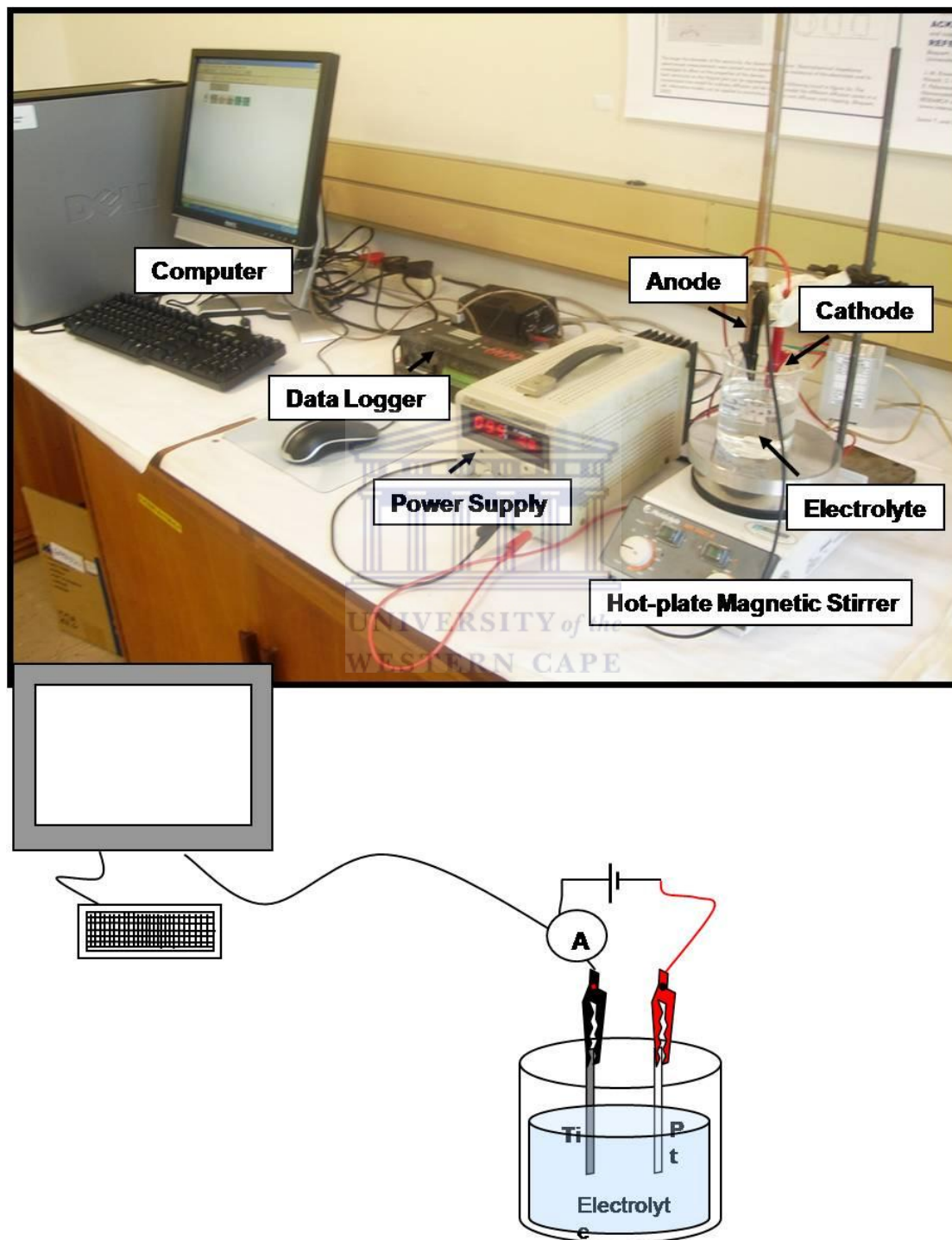
Figure 2.5: Anodisation set-up employed to synthesise TiO_2 nanotube arrays

A Xytron GPS-3030E direct current (DC) power supply (900 W maximum power output) is used to supply a DC voltage across the electrodes. For high voltages (i.e. greater than 30 V), a second power supply (Texio PS36-30, 1000 W maximum power output) is connected in series to the Xytron power supply. A dataTaker® DT600 datalogger, interfaced with a computer, is used to record the changes in the current density at the anode. A magnetic hot-plate stirrer is employed to assist in the preparation of the electrolyte solution before-hand.

For their use as anodes, Ti foil sheets of 25 µm thickness were cut into 1 x 1.5 cm^2 rectangles, rinsed with anhydrous ethanol, dried in a stream of nitrogen gas and finally cured at 80 ºC for 10 minutes. Once dry, a single Ti substrate was clipped onto a pair of crocodile clips and immersed in the electrolyte solution along with a 1 x 1.5 cm^2 flag-shaped Pt grid; the Pt grid acted as the cathode during anodisation and the distance maintained between the two electrodes was approximately 1 cm. Hereafter the voltage was ramped to the desired value at a rate of approximately 1 V/s. Two different types of electrolyte solutions were used during this study. In the first instance an aqueous, low pH solution was used. The solution was prepared by dissolving 0.15 M ammonium fluoride (NH_4F) in phosphoric acid (H_3PO_4). The H_3PO_4 concentration was kept constant and only the NH_4F content varied. This mixture was then added to deionised water. The total volume of the solution was 200 ml and stirred rigorously using the magnetic stirrer hot-plate. The second electrolyte was a 200 ml solution consisting of NH_4F dissolved in deionised H_2O and added to ethylene glycol (EG); the pH of this solution was neutral at approximately 7.5. During this set of experiments, the H_2O concentration was kept constant and the NH_4F concentration varied. All chemicals used during this

study were of chemical grade and obtained from Merck (Pty) Ltd., South Africa.

Table 2.1 summarises the different experimental parameters studied. The as-

synthesised nanotubes were amorphous and thus were annealed in a belt-

furnace at 450 °C for 2 hours in air at atmospheric pressure.

Table 2.1: Anodisation parameters studied

Parameter / Electrolyte	$NH_4F + H_3PO_4 + H_2O$	$NH_4F + H_2O + EG$
Voltage (V)	5 – 30	5 – 60
NH_4F concentration (M)	0.15 – 1	0.15 – 1
Time	8 seconds – 24 hours	8 seconds – 24 hours

2.2 Sol-Gel Synthesis

2.2.1 Background

As will be shown in this work, one of the most technologically important

aspects of sol-gel processing is its suitability for preparing thin films by common

processes such as dipping, spinning or spraying (see part (a) of Figure 2.7).

Compared to conventional thin film synthesis techniques such as chemical

vapour deposition, thermal evaporation and sputtering, sol-gel film formation

requires considerably less equipment and as such is more cost effective. In

addition, sol-gel deposition allows for accurate control of the microstructure of

the deposited film, which is absent in most cases during deposition via the other

methods mentioned above [2.19].

A suspension in which the dispersed phase is so small (1 ~ 1000 nm) that

gravitational forces are negligible and interactions are dominated by short range

forces such as Van Der Waals forces and surface charges, is called a colloid. Based on this definition, a "sol" is considered a colloidal suspension of solid particles in a liquid [2.19]. Defining the term "gel" is bit more complicated and often disagreed upon. Henisch [2.20] defined a gel by describing it as a component system of a semi-solid nature, rich in liquid. However the term "semi-solid" in the definition is very ambiguous and spurred various debates on what qualifies as a gel and what not. The most comprehensive definition of a gel can be found in [2.19] and is interpreted as consisting of continuous solid (sols) and fluid phases of colloid dimensions. In the above definition, continuity implies that one could travel through the solid phase from one side of the sample to the other without having to enter the liquid; conversely one could make the same trip entirely within the liquid phase. Figure 2.6 schematically depicts the above – a line segment (P) originating in a pore and running perpendicularly into the nearest solid phase must re-emerge in another pore less than 1 µm away since both phases are of colloidal dimensions. Similarly, an arrow S passes from solid to solid in Figure 2.6. Gel formation (known as gelation) usually commences with the formation of fractal aggregates that grow until they begin to impose on one another, where after these clusters link according to the theory of percolation [2.19]. Hence, the term sol-gel refers to a suspension of gels consisting of colloidal solid and fluid phases.
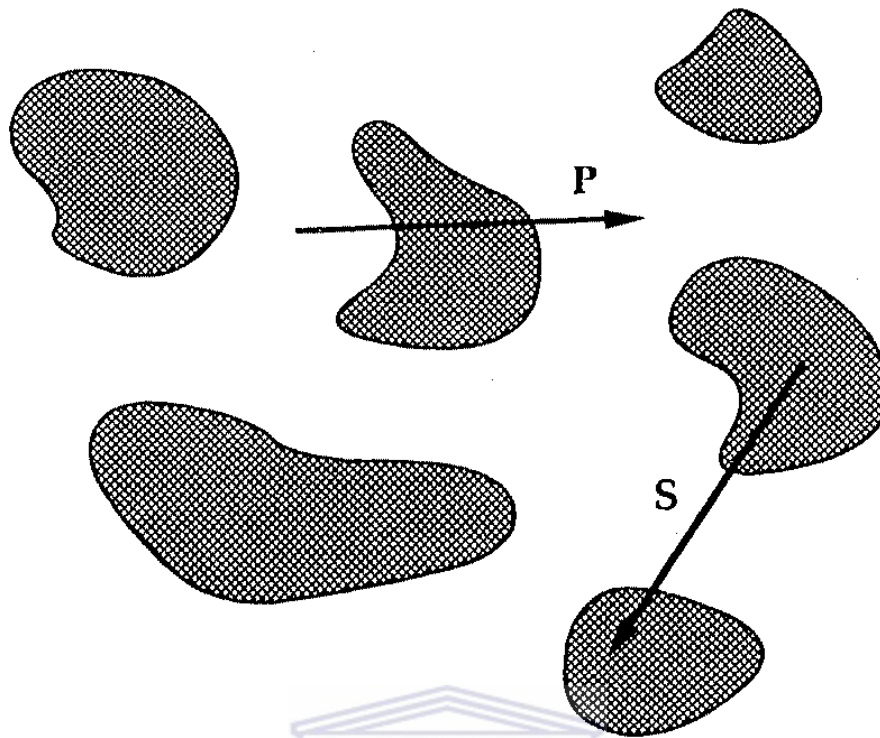
Figure 2.6: Schematic illustration of gel formation [2.19]

In 1930 a group from the Schott Company [2.21, 2.22] developed the first

sol-gel process for the deposition of oxide layers on industrial glass using

combinations of metal-containing precursors. Approximately thirty years later

Shroeder [2.23] expanded the technique for the deposition of transparent

coatings on glass surfaces in order to correct their refractive indices. The most

significant work in this field, however, was realised a few years later when the

Dislich group [2.24] reported on the synthesis of boron-silicate glass by heating

baths of oxide powders obtained from a low-temperature sol-gel process. This

work led to the first "International Conference on Glasses and Glass Ceramics

obtained by Gel methods" in 1981 [2.25], which marked the advent of modern

sol-gel science.

Of particular interest to this study is the coating of nanostructured materials, most notably nanoparticles with a thin layer of metal-oxide by means of sol-gel dip-coating; the so-called core-shell nanostructured materials [2.26]. Figure 2.7 shows the different steps involved in a simple sol-gel experiment and the different products obtainable after each step. As shown in Figure 2.7, the sol-gel technique produces two types of end products, namely (a) dense films or (b) dense ceramics. For the purpose of this study only a discussion on the synthesis of dense films via dip-coating (i.e. type (a) in Figure 2.7) will be discussed. The process can be categorised in three steps namely: (i) preparation of the precursor solution; (ii) deposition of the prepared sol on the substrate by dip-coating and (iii) heat treatment of the xerogel film. The term xerogel is given to the dried gel at ambient pressure, whereas the dried gel in supercritical conditions is referred to as an aerogel.
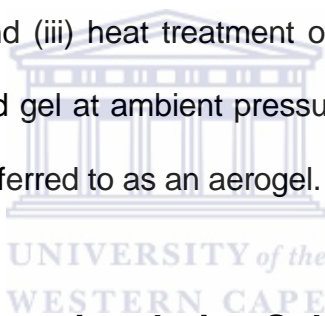
2.2.2 Alumina Film Formation during Sol-Gel Dip-coating

Aluminium is the second most abundant metal in the earth's crust and exhibits only the trivalent state, Al(III) in compounds and in solution [2.27]. Of interest to this study is the evolution of hydrolysis chemistry towards the understanding of the hydrothermal digestion of Al(III) as the anionic species, $[Al(OH)_4]^-$ at high pH. This is important since aluminium hydroxides and oxo-hydroxides are commonly used precursors for alumina gels, used during dip-coating for the deposition of Al_2O_3 thin films [2.19].
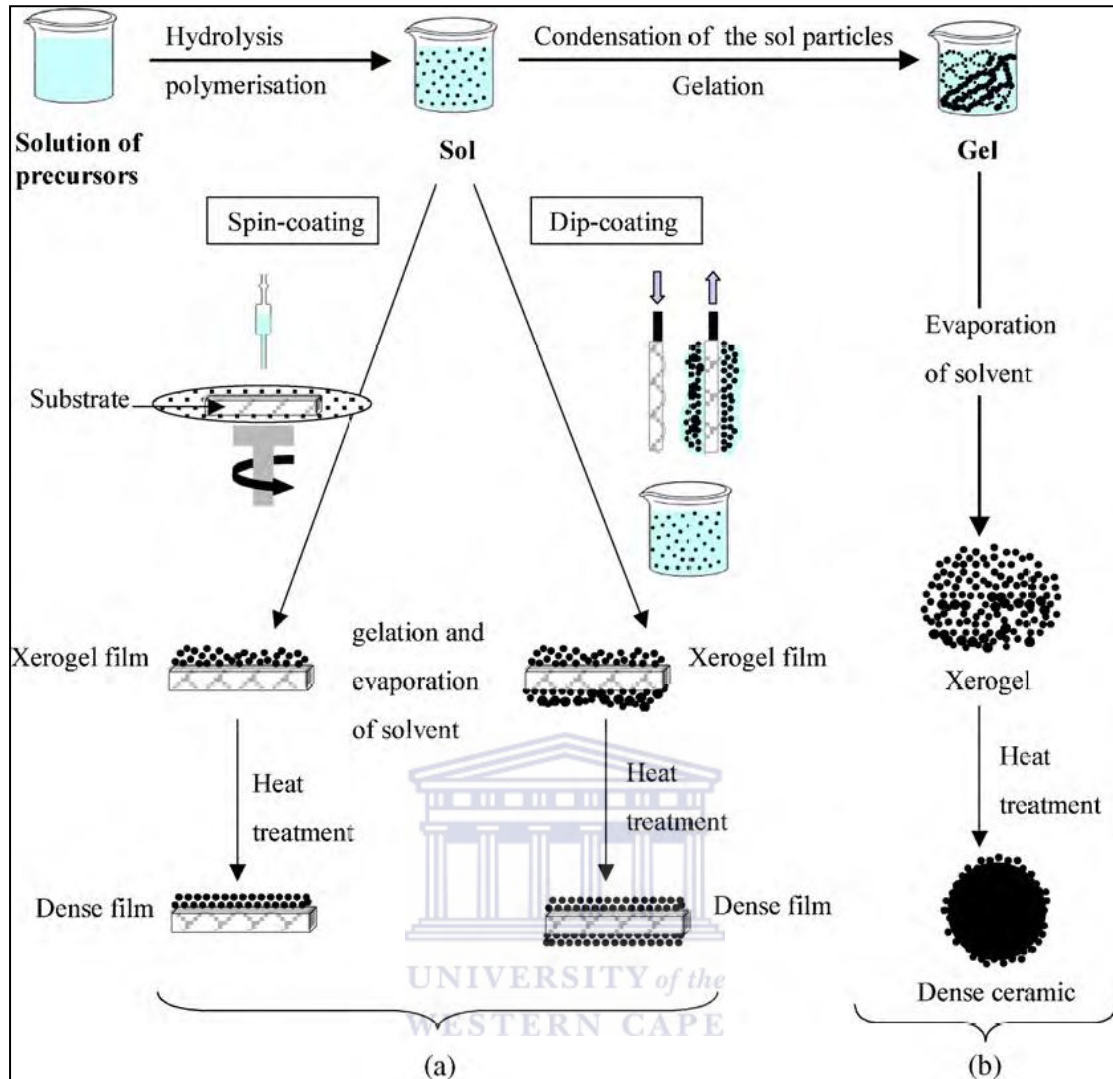
Figure 2.7: Typical sol-gel experimental set-up for the synthesis of either dense films or ceramics [2.26]

Al^{3+} has an ionic radius of 0.5 Å, a coordination number N = 6 and exists as the unhydrolised species $[Al(OH_2)_6]^{3+}$ below pH 3. With increasing pH, $[Al(OH_2)_6]^{3+}$ can be hydrolysed according to:

$$[Al(OH_2)_6]^{3+} + hH_2O \rightarrow [Al(OH)_h(OH_2)_{6-h}]^{(3-h)+} + hH^3O^+ \qquad (2.5)$$

$$hH_3O^+ + hOH^- \rightarrow 2hH_2O \qquad (2.6)$$
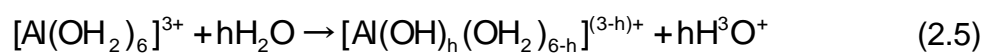
where h is the molar ratio of hydrolysis, equivalent to the ratio of OH to Al according to the net reaction, i.e. equation (2.5) + equation (2.6) [2.19]. Subsequent condensation yields metastable polynuclear hydroxides or oxo-hydroxides in the form of bayerite (α-Al(OH)$_3$) precipitates, as shown in Figure 2.8 [2.28]. These metastable precipitates can form and redissolve slowly and the species distribution is very sensitive to the precise conditions during hydrolysis, such as the time-temperature history and the method of base addition [2.27].
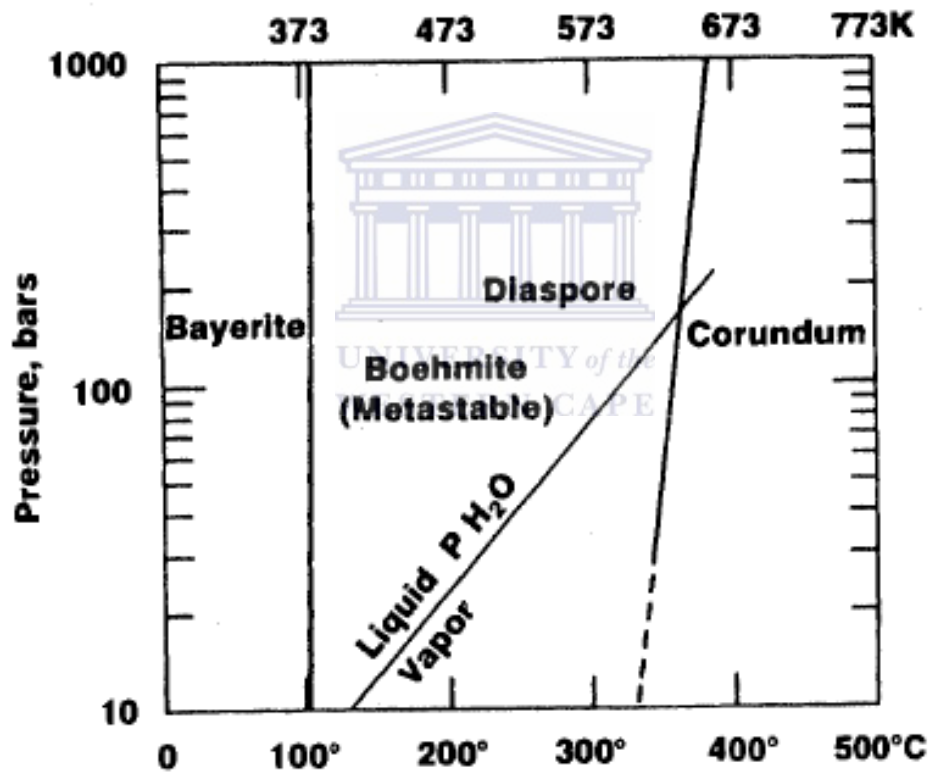
Figure 2.8: Pressure-temperature phase diagram of the Al$_2$O$_3$-H$_2$O binary system [2.28]

Above h = 2.46 in (2.5) rapid precipitation of highly condensed, amorphous or weakly crystalline phases occurs. The most common crystalline

40

phase is pseudoboehmite (or gelatinous boehmite) as shown by the x-ray diffraction (XRD) patterns of Figure 2.9 [2.28].
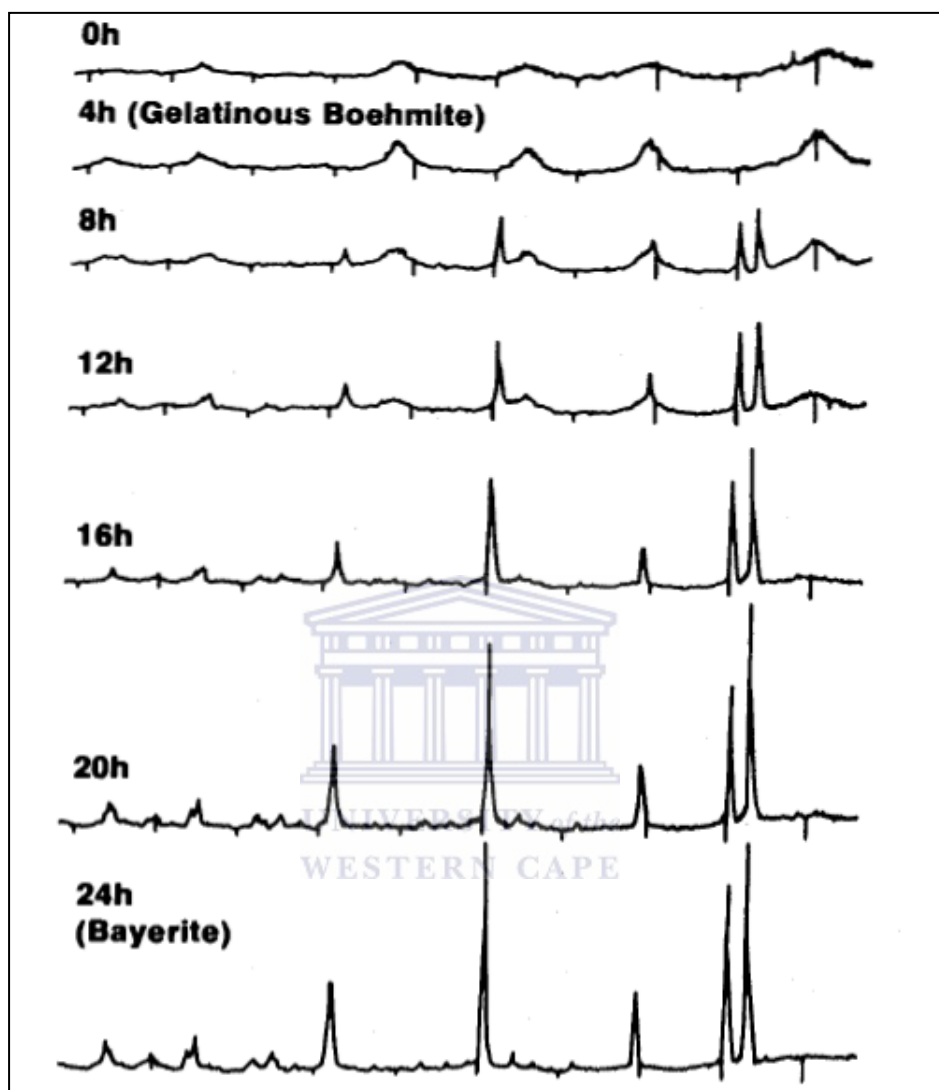
Figure 2.9:   XRD patterns of an aluminium hydroxide gel as a function of aging time at pH 9 and 300K [2.28]

The XRD pattern of pseudo-boehmite shows broad diffraction peaks that coincide with the major reflections of highly crystalline boehmite, γ-AlO(OH), but are shifted as result of water intercalation or association. The degree of crystallinity, crystallite size and chemical composition of gelatinous aluminas

depend critically on the temperature, rate of precipitation, final pH, concentration of precursor solutions and time of ageing [2.19]. As shown in Figure 2.9 both amorphous and pseudo-crystalline phases transform into bayerite with time. During this study, however, the alumina gels are transformed into corundum alumina (α-Al_2O_3) by means of sintering of the sol-gel coated film at 450 $^{\circ}$C for 30 minutes at atmospheric pressure, as will be explained in detail below.

2.2.3 Experimental Procedure

This study employed a slightly modified version of the commonly used Yoldas process [2.29] for the synthesis of α-Al_2O_3 layers on the anodised TiO_2 nanotubes and nanoparticle films, shown schematically in Figure 2.10. The process involves hydrolysing an aluminium alkoxide, namely aluminium butoxide ($Al(Bu^sO)_3$) in water at a temperature between 80 and 100 $^{\circ}$C, resulting in the precipitation of fibrillar boehmite. The next step in the synthesis process is peptisation with a mineral acid such as HNO_3 or HCl to form a stable particulate sol. This is followed by evaporation of the solvent and extraction of the butanol phases in a repetitive fashion until all unwanted phases are removed. Gelation is then achieved by heating of the sol, followed finally by calcination to form the stable corundum Al_2O_3 phase.

The Yoldas process was slightly adapted in that isopropanol was used as the solvent during the hydrolysis phase of Figure 2.10, which allowed for a lower hydrolysis temperature of 60 $^{\circ}$C in accordance with the work done by Palomares et al. [2.30]. Analytical grade aluminium tri sec-butoxide, $Al(BuO)_3$

was dissolved in 50 ml isopropanol under slow magnetic agitation in a dry nitogren ambient at 60 ºC. No ether extraction was performed on the prepared alumina sol since the solution was used as a dipping solution. Experiments were conducted as a function of Al(BuO)$_3$ concentration, dipping time and temperature and repeated dipping/sintering cycles. However, the overlayer growth was found to be independent of the dipping time or temperature, but dependent on precursor concentration and the number of dipping/sintering cycles; one dipping/sintering cycle comprised of dipping the TiO$_2$ film in the alumina sol for 30 seconds followed by sintering at 430 ºC for 30 minutes in air at atmospheric pressure.
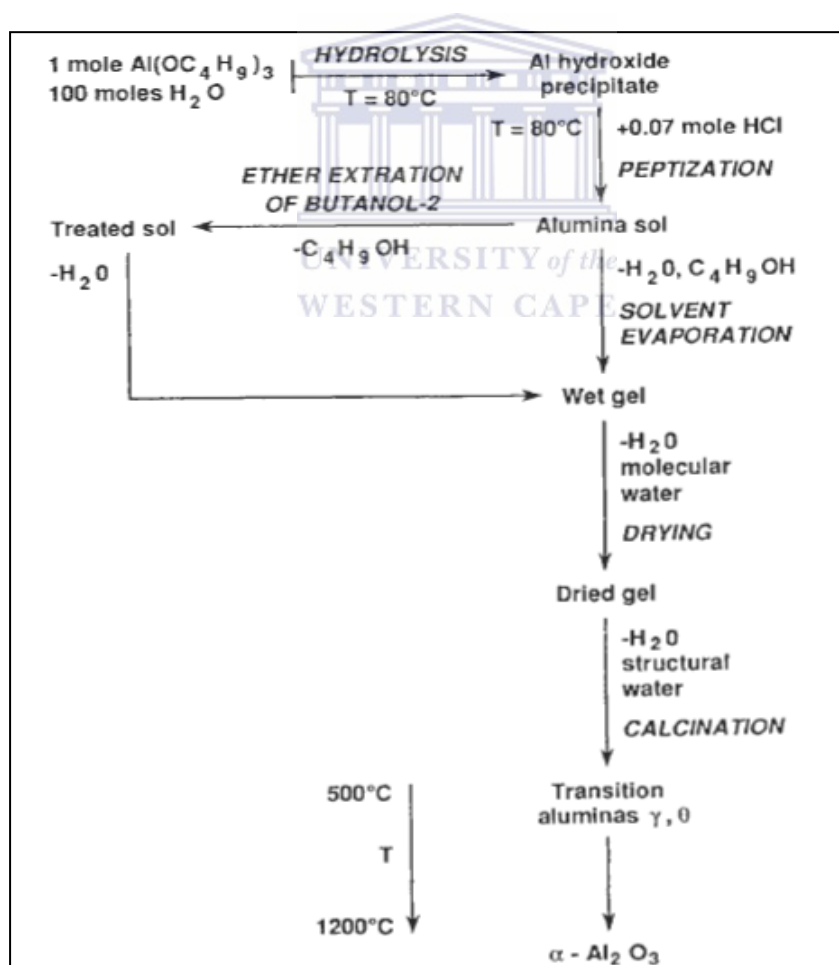
Figure 2.10: Flow chart of the Yoldas process used during this study for the synthesis of alumina [2.29]

Figure 2.11 shows images of the TiO_2 nanoparticle film coated under different experimental conditions. The film was dip-coated in the alumina sol for 0.05, 0.1, 0.5 and 1 M $Al(BuO)_3$ as shown by samples (1) to (4) in Figure 2.11. Samples (5) to (8) were treated for 1, 2, 3 and 4 dipping/sintering cycles, respectively. As can be seen, an $Al(BuO)_3$ precursor concentration of 1M yields the most uniform film, whereas a single dipping/sintering cycle results in a TiO_2 film exhibiting no cracks in its morphology.
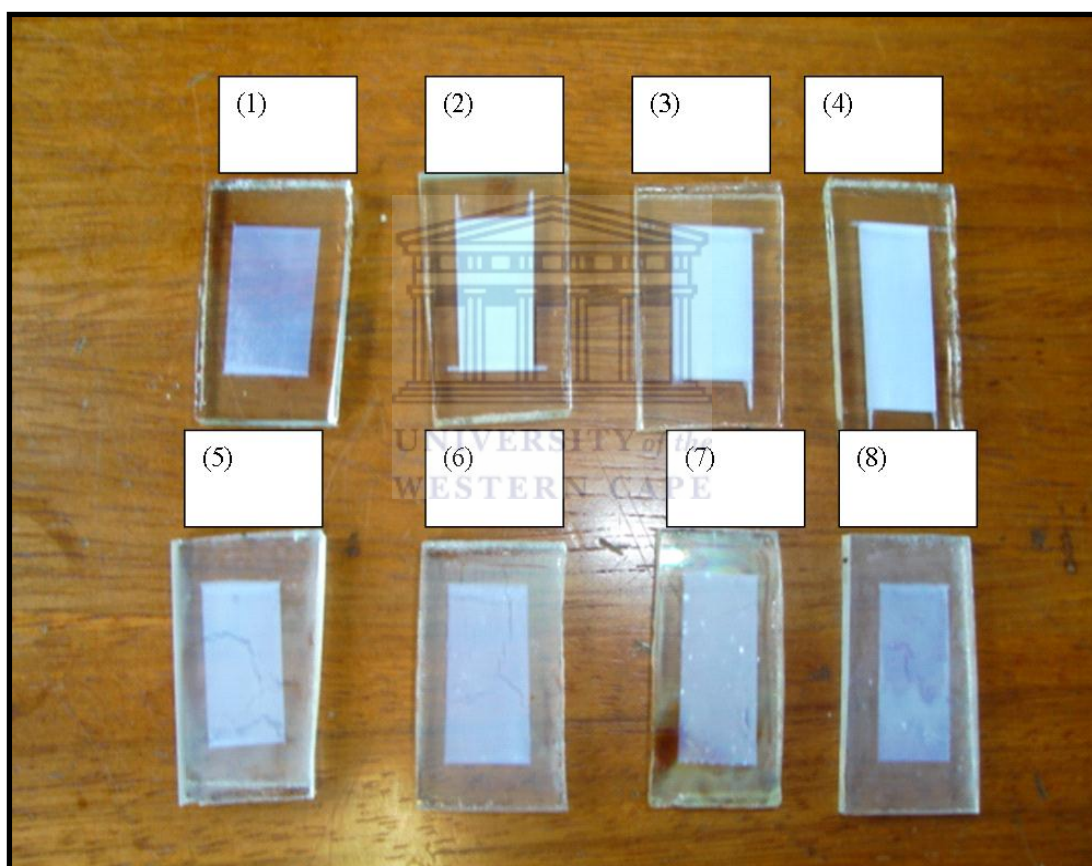
Figure 2.11: Images of the TiO_2 nanoparticle film coated with Al_2O_3 using an alumina sol consisting of (1) 0.05, (2) 0.1, (3) 0.5 and 1M $Al(BuO)_3$ as the precursor; and subjecting the TiO_2 film to (4) 1, (5) 2, (6) 3, (7) 4 and (8) 5 dipping/sintering cycles

2.3 Dye-Sensitised Solar Cell Manufacturing

DSCs employing both TiO_2 nanoparticle and nanotube films as the electron transport medium were fabricated and investigated in this study. The Al_2O_3 layers were coated onto both the TiO_2 nanoparticle and nanotube films. Figure 2.12 shows a schematic representation of a TiO_2 nanoparticle based DSC that was manufactured in this study.
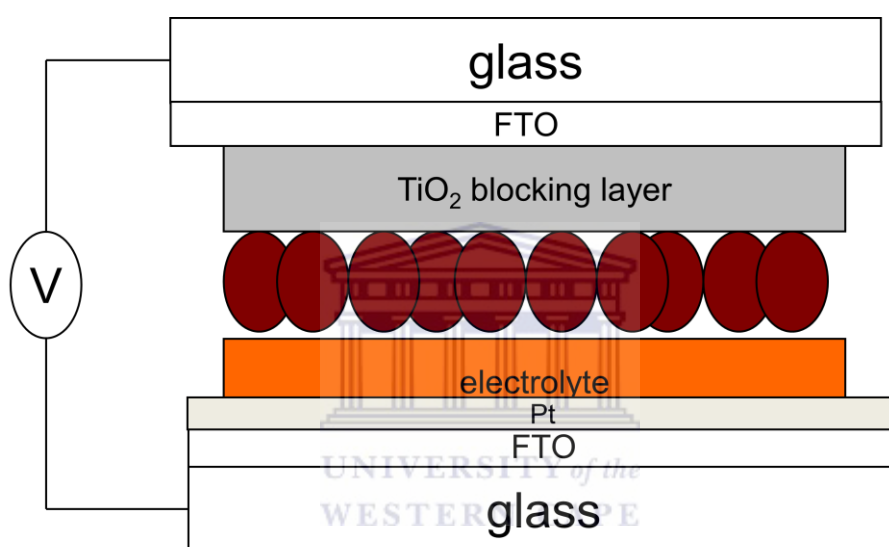
Figure 2.12: Schematic representation of the structure of a DSC with a TiO_2 nanoparticle film as the electron transport medium, as fabricated in this study

The TiO_2 nanoparticle films were prepared by doctor-blading [2.31] an even spread of a screen-printable TiO_2 paste, synthesised according to the method proposed in [2.32] onto 2 x 1.5 cm^2 fluorine doped tin-oxide (FTO)/glass substrates covered by a TiO_2 "blocking layer". The glass/FTO substrates were framed off with acrylic tape (3M magic tape) which exposed an active area of 9 x 5 mm^2. The blocking layer was prepared by dissolving 7.5 wt% titanium-

butoxide in 1-butanol, followed by magnetic stirring for 10 minutes. The solution was then spin-coated onto the glass/FTO substrate at 2000 rpm for 1 minute, succeeded by annealing at 500 ºC for 20 minutes at ambient conditions. After removing the tape, the TiO_2 nanoparticle/TiO_2 blocking layer/FTO/glass samples were sintered in a belt furnace for 25 minutes at 450 ºC, under atmospheric pressure. The TiO_2 working electrode was then coated with Al_2O_3 as described in Section 2.2.3 above. N719 dye solution was used as the light sensitiser. The solution consisted of 0.5 mM N719 dye powder (Solaronix, Switzerland) dissolved in anhydrous ethanol, magnetically stirred for 10 minutes and finally ultra-sonicated for 2 minutes. Both coated and bare TiO_2 films were soaked in the dye by placing the working electrodes in the dye solution overnight. Hereafter the electrodes are removed, rinsed with anhydrous ethanol, air dried for 1 minute and finally further dried in a stream of N_2 gas.

The counter electrode of the cell consisted of a FTO substrate coated with a thin layer of Pt. The Pt was deposited by doctor-blading a commercial Pt paste (Solaronix, Switzerland) onto the FTO covered glass substrate, followed by annealing at 500 ºC for 10 minutes in air at atmospheric pressure. The two electrodes were then sealed by means of a hot-press, using 25 µm thick Surlyn® adhesive polymer at 100ºC and a pressure of 1.5 bar. The electrolyte, which contains a commercially bought I^-/I_3^- redox couple, was then injected into the cell, where after the cell was sealed with the Surlyn®. Solar cells with an effective area of 0.45 cm^2 and dimensions allowing for efficient charge collection at the device contacts, as reported by Lee et al [2.33], were fabricated.

The structure of DSCs comprising of TiO_2 nanotubes as the electron carrier is shown in Figure 2.13 [2.12]. The nanotube films were synthesised as described in Section 2.1.3. The same procedure as was followed to coat a film of nanoparticles was then used to coat the nanotubes with a thin layer of Al_2O_3. The coated nanotube layer was then cut into 9 x 5 mm^2 rectangles and placed on a FTO covered glass support coated with a blocking layer. The Al_2O_3 coated and bare TiO_2 nanotube films were then soaked overnight in the N719 dye solution and dried in the same manner as with the nanoparticles. This was proceeded with sealing of the cell and electrolyte injection as described above.
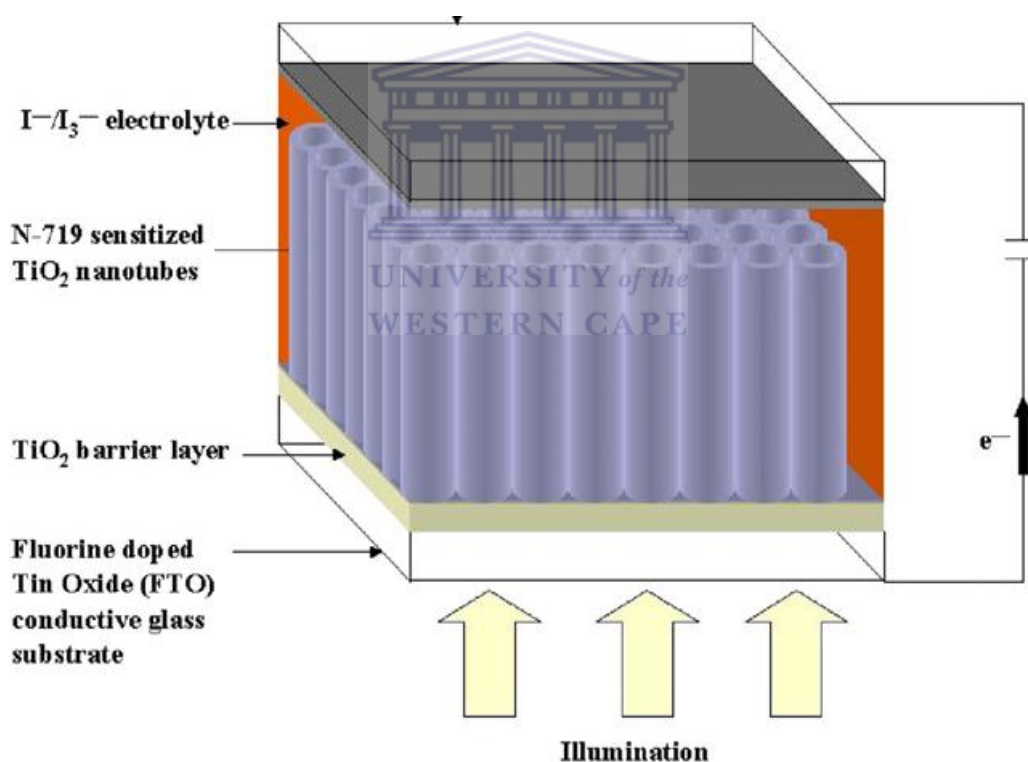
Figure 2.13: Schematic representation of the structure of a DSC with a TiO_2 nanotube film as the electron transport medium [2.12]

References

[2.1]   C. Vargel, M. Jacques and M. P. Schmidt, "*Corrosion of Aluminium –
        Chapter B. 1: The Corrosion of Aluminium*", The Netherlands, Elsevier
        Publishers, pp. 81 - 82 (2004)

[2.2]   V. P. Parkhutik, V. T. Belov and M. A. Chernyckh, Electrochem. Acta 35
        (1990) 961

[2.3]   H. Masuda and K. Fukuda, Science 268 (1995) 1466

[2.4]   H. Masuda, K. Yada and A. Osaka, Jap. J. Appl. Phys. 38 (1999) L1403

[2.5]   H. Tsuchiya and P. Schmuki, Electrochem. Commun. 6 (2004) 1131

[2.6]   I. Sieber, H. Hildebrand, A. Friedrich and P. Schmuki. Electrochem.
        Commun. 7 (2005) 97

[2.7]   H. Tsuchiya, J. M. Macak, I. Sieber, L. Taveira, A. Ghicov, K. Sirotna,
        and P. Schmuki, Electrochem. Commun. 7 (2005) 295

[2.8]   D. Gong, C. A. Grimes, O. K. Varghese, Z. Chen and E. C. Dickey, J.
        Mater. Res. 16 (2001) 3331

[2.9]   G.K. Mor, O. K. Varghese, M. Paulose, K. Shankar and C. A. Grimes,
        Sol. Ener. Mat. Sol. Cells 90 (2006) 2011

[2.10] M.R. Hoffmann, S. T. Martin, W. Choi, and D. W. Bahnemannt, Chem.
        Rev. 95 (1995) 69

[2.11] L. Gao, Q. Li, Z. Song and J. Wang, Sensors Actuat. B 71 (2000) 179

[2.12] M. Paulose, K. Shankar, O. K. Varghese, G. K. Mor and C. A. Grimes, J.
        Phys. D: Appl. Phys. 39 (2006) 2498

[2.13] J.M. Macak, H. Tsuchiya, A. Ghicov, K. Yasuda, R. Hahn, S. Bauer, P.
        Schmuki, Curr. Opinion Solid State Mater. Science 11 (2007) 3

[2.14] J.W. Schultze and M.M. Lohrengel, Electrochim. Acta 45 (2000) 2499

[2.15] J.C. Marchenoir, J.P. Loup and J. Masson, Thin Solid Films 66 (1980) 357

[2.16] L. Arsov, M. Froehlicher, M. Froment and A. Hugot-le-Goff, J. Chim. Phys. 3 (1975) 275

[2.17] L.V. Taveira, J.M. Macak, H. Tsuchiya H, L.F.P. Dick and P.J. Schmuki, Electrochem. Soc. 152 (2005) B405

[2.18] S.K. Mohapatra, M. Misra, V.K. Mahajan and K.S. Raja, J. Cat. 246 (2007) 362

[2.19] C.J. Brinker and G.W. Scherer, "*Sol-gel Science: The Physics and Chemistry of Sol-gel Processing*", San Diego USA, Academic Press Inc. (1990)

[2.20] H.K. Henisch, "*Crystal Growth in Gels*", Pennsylvania USA, Pennsylvania State University Press, p. 41 (1970)

[2.21] C.W. Turner, Ceramic Bulletin 70 (1991) 1487

[2.22] Shott AG, Mainz, Germany. 2010. Shott AG [Online], Available: http://www.schott.com/english/company/corporate_history/index.html [Accessed 12 October 2010]

[2.23] H. Schroeder, Glastech. Ber. 39 (1966) 156

[2.24] H. Dislich, P. Hiuz and R. Kaufman, FRQ Patent 1941191 (1969)

[2.25] Y. Dimitriev, Y. Ivanova and R. Iordanova, J. Univ. Chem. Tech. Metal. 43 (2008) 181

[2.26] L. Znaidi, Mat. Sci. Eng. B 174 (2010) 18

[2.27] C.J. Brinker and G.W. Scherer, "*Sol-Gel Science: The Physics and Chemistry of Sol-Gel Processing*", San Diego USA, Academic Press Inc., (1990)

[2.28] K. Wafers and C. Misra, "*Oxides and Hydroxides of Aluminium*", Pennsylvania USA, Alcoa Technical Paper 19, (1987)

[2.29] B.E. Yoldas, J. Mater. Sci. 10 (1975) 1856

[2.30] E. Palomares, J.N. Clifford, S.A. Haque, T. Lutz and J.R. Durrant, Chem. Commun. (2002) 1464

[2.31] A. Tolvanen, "*Characterisation and Manufacturing Techniques of Dye-Sensitised Solar Cells*", M.Sc. Thesis, Helsinki University of Technology, Helsinki Finland, pp. 48 – 50 (2003)

[2.32] H.-J. Koo, J. Park, B. Yoo, K. Yoo, K. Kim, N.-G. Park, Inorg. Chim. Acta 361 (2008) 677

[2.33] W.-J. Lee, E. Ramasamy, D.-Y. Lee, Sol. Energy Mater. Solar Cells 93 (2009)1448
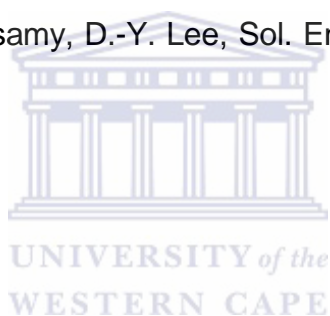
CHAPTER THREE
Analytical Techniques

This chapter will discuss the analytical techniques used to characterise the synthesised nanomaterials, dye-sensitised working electrodes and the manufactured solar cells. In particular, the fundamental physics underlying the different techniques will be addressed. Characterisation of the working electrode structure, namely the morphology, topography and crystallinity will be discussed in section 3.1. Section 3.2 will report on the various techniques used to characterise the optical properties of the TiO_2 nanostructured films, whereas section 3.3 will discuss the characterisation of the fabricated dye-sensitised solar cells.
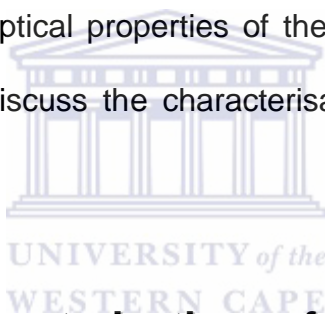
3.1 Structural Characterisation of the TiO_2 Working Electrode

3.1.1 Scanning and Focused Ion Beam Electron Microscopy

Field emission scanning electron microscopy (FE-SEM) was used to investigate the morphology and fine structure of the TiO_2 films. FE-SEM differs from conventional SEM in that the primary electrons are produced with an electric field during FE-SEM, whereas a filament is heated during conventional SEM. At the heart of an FE-SEM instrument is an extremely thin and sharp mono-crystalline tungsten crystal (tip radius between 10 and 100 nm) that produces a coherent electron beam about 1000 times smaller than in

conventional SEM. This smaller electron beam diameter yields greater resolution than that obtainable in conventional SEM microscopes, with resolutions as low as 1nm reported. The crystal functions as a cathode in front of the primary and secondary anodes. The voltage generated between the cathode and anode range between 0.5 and 30 kV under a high vacuum in the order of 10^{-7} to 10^{-9} mbar [3.1, 3.2].

The electrons emitted from the crystal, called primary electrons, are focused and deflected by electromagnetic lenses and coils to produce an extremely narrow beam, which is focused at the sample object. As the beam irradiates the sample, secondary electrons are emitted from each atom of the sample exposed to the beam. At the same time the primary electrons are either scattered or back reflected. A detector then records the secondary electrons, while a different detector detects the back-scattered primary electrons. The collected electrons are then amplified and converted into a digital image by a digital camera system connected to the different detectors. By scanning the electron beam across the sample surface, a topographical representation of the sample surface is obtained and viewed in real time on a computer screen of a desktop computer connected to the digital camera system [3.2]. Figure 3.1 shows a typical electron column of a scanning electron microscope.

A JEOL JSM 7500F FE-SEM was used in this study to investigate the structure of the TiO_2 nanotube films. The microscope was operated at electron beam energies between 1 and 10 keV. The cross-section of the nanotubes was viewed by bending the flexible anodised Ti foil in order to crack the intact film. However, cracking of the as-synthesised Ti foil before FE-SEM analyses does

not give an accurate indication of the length of the nanotube layer as this process often leads to damage of the TiO_2 film. Hence focused ion beam SEM (FIB-SEM) analysis was performed to determine whether the Ti foil substrate was completely consumed during the anodisation process.
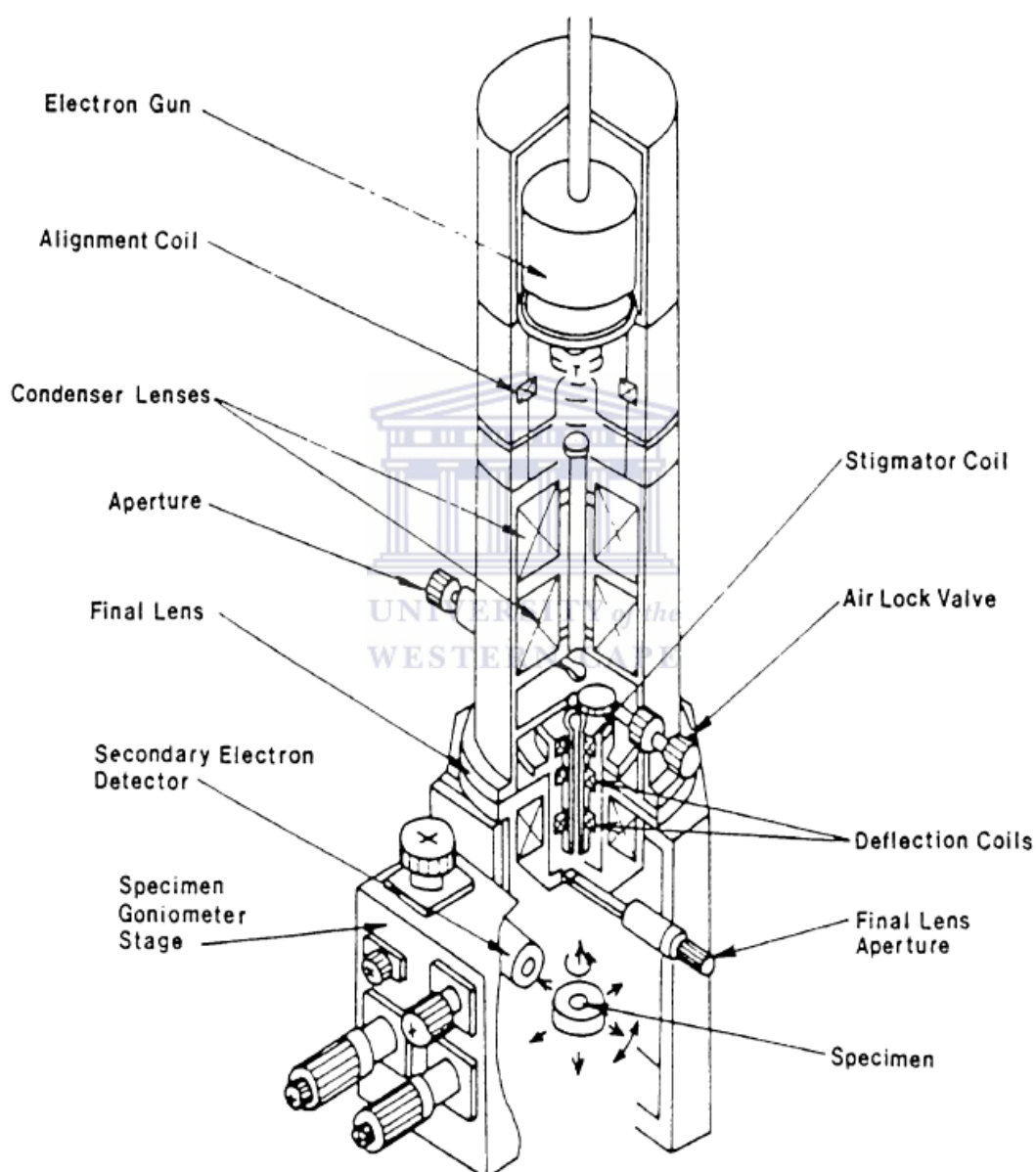
Figure 3.1: Schematic representation of the components of a SEM electron column [3.2]

Fundamentally, a focused ion beam system produces and directs a stream of high-energy ionised atoms of a relatively massive element, focusing them onto the sample both for the purpose of etching or milling the surface and as a method of imaging [3.3]. The ions' greater mass allows them to easily expel surface atoms from their positions and produces secondary electrons from the surface, allowing the ion beam to image the sample before, during, and after the lithography process. The ion beam has a number of other uses, such as the deposition of material from a gaseous layer above the sample.

Modern FIB systems utilises a liquid-metal ion source at the top of its column to produce ions, usually Ga^+. The ions are emitted and focused into a beam by an electric field and subsequently pass through apertures and scanned over the sample surface. The ion–atom collision is either elastic or inelastic. Whereas elastic collisions result in the excavation of surface atoms, a technique called sputtering or milling, inelastic collisions transfer some of the ion energy to either surface atoms or electrons, resulting in the emission of secondary electrons. Secondary ions are also emitted from the surface following the secondary electrons. Figure 3.2 shows the configuration of a typical two-beam FIB-SEM system [3.3].

A Zeiss Auriga Cobra FIB FE-SEM was utilised in this work. The sample was prepared by tilting the Ti foil at a 54º angle to the in-lens detector of the instrument, where after a layer of Pt was deposited onto the region of interest in order to protect the nanotube film during subsequent milling. An area of 10 x 20 μm^2 and up to 20 µm deep was then milled, which revealed the morphology of the intact nanotube layer.
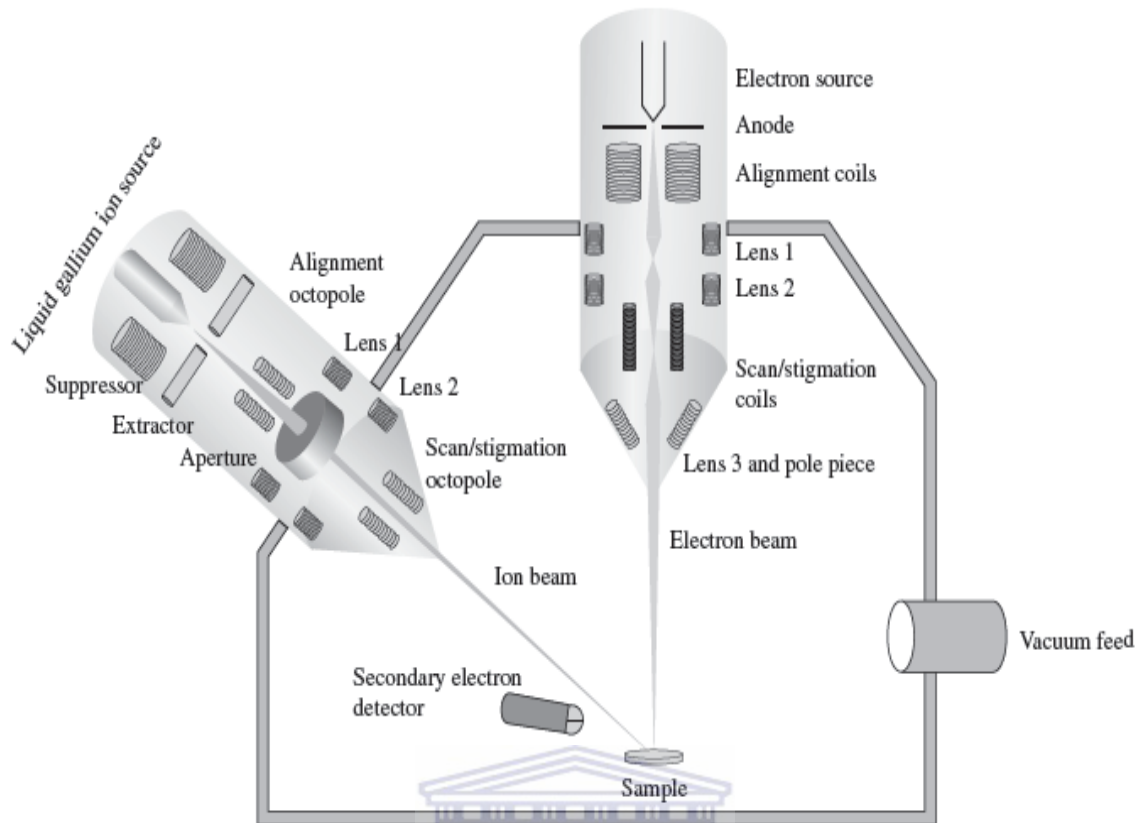
Figure 3.2: Schematic diagram of a typical two beam FIB-SEM [3.3]

3.1.2 Transmission Electron Microscopy

Transmission electron microscopy (TEM) was used to study the internal structure of the nanotubes and nanoparticles. This technique differs in principality from SEM in that the primary electron beam is transmitted through the specimen instead of being backscattered or knocking out secondary electrons in the specimen sample. By increasing the accelerating potential of the electrons to 50 kV, the electron wavelength shrinks to about 5 pm in accordance with De Broglie's relationship [3.4] and such higher-energy electrons can penetrate distances of several microns (µm) into a solid. If the solid is crystalline, the electrons are diffracted by atomic planes inside the material, yielding a transmission electron diffraction pattern. As a result of the

very small wavelength of the transmitted electrons, the specimen can be imaged at a spatial resolution much higher than is the case in a SEM [3.5, 3.6]. Modern TEMs are operated between 100 and 300 kV achieving spectral resolutions of 0.1 nm (one Angstrom) with regularity.

Image formation during TEM can be considered as occurring in two stages. Incident electrons undergo interactions with atoms of the specimen, resulting in elastic and inelastic scattering processes. The electron wavefunction which leaves the exit surface of the specimen is transmitted through the objective lens and subsequent intermediate lenses of the electron microscope to form the final enlarged image as shown in the ray diagram of Figure 3.3. Elastically scattered electrons contribute to the high resolution TEM image, whereas the inelastically scattered electrons are detected and recorded to yield valuable elemental information about the specimen during electron energy loss spectroscopy [3.5, 3.7].

A JEOL JEM-2100 HR-TEM, operated at 200 kV was employed to examine the internal structure of the samples. TEM samples were prepared dispersing the as-synthesised working electrode material in ethanol, followed by ultra-sonication for 5 minutes, where after a drop is placed on a holey-carbon copper grid and dried at ambient conditions.
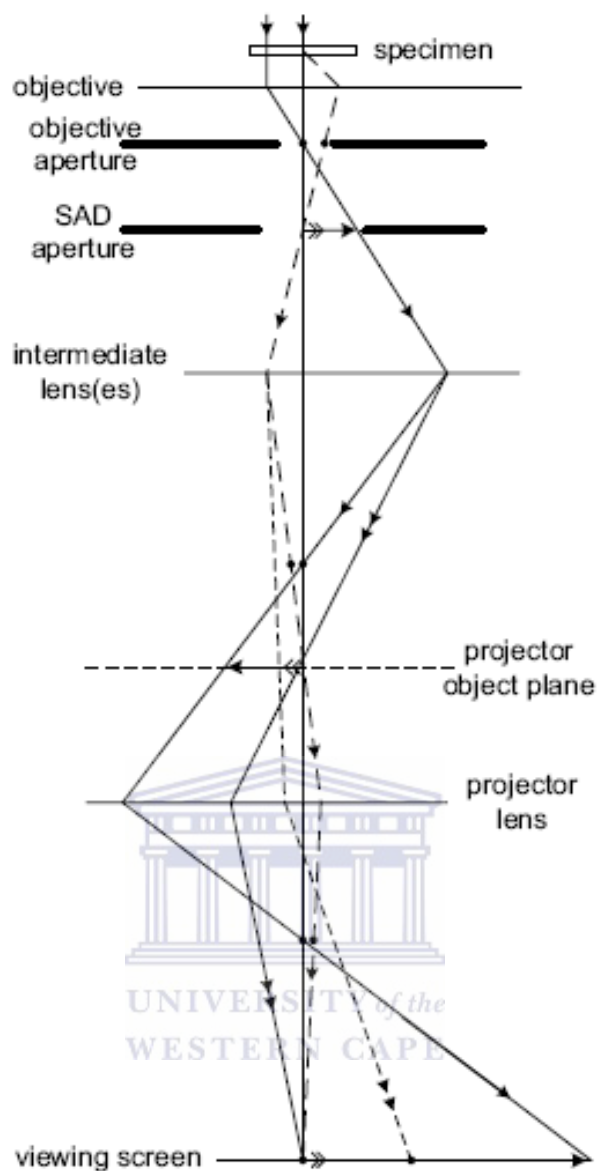
Figure 3.3: Thin-lens ray diagram of the imaging system of a TEM [3.5]

3.1.3 Atomic Force Microscopy

The working electrode surface topology and roughness were characterised by means of atomic force microscopy (AFM). The AFM was developed in the eighties primarily for nonconducting solid surfaces, but has since been developed for analyses on both conducting and non-conducting surfaces. The biggest advantage of AFM is that most samples can be investigated in their natural state, which is otherwise impossible by electron

57

microscopy methods. Figure 3.4 shows a diagram of the operating principle of a typical AFM setup. A cantilever scans the solid surface and the deflection of the cantilever is detected by the reflection of a laser beam as shown in Figure 3.4 [3.6].
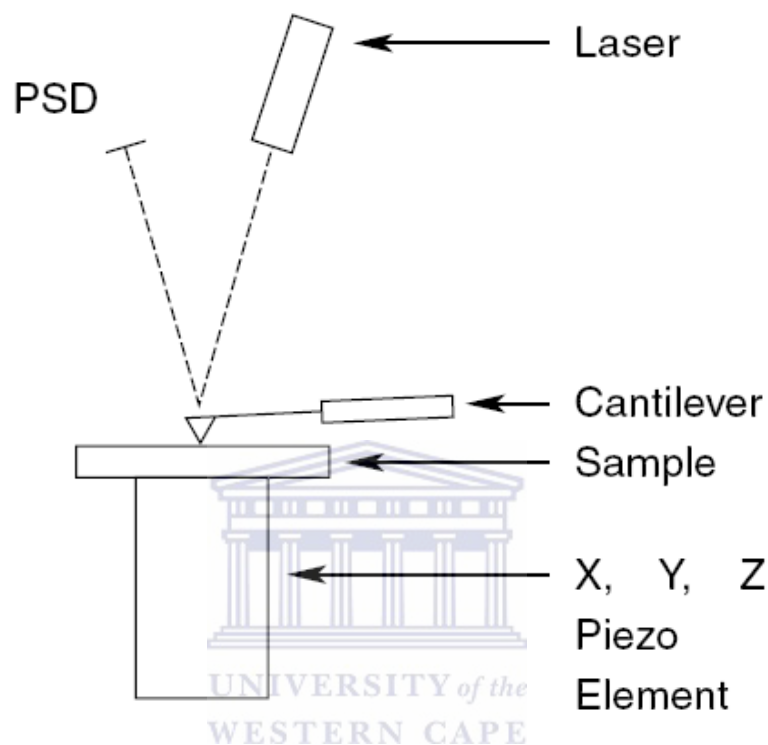
Figure 3.4:   Operating principle of an atomic force microscope [3.6]

AFM is based on the existence of a separation-dependency force between any two bodies. More specifically, the force between the tip of the cantilever and the surface bound atoms of the substrate (or specimen) is of importance in AFM. Typically, pyramidal silicon nitride tips are used, which have a radius of curvature on the order of 100 Å. The force is detected by placing the tip on a flexible cantilever that deflects proportionally to the exerted force. The deflection is then measured by some convenient procedure, such as laser reflection. In general, the AFM is operated under constant-force mode,

with forces typically in the range 0.5 to 0.1 nN. Both repulsive and attraction forces can be measured by the tip.

If the distance between the tip and the sample, r_d, is small, the force, F_r, is expressed as follows:

$$F_R = \frac{12B}{r_d^{13}} - \frac{6D}{r_d^{7}}$$ (3.1)

where B and D are constant depending upon the substrate and the tip. For small separation distances, the first term (repulsive) will dominate. The resolution is best when the tip is in contact with the substrate, due to the rapid decay of the repulsive force term. The force curve starts at a point where the different forces between the tip and sample are negligible and the cantilever is not deflected. When the tip "touches" the sample, this region is called the non-contact region. The tip is oscillating (also called AC mode or tapping mode) in the attractive force region, sensing the force without actually touching the substrate. After contact between the sample and the tip, the deflection of the cantilever follows the movement of the sample and this is called the contact region. In the non-contact mode, the net force detected is the attractive force between the tip and the substrate. On the other hand, in the contact mode, the net force measured is the sum of the attractive and repulsive forces [3.7, 3.8]. In this work, AFM images of the DSC working electrodes were acquired using a Veeco NanoScope 124 IV Multi-Mode AFM, operated in tapping mode.

3.1.4 X-Ray Diffraction

3.1.4.1 Basic Theory of X-Ray Diffraction

X-rays are electromagnetic radiation similar to light, but with much smaller wavelength and are produced when a fast moving electron is rapidly slowed down. Diffraction is a phenomenon that occurs when waves interfere with a structure whose repeat distance is about the same as that of the incident wavelength. Upon interaction constructive and destructive interference patterns result due to the scattering of the incoming wave fronts by the structure. The wavelength range of x-rays is about the same as that of the interatomic spacing found in three-dimensional crystalline structures. This implies that x-rays can be diffracted by these crystalline structures, with each atom in the crystalline structure serving as a scattering centre for the incoming wave fronts. This phenomenon is known as x-ray diffraction (XRD) and can be used as a tool for the investigation of the fine, crystalline structure of matter [3.9]. In this study, XRD was used to investigate the crystallinity of the TiO_2 films of the working electrode of the DSC.

In Figure 3.5 a monochromatic beam of parallel x-rays, O and O', strikes a stack of planes (h k l) spaced a distance d apart at an angle θ. Each plane consists of a series of equally spaced atoms, each of which is capable of scattering the incident radiation. The scattered rays P and P', resulting from the interaction of the incident beam with the atoms of the parallel planes, will recombine to form a diffracted beam if and only if their path difference is an integer multiple of wavelengths, i.e.

$$CA + AD = d\sin\theta + d\sin\theta = n\lambda \qquad (3.2)$$

or

$$2d\sin\theta = n\lambda \qquad (3.3)$$

where   n   =   integer multiple (order of diffraction)

            λ =   wavelength of the radiation

            d   =   interplanar spacing

            θ =   incident angle (Bragg angle)

Equation (3.3) is better known as Bragg's law for diffraction and gives the angle θ, at which a set of planes (h k l) of spacing d constructively reflects x-rays of wavelength λ in the nth order [3.10].
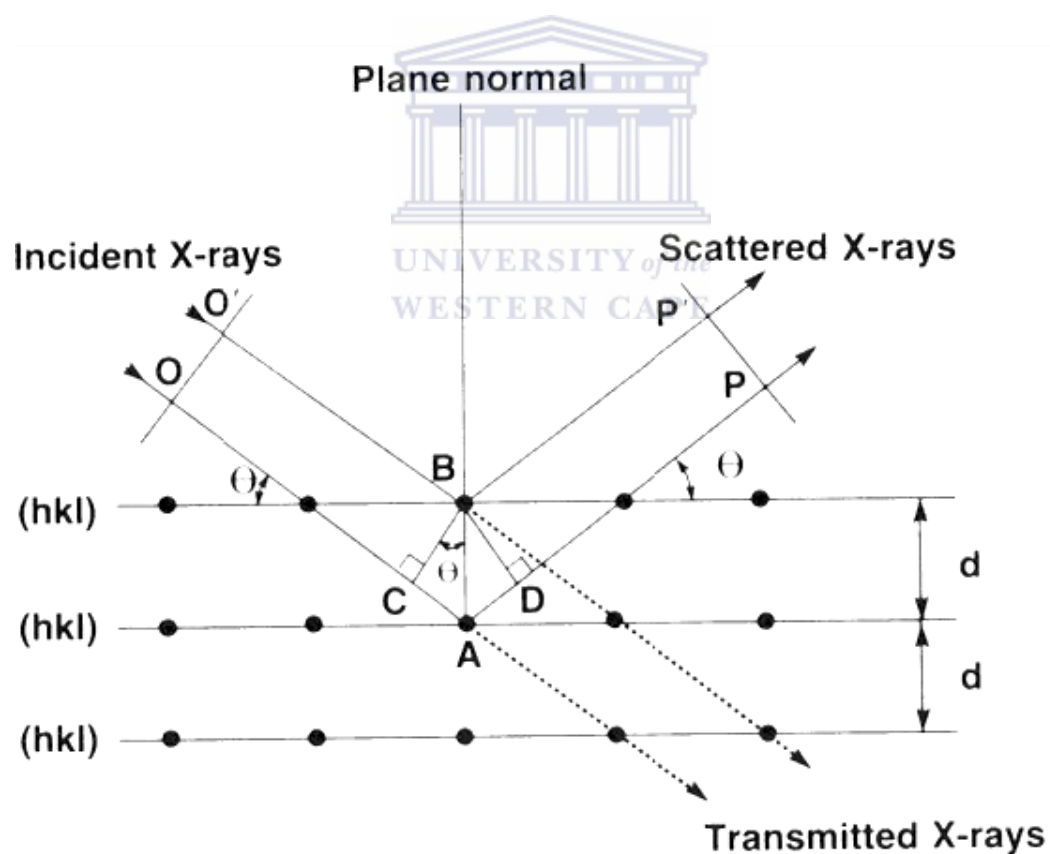
Figure 3.5:   Conditions for Bragg's law [3.9, 3.10]

3.1.4.2 Scherrer Formulation for Determination of Crystallite Size

An important analytical tool of XRD is the ability to determine the crystal size of small crystallites, by analysing the width and intensity of a diffracted x-ray peak. Bragg's law of (3.3) is based on the assumption that the incident-ray beam is composed of perfectly monochromatic and parallel radiation, which is rarely the case in reality. Consider Figure 3.6. Suppose that the crystal has a thickness, t, measured in a direction perpendicular to a particular set of reflecting planes. Let there be (m + 1) planes in this set. In this case the Bragg angle of (3.3) will be considered a variable θ_B, which exactly satisfies (3.3) for the particular values of λ and d involved. That is:

$$2d\sin\theta_B = n\lambda. \tag{3.4}$$
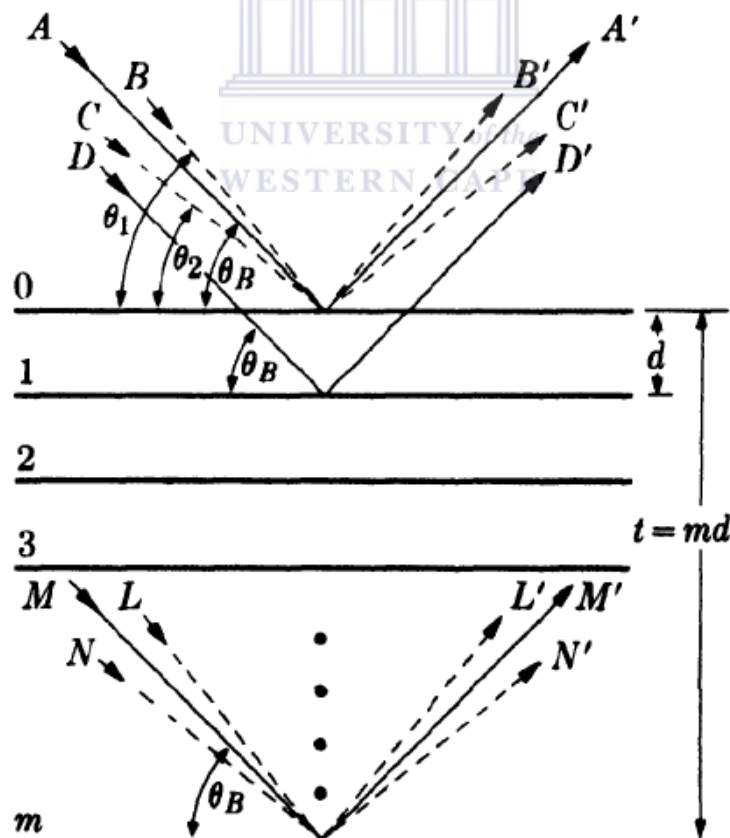
Figure 3.6: Effects of crystal size on diffraction [3.10]

62

In Figure 3.6 rays **A**, **D**,..., **M** are incident at the angle θ_B to the reflecting planes 0, 1,..., m. Ray **D'**, scattered by the first plane below the surface, is therefore one wavelength out of phase with **A'**; and ray **M'**, scattered by the mth plane below the surface, is m wavelengths out of phase with **A'**. Therefore, at a diffraction angle, $2\theta_B$ rays **A'**, **D'**,..., **M'** are completely in phase and unite to form a diffracted of maximum amplitude, i.e. a beam of maximum intensity, since the intensity is proportional to the square of the amplitude.

However, when one considers incident x-rays incident at angles slightly different from θ_B, it is found that destructive interference is not complete. For example, in Figure 3.6, ray **B** makes a slightly larger angle θ_1, such that ray **L'** from the mth plane below the surface is (m + 1) wavelengths out of phase with **B'**. This implies that midway in the crystal there is a plane that scatters a ray which is half a wavelength out of phase with ray **B'**. Subsequently, these planes cancel each other out and so do the other rays from similar pairs of planes throughout the crystal. The net effect is that rays scattered by the top half of the crystal annul those scattered by the bottom half. The intensity of the beam diffracted at an angle $2\theta_1$ is therefore zero. It is also zero at an angle $2\theta_2$ where θ_2 is such that ray **N'** from the mth plane below the surface is (m – 1) wavelengths out of phase with ray **C'** from the surface plane.

It follows that the diffracted intensity at angles near $2\theta_B$, but not greater than $2\theta_1$ or less than $2\theta_2$, is not zero but has a value intermediate between zero and the maximum intensity of the beam diffracted at an angle $2\theta_B$. Figure 3.7 shows this relationship between the diffracted intensity and $2\theta_B$ and compares it to the ideal diffraction condition implied by Bragg's law.
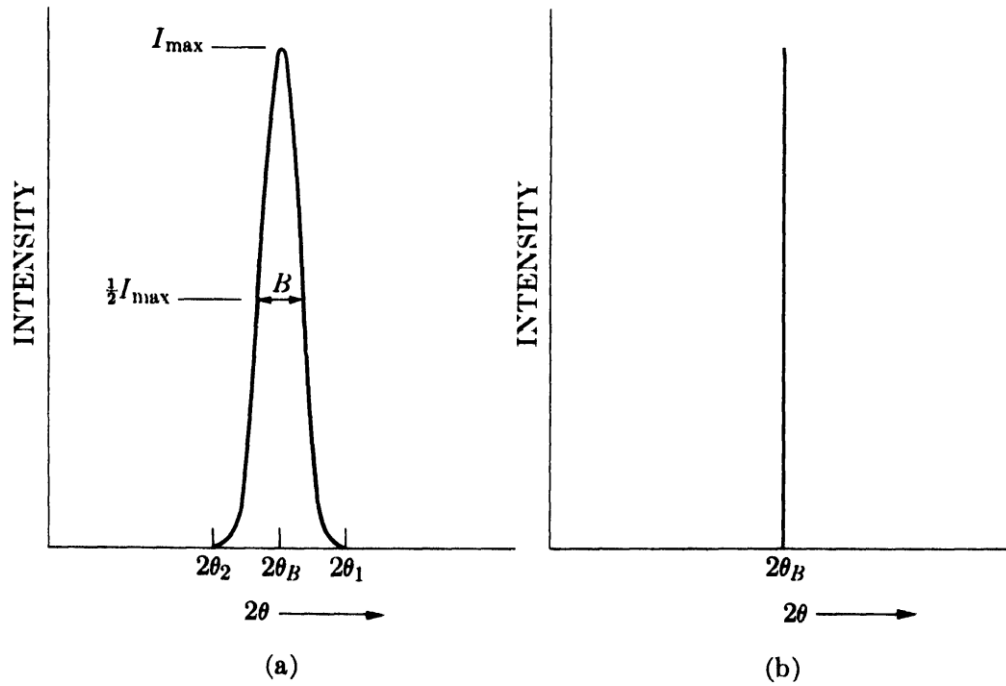
Figure 3.7: Effect of crystal size on the diffraction curve under (a) real conditions and (b) ideal Bragg conditions [3.10]

The width of the diffraction curve of Figure 3.7 (a) increases as the thickness of the crystal decreases. The width B is usually measured, in radians, at an intensity equal to half the maximum intensity. As a rough measure of B, one can take half the difference between the two extreme angles at which the intensity is zero, i.e.:

$$B = \frac{1}{2}(2\theta_1 - 2\theta_2) = \theta_1 - \theta_2$$

The path difference requirements from Bragg's law for these two angles implies that

$$2t\sin\theta_1 = (m+1)\lambda$$

$$2t\sin\theta_2 = (m-1)\lambda$$

Subtraction gives

$$t(\sin\theta_1 - \sin\theta_2) = \lambda$$

64

or

$$2t\cos(\frac{\theta_1 + \theta_2}{2})\sin(\frac{\theta_1 - \theta_2}{2}) = \lambda$$

However, θ_1 and θ_2 are both very close to θ_B, such that $\theta_1 + \theta_2 = 2\theta_B$. Also

$\sin(\frac{\theta_1 - \theta_2}{2}) = \frac{\theta_1 - \theta_2}{2}$ for small angles of θ_1 and θ_2. Thus

$$2t(\frac{\theta_1 - \theta_2}{2})\cos\theta_B = \lambda$$

or with a more thorough treatment

$$t = \frac{0.9\lambda}{B\cos\theta_B} . \qquad\qquad (3.5)$$

Equation (3.5) is known as the Scherrer formula and gives an estimate of the particle size of very small crystals from the measured width of their diffraction curves.
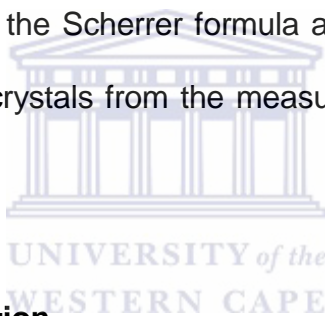
3.1.4.3 Instrumentation

X-ray diffraction patterns are recorded with an x-ray diffractometer as shown in Figure 3.8 and consists of three basic parts:

- An x-ray source (S and T in Figure 3.8)

- The diffractometer circle and

- A detector system (G and E).

The detector (G) is placed on the circumference of a circle centred at the specimen stage, C. The specimen is supported on a table H, which can rotate about an axis, O, perpendicular to this page. X-rays diverge from the source at S and are diffracted by the specimen at C to form a convergent diffracted beam, which focuses at the slit F before entering the detector at G, supported on a

carriage, E. The carriage also rotates about the axis O and has an angular position 2θ. The supports H and E are mechanically locked in a θ-2θ relationship. A and B are special slits that define and collimate the incident and diffracted beams. A filter is placed in the diffracted beam-path to suppress the K_β radiation and to decrease the background radiation originating in the specimen. In this work the XRD spectra were recorded with a PANalytical X'Pert Pro diffractometer, operated at 45 kV and 40 mA at the source. Copper, $K_{\alpha 1}$ radiation with a wavelength of 1.5406 Å was used as the x-ray source.
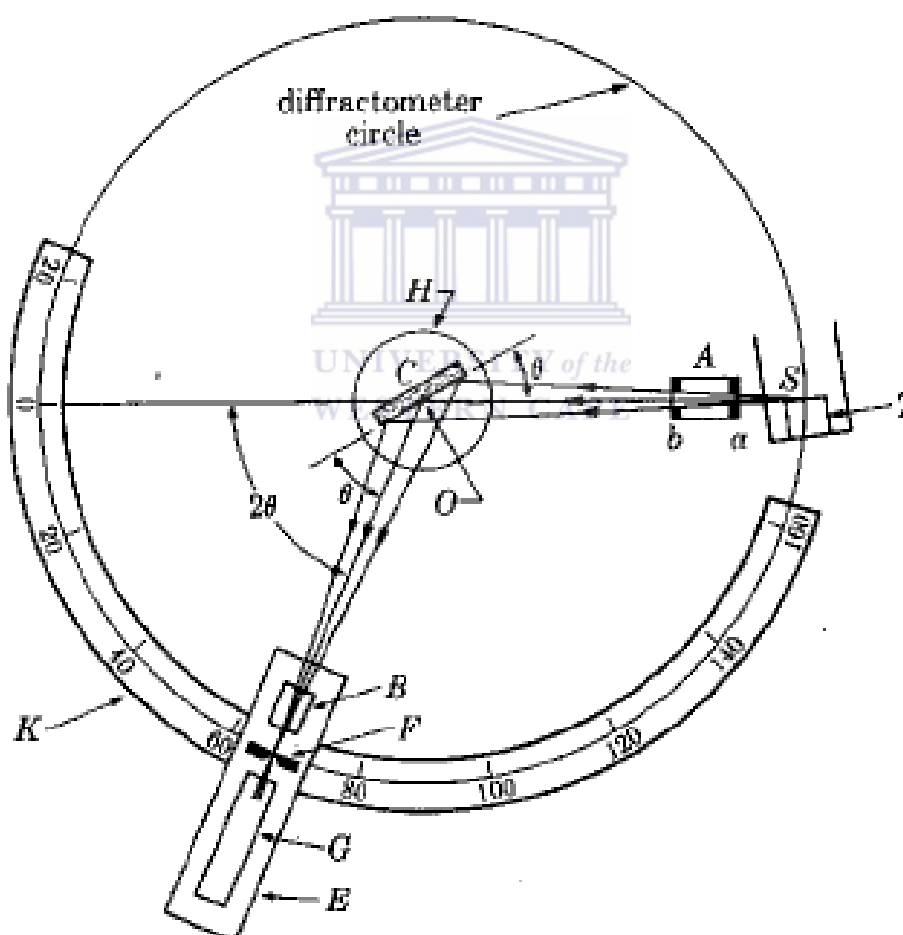
Figure 3.8: X-ray diffractometer [3.10]

3.2 Optical Characterisation of the TiO$_2$ Working Electrode

3.2.1 Raman Spectroscopy

3.2.1.1 Basic Theory of Raman Spectroscopy

Scattered radiation is released when the light wave, which can be considered as an oscillating dipole, transfers its energy to the molecule, subsequently distorting (polarising) the electrons around the nuclei of the molecule causing it to go to a higher energy state. This interaction can be considered as the formation of a 'complex' between the light energy and the electrons in which the nuclei of the molecule do not have enough time to move appreciably. This complex is not stable, resulting in the light being released almost immediately as scattered radiation [3.11].

Two types of scattering exist. The most intense form is Rayleigh scattering, which occurs when the electron cloud relaxes without any nuclear movement. This process is essentially elastic since no appreciable change in energy of the molecule. On the other hand, Raman scattering, which is a much rarer event, occurs when the light and the electrons interact and the nuclei begin to move at the same time. Since the nuclei are much heavier than the electrons, there is an appreciable change in energy of the molecule to a lower or higher energy. This depends on whether the electron was initially in the ground state or in a vibrationally excited state; when the molecule is initially in the ground state the process is known as Stokes scattering, whereas when the

67

molecule starts off in an excited state, anti-Stokes scattering occurs. Figure 3.9 shows these two scattering processes compared to Rayleigh scattering.
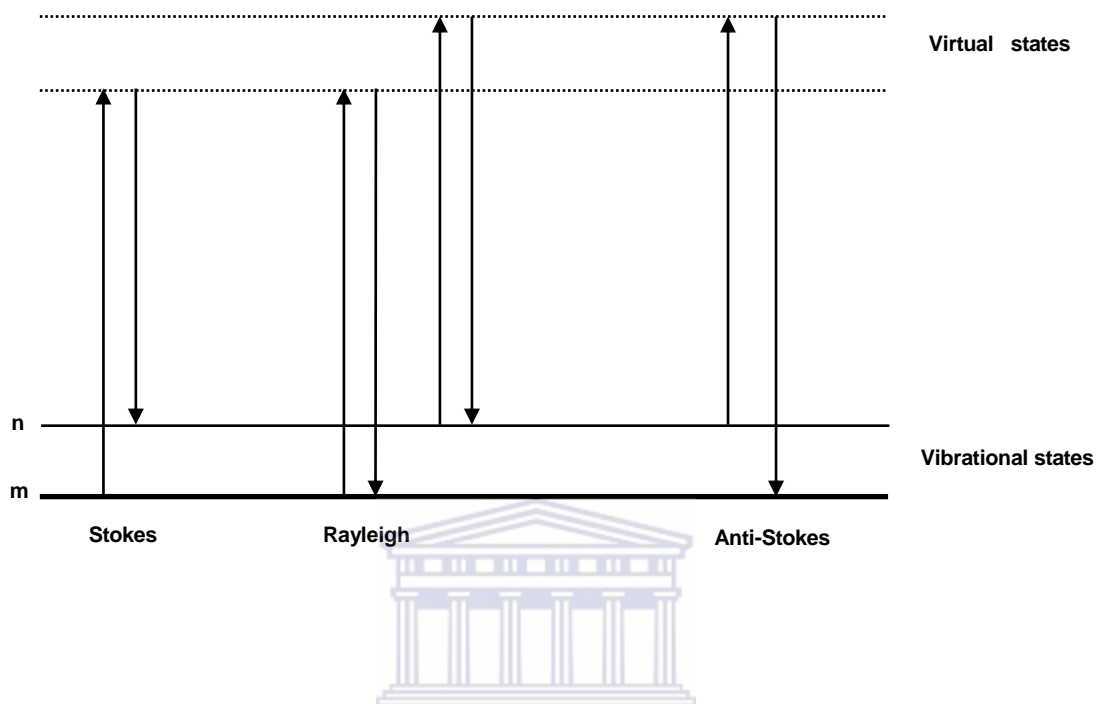
Figure 3.9: Diagram of the Rayleigh and Raman scattering processes [3.11]

3.2.1.2 Size Dependent Optical Properties of Nanomaterials

Surface atoms in materials behave differently from those in the bulk of the material. Figure 3.10 shows that a surface atom at position A has fewer neighbouring atoms than a bulk atom at position B in the material. As a result there atom A contains "unshared" electrons, whereas the electrons of atom B are fully bonded. The unshared atoms of atom B in Figure 3.10 are known as dangling bonds and the main reason behind the differing mechanical, vibrational, electronic and consequently, optical properties of surface atoms to that of atoms in the material bulk [3.12].
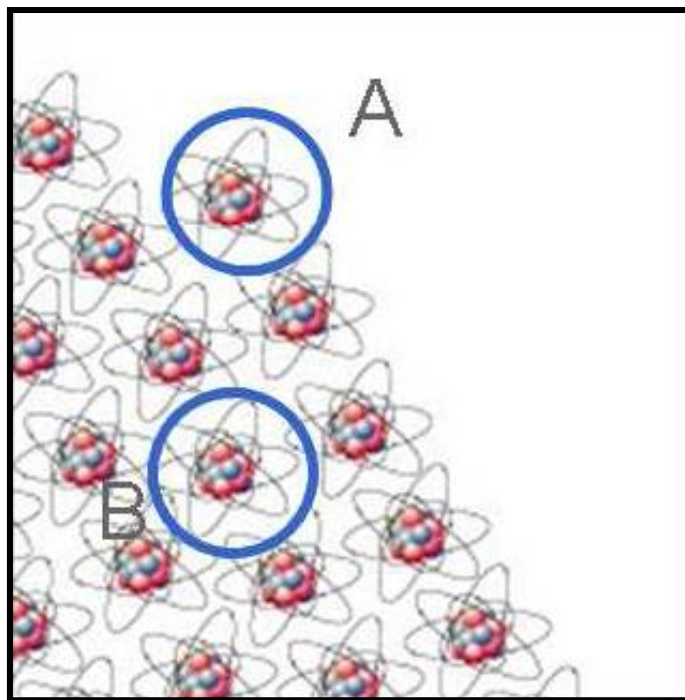
Figure 3.10: Schematic illustration of the difference between surface and bulk atoms. In 2 dimensions surface atoms are each surrounded by a 3 other atoms whereas the inner (bulk) atoms are surrounded by 6 atoms [3.12]

The proportion of surface atoms to those in the bulk material, i.e. N_{surf}/N_{bulk} can be represented by the ratio, σ_{surf}, which essentially represents the surface area to volume ratio of the material. An isolated atom can be classified as a surface atom since it contains no surrounding neighbouring atoms. As the number of atoms aggregate the number of bulk atoms increase (i.e. N_{bulk}) and consequently σ_{surf} decreases. The expressions for σ_{surf} for the most commonly found shapes that materials can adopt are illustrated in Figure 3.11. It can be seen that as the dimensions of the structure decrease, the value of σ_{surf} increases very rapidly.

rod/ wire	$\left(\sigma_{surf}\right)_{rod} = \dfrac{2}{l} + \dfrac{2}{r}$	
sphere	$\left(\sigma_{surf}\right)_{sphere} = \dfrac{3}{r}$	
cube	$\left(\sigma_{surf}\right)_{cube} = \dfrac{6}{a}$	
cuboid	$\left(\sigma_{surf}\right)_{cuboid} = \dfrac{2}{a} + \dfrac{2}{b} + \dfrac{2}{c}$	
strip/ belt/	$\left(\sigma_{surf}\right)_{ribbon} = \dfrac{2}{a} + \dfrac{perimeter}{area_{bc}}$	
disc	$\left(\sigma_{surf}\right)_{disc} = \dfrac{2}{a} + \dfrac{2}{r}$	
sheet/ film	$\left(\sigma_{surf}\right)_{sq.disc} = \dfrac{2}{a} + \dfrac{4}{b}$	
solid cone/ tip	$\left(\sigma_{surf}\right)_{tip} = 3\left(\dfrac{s}{rh} + \dfrac{1}{h}\right)$	
horn/ cone	$\left(\sigma_{surf}\right)_{horn} = \dfrac{3}{h\delta r}(s+r)$	
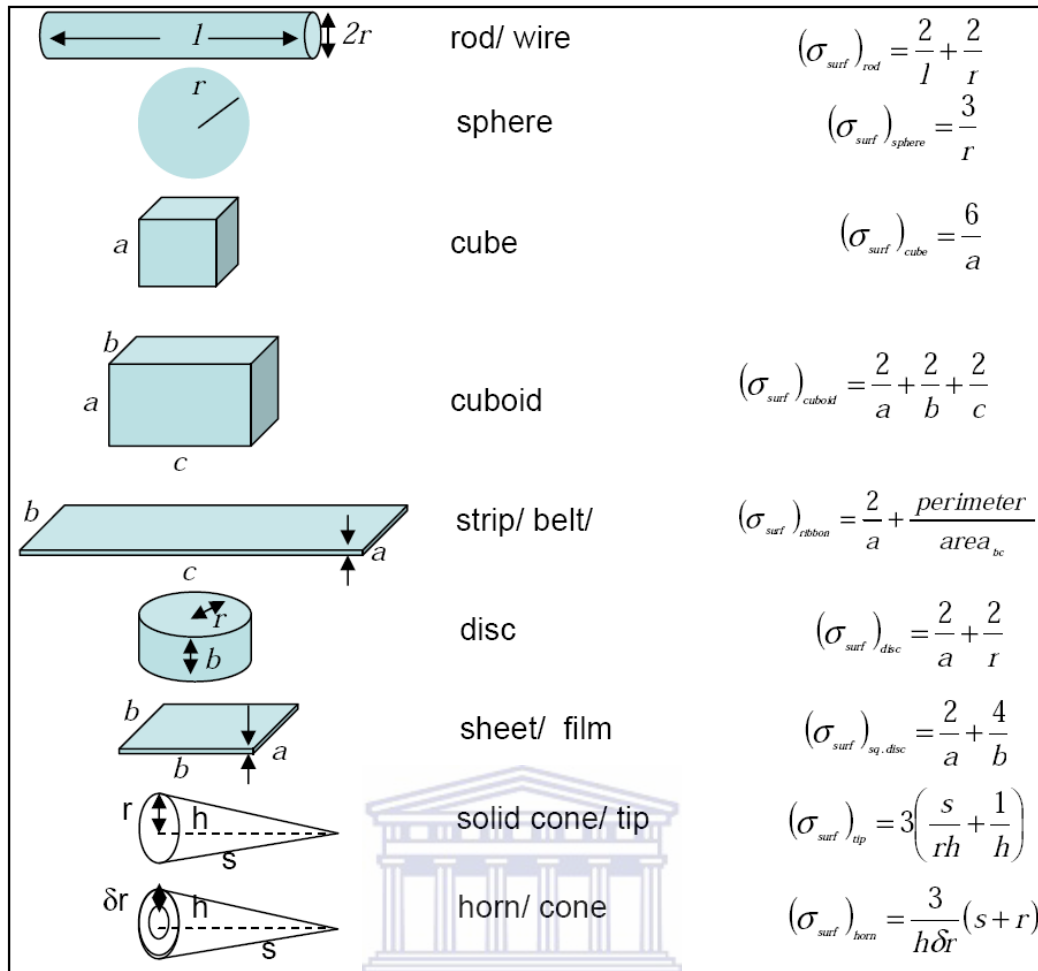
Figure 3.11: The surface to volume ratio of the most commonly found structures [3.12]

It became apparent in the eighties that the Raman lineshapes for micro-crystals did not follow the perfect Gaussian profile as predicted by Stokes. Hence there was a need for deeper understanding of the origin of this asymmetry. Spatial correlation modelling, as it was called, became one way to extract information from Raman spectroscopy data. The justification is that, for a perfect (bulk) crystal of diameter d having vibrational modes of momentum q, the Heisenberg's uncertainty principle ($\delta d. \delta q \sim h$) means that as $\delta d \rightarrow \infty$ (bulk) then $\delta q \rightarrow 0$ (the "q = 0" selection rule applies). Conversely, as the diameter $\delta d \rightarrow 0$ (nano-metric) then the vibrational momentum $\delta q \rightarrow \infty$. In

70

this case, the "q = 0" selection rule breaks down, since a contribution from the **q** ≠ 0 phonons, determined by the dispersion relation ω(**q**) is allowed. This accounts for the asymmetric line broadening of the peaks in a Raman spectrum. Richter et al. [3.13] developed what is commonly referred to as the phonon confinement (PC) model for nanosized crystals in the late seventies and published their results in 1981. This model was later developed to include the Gaussian distribution of the phonon momenta and particle size by Fauchet and Campbell [3.14] and is given by

$$I(\omega) = A_0 \int_{-\infty}^{\infty} \frac{|c(0,q)|^2}{(\omega_0 - \omega(q))^2 + (\Gamma_0 / 2)^2} \, d^3q \qquad (3.6)$$

In equation (3.6), Γ_0 is the full-width at half-maximum (FWHM) of the Raman peak for the bulk material, ω(q) is the phonon dispersion curve relation (PDR) for the material and A_0 is a coefficient dependent on the material. The Richter model is valid for spherical nano-crystals of mean diameter d for which the Fourier coefficient c(0,q) was assumed to be Gaussian of the form $\exp(-q^2d^2/14\pi^2)$ with a phonon amplitude at the boundary of 1/e. Campbell & Faucet modified the Richter model to (1) remove the non-physical boundary condition of 1/e and (2) tried other values to check the effect of other particle-size distribution functions. It was found that in general for spherical particles, the function c(0,q) can be written as

$$|c(0,q)|^2 = \frac{d^6}{16(2\pi)^2 \alpha^3} \exp \left(\frac{q^2 d^2}{2\alpha} \right) \qquad (3.7)$$

where d is the crystallite size, q is the wave vector and α is a constant. Balaji et al. [3.15] used values of α = 8π², Γ_0 = 7.5 cm⁻¹ and ω_0 = 142.5 cm⁻¹ in their

71

studies on PC in nano-crystalline anatase TiO_2 thin films. In order to evaluate the effect of the TiO_2 crystallite size on the dispersion and ultimately the confinement of the phonon modes in the material, the Balaji group employed a modified version of the weighted average of phonon dispersions proposed by Ivanda et al. [3.16], given as

$$\omega(q) = \omega_0 + \Delta \sin^2(\frac{q\pi}{x})$$ (3.8)

with $\omega_0 = 142.5$ cm^{-1}, $\Delta = 164$ cm^{-1} and $x = 1.51779$ was employed. The values of Δ and x determine the amount of dispersion in $\omega(q)$.

Red-shift in the Raman spectral line owing to the particle size has been well observed by Zi et al. [3.17] in Si nanocrystals of spherical and columnar shapes with sizes from 5 nm down to 1 nm. Red-shifts up to 30 cm^{-1} have been reported for nanocrystals of diameter of 1 nm. The PC model of equation (3.6) failed to explain the Zi et al. data on Si nanocrystals. Therefore they used what is known as the bond polarizability model (BPM) [3.18, 3.19] to derive another confinement model given by

$$\omega_{vib}(d) = \omega_0 - A(a/d)^\beta$$ (3.9)

where d is the particle size, ω_{vib} is the new peak position due to particle size, ω_0 is the original peak position, A and β are constants that are attributes of the geometry of nano-crystal and a is a parameter determined by fitting of equation (3.9) to experimental data. According to Zi et al., for spherical Si nano-crystals $A = 44.41$ cm^{-1} and $\beta = 1.44$ whereas for columnar shapes one has $A = 20.92$ cm^{-1} and $\beta = 1.08$.

3.2.1.3 Phonon Confinement in TiO$_2$ Nanotubes
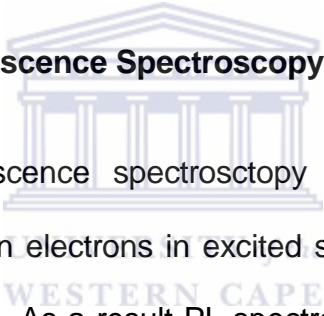
Not a lot of literature report on the size dependent optical properties of novel anodised TiO$_2$ nanotubes. This is a crucial gap, since TiO$_2$ is almost extensively used in DSCs because of its unique photo-electrochemical properties. In the case of TiO$_2$ nanoparticles and thin films it is well reported that a decrease in the diameter of the crystallites results in enhanced quantum confinement. Subsequently, these confinement effects alter the measured optical properties, especially the bandgap of the material [3.15, 3.20 – 3.24]. This level of detail is not reported for TiO$_2$ nanotubes synthesised via anodisation.

On the few publications that indeed report on PC in TiO$_2$ nanotubes, Lai et al. [3.25] observed a blue shift in the absorption edge of the ultraviolet-visible (UV-vis) absorption spectra as the diameter of the TiO$_2$ nanotubes decreased. These observations were attributed to quantum confinement effects, caused by the decrease in nanotube diameter. However a thorough explanation is not provided. Mor et al. [3.26] reported an absorption coefficient of 2.303 for a nanotube film of thickness 340 nm on a glass substrate and an average refractive index of 1.66 in the visible range. In addition, a porosity of 66.5% and an increase in the bandgap to 3.34 eV were obtained for these purely anatase structures. These findings were also attributed to quantum confinement induced by the 12 nm wall thickness of the nanotube film. Yet, a thorough treatment of the problem was not pursued. Further studies by Ge et al. [3.27] also revealed a blue shift in the fundamental UV-Vis absorption edge with decreasing inner diameter of anodised TiO$_2$ nanotubes and the results were ascribed to the

effects of quantum confinement. However, the presence of both rutile and anatase crystallites was also provided as a possible reason for the decrease in the absorption edge, which contradicts their notion of quantum confinement.

These findings show the uncertainty that exists in quantifying the structure-related optical properties of these porous nanotube structures. Contrary to nanoparticles, the complex morphology of anodised TiO_2 nanotubes has proved to be more difficult to investigate and currently pose as the biggest reason for the varying results on the optical properties, as presented above.

3.2.1.4 Photoluminescence Spectroscopy

During photoluminescence spectrosctopy (PL) atoms emit light by spontaneous emission when electrons in excited states drop down to a lower level by radiative transitions. As a result PL spectroscopy has proved to be an important technique in the characterisation of the optical energy bands of materials and the study of surface states, donor/acceptor states and structure-induced trapping states present within the band gap of materials. Furthermore, it is also well known that PL spectra are greatly affected by changes in size of nanomaterials. Hence this technique proves to be an invaluable tool during phonon confinement studies of nanomaterials, and was made use of in this study. A Horiba Jobin-Yvon iHR 320 Nanolog, equipped with a Symphony® cryogenic detector for high spectral resolution was employed to record the PL spectra, with an excitation wavelength of 325 nm at room temperature

3.2.1.5 Instrumentation

Figure 3.12 shows a typical set-up for Raman spectroscopy. A monochromatic visible laser is used as the excitation source. The laser is passed through a pinhole, measured by a spectrometer and then collected as an expanded parallel beam. This is done in order to fill the optics of the microscope. The radiation is then deflected by mirrors towards the notch filter, which reflects the light into the microscope. After interaction of the light with the sample the scattered radiation is collected from the microscope back through the same optics. The scattered radiation then passes through the notch filter at an angle that allows transmission of the scattered radiation. This radiation is then passed through a grating and onto the charge coupled device (CCD) detector [3.9]. In this work the Raman spectra were measured with a Horiba Jobin-Yvon HR800 micro-Raman spectrometer with a spectral resolution of 0.33 cm^{-1}. In all measurements an excitation wavelength of 514 nm was directed perpendicular to the substrate and the spectra were recorded in reflection geometry.
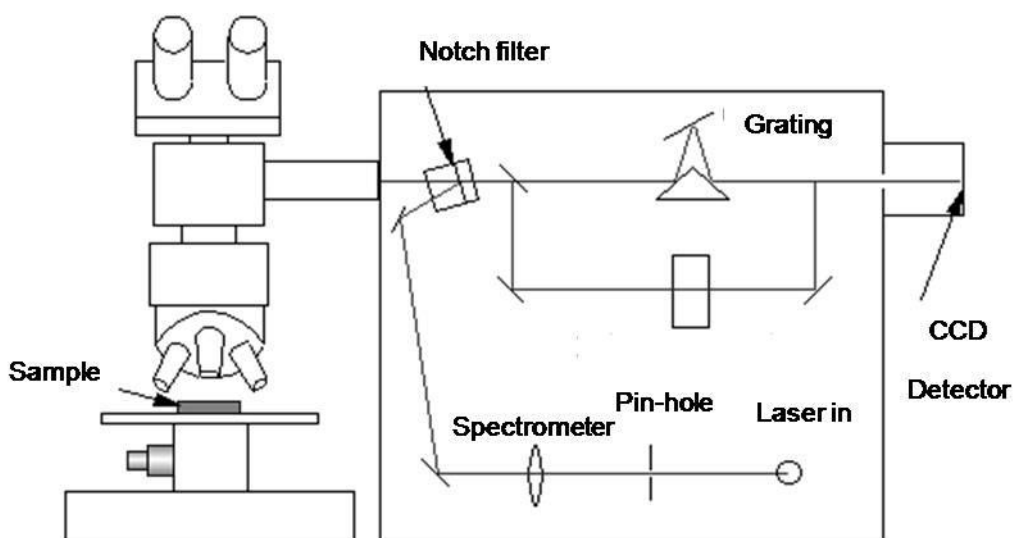
Figure 3.12: Typical set-up for Raman spectroscopy

3.2.2 Ultraviolet-Visible Spectroscopy

3.2.2.1 Theory

Semiconductors and insulators have a fundamental absorption edge in the near-infrared, visible or ultraviolet spectral region. This absorption edge exists as a result of the onset of optical transitions across the fundamental band gap of the material, E_g. During ultraviolet-visible (UV-vis) spectroscopy, investigation of the fundamental absorption edge located in the UV to visible wavelength range is pursued. Figure 3.13 shows a simplified energy diagram of two separated bands in a solid. The gap in energy between the two bands is called the band gap, E_g. Interband transitions are only possible across E_g if the selection rules permit them. The lower band is commonly referred to as the valence band, whereas the top band is known as the conduction band. The valence band edge is referred to as E_V and the conduction band edge is labelled E_C.

During a transition an electron jumps from the band at lower energy to the one above it by absorbing a photon. This can only happen if there is an electron in the initial state in the lower band. Furthermore, the Pauli exclusion principle demands that the final state in the upper band must be empty. By applying the law of conservation of energy to the interband transition shown in Figure 3.13 it follows that

$$E_f = E_i + \hbar\omega \tag{3.10}$$

where E_i is the energy of the electron in the lower band, E_f is the energy of the final state in the upper band and $\hbar\omega$ is the photon energy.
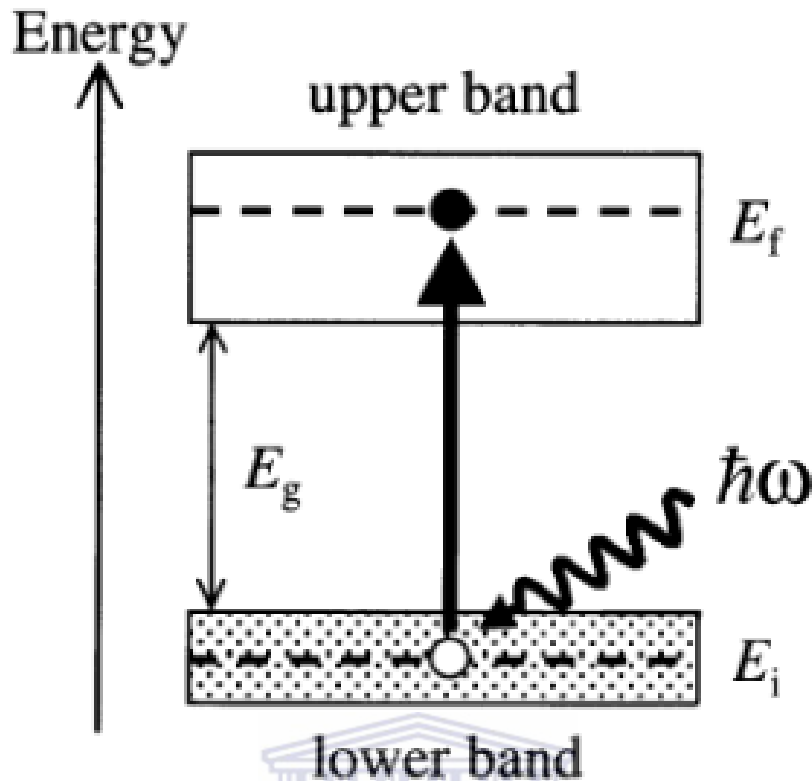
Figure 3.13: Interband optical absorption between an initial state of energy E_i in an occupied lower band and a final state at energy E_f in an empty upper band. The energy difference between the two bands is E_g [3.28]

The excitation of the electron leaves the initial state at energy E_i in the valence band unoccupied. The interband absorption process therefore creates a "hole" in the initial state and an electron in the final state; and may be considered as the creation of an "electron-hole" pair. The band gap of a material may be either direct or indirect, as illustrated by the energy band diagram of Figure 3.14.
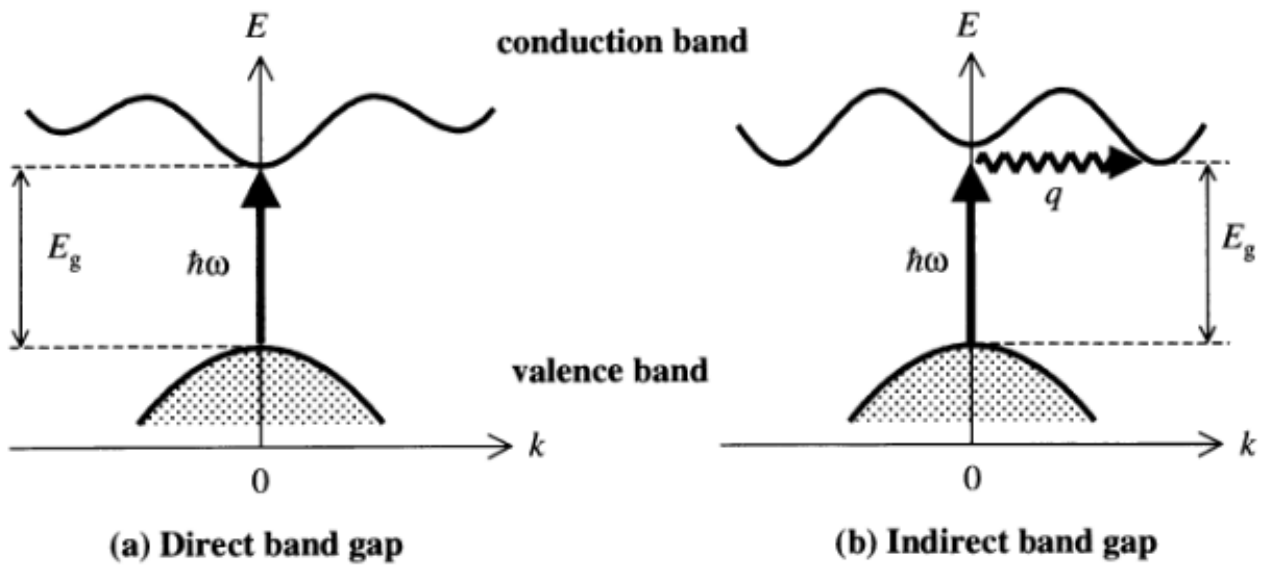
Figure 3.14: Interband transitions in (a) direct band gap and (b) indirect band gap materials [3.28]

In a direct gap material, the valence band maximum and the conduction band minimum coincide at the Brillouin centre where k = 0, whereas in an indirect gap material the maximum and minimum do not occur at k = 0, but at some value for k close to the zone edge. Conservation of momentum implies that the electron wave vector, **k**, does not change significantly during a photon absorption process. It can be seen from Figure 3.14(b) that **k** must change significantly in transiting from the valence band to the bottom of the conduction band in indirect band gaps. It is not possible to make this transition by absorption of photon alone and therefore the transition must involve a phonon to conserve momentum. This contrasts with a direct gap material in which the process may take place without any phonons being involved.

78

3.2.2.2 UV-Vis Desorption Method

For evaluating the concentration of Ru dye adsorbed onto both the TiO_2 nanoparticle and nanotube films, the spectroscopic information obtained from UV-vis spectra were analysed in accordance with the desorption method developed by Tolvanen [3.1]. Tolvanen found that a plot of the dye concentration, c, against the UV-vis absorbance peak maximum, A, yields a straight line, given by

$$c = 91.48A - 0.18$$

(3.11).

Equation (3.11) implies that, if the concentration of dye adsorbed onto two different TiO_2 films is kept constant, then the absorbance at a certain wavelength should also be constant, given that the two films share the same thickness and ultimately surface area. Hence, equation (3.11) can be used as a tool to deduce and compare the surface area of two differing shapes of TiO_2 films. The absorbance spectra reported on in this work were recorded with a Perkin Elmer Elmer LAMDA 750S UV-vis spectrometer at over a spectral range of 400 nm to 700 nm.

3.3 Characterisation of the DSC Performance

3.3.1 Electrochemical Impedance Spectroscopy

3.3.1.1 Introduction

During electrochemical impedance spectroscopy (EIS) the complex AC resistance over a wide range of frequencies, typically between 10^{-2} and 10^6 Hz, is investigated. The complex resistance in question is called the impedance $Z(\omega)$ and is dependent on the frequency, υ and thus the angular frequency $\omega = 2\pi\upsilon$. The impedance is determined by applying a small sinusoidal AC voltage on the system and measuring the resulting AC current. The amplitude of the AC voltage has to be small enough so that the resulting current is proportional to the voltage and has harmonic time dependence.

EIS is widely employed to investigate the internal processes and phase boundaries within the DSC. The different microscopic processes within the cell have different time constants, which are reflected in different frequency ranges in an impedance spectra. For example, the diffusion of electrons through the redox electrolyte is much slower than the charge transfer at the counter electrode of the cell, and thus would appear at different frequency ranges in the impedance spectra.

3.3.1.2 Basic Theory of Electrochemical Impedance Spectroscopy

The basic theory of EIS is best presented through use of a simple electrochemical cell, depicted by an equivalent circuit composed of resistors and capacitors that pass current with the same amplitude and with the same phase that the real cell does under a given excitation. Figure 3.15 shows a very common equivalent circuit, called a Randles equivalent circuit, where i_f and i_c represent the faradaic processes and double layer charging, respectively. The double layer charging is nearly purely capacitive and is thus represented by a capacitance element, C_d. The faradaic processes, in contrast, are represented by a general impedance, Z_f. R_Ω represents the solution resistance that the current must pass through, as well as the other sources of series resistance. The faradaic impedance, Z_f, is comprised of a series resistance R_s and a pseudo-capacity, C_s. The faradaic impedance can also be sub-divided into a charge-transfer resistance, R_{ct}, and a another general impedance, Z_w, called the Warburg impedance, which is related to the mass transfer within the cell.
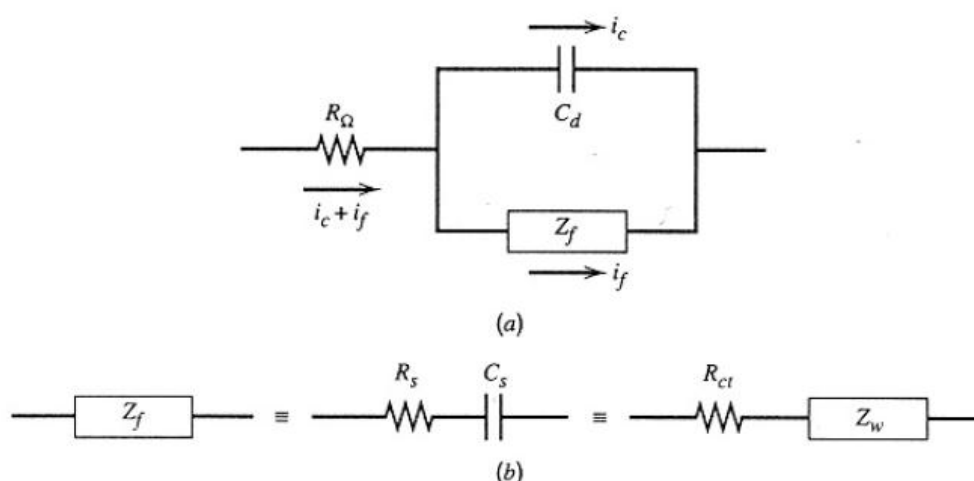
Figure 3.15: Schematic representation of (a) the Randles equivalent circuit and (b) sub-division of the faradaic impedance Z_f

Impedance, $Z(\omega)$, is a complex quantity comprising of real and imaginary components, i.e.

$$Z(\omega) = Z_{Re} - jZ_{Im} \qquad (3.12)$$

with $j = \sqrt{-1}$. The real part of $Z(\omega)$ represents the resistive behaviour of the system under investigation, $Z_{Re} = R_B$ and the imaginary part the capacitance, i.e. $Z_{Im} = \frac{1}{\omega C_B}$. By adding the impedances in the Randles equivalent circuit of Figure 3.15, the following expression for the total impedance in the system is obtained:

$$Z(\omega) = Z_{R\Omega} + \frac{Z_{Cd}Z_f}{Z_{Cd} + Z_f} \qquad (3.13)$$

The real and imaginary parts of each of the impedances in the circuit is given by

$$\begin{aligned}
Re(Z_{R\Omega}) &= R_\Omega; \quad Im(Z_{R\Omega}) = 0 \\
Re(Z_{Cd}) &= 0; \qquad Im(Z_{Cd}) = \frac{1}{j\omega C_d} \\
Re(Z_f) &= R_s; \qquad Im(Z_f) = \frac{1}{j\omega C_s}
\end{aligned} \qquad (3.14)$$

Substituting equations (3.14) into 3.13, and separating the real and imaginary parts for $Z(\omega)$, yields:

$$Re[(Z(\omega)] = R_\Omega + \frac{R_s}{A^2 + B^2} \qquad (3.15)$$

where $A = \frac{C_d}{C_s} + 1$ and $B = \omega R_s C_d$ for the real part of $Z(\omega)$. Similarly the imaginary part of $Z(\omega)$ is given by

$$Im[(Z(\omega)] = \frac{B/\omega C_d + A/\omega C_s}{A^2 + B^2} \qquad (3.16)$$

The relationships for the series resistance, R_s and pseudo-capacitance, C_s in Figure 3.15 are given by [3.29]

$$R_s = R_{ct} + \sigma\omega^{\frac{-1}{2}}$$
$$C_s = \frac{1}{\sigma\omega^{\frac{1}{2}}}$$

(3.17)

where σ is a constant dependent on the concentrations, diffusivities and temperature residing in the system under investigation. Substituting the relations of equation (3.17) into the real and imaginary parts of $Z(\omega)$ in equations (3.15) and (3.16), respectively gives two very important equations.

$$Z_{Re} = R_\Omega + \frac{R_{ct} + \sigma\omega^{\frac{-1}{2}}}{(C_d\sigma\omega^{\frac{1}{2}} + 1)^2 + \omega^2 C_d^2 (R_{ct} + \sigma\omega^{\frac{-1}{2}})^2}$$

(3.18)

$$Z_{Im} = \frac{\omega C_d (R_{ct} + \sigma\omega^{\frac{-1}{2}})^2 + \sigma\omega^{\frac{-1}{2}}(\omega^{\frac{1}{2}}C_d\sigma + 1)}{(C_d\sigma\omega^{\frac{1}{2}} + 1)^2 + \omega^2 C_d^2 (R_{ct} + \sigma\omega^{\frac{1}{2}})^2}$$

The equations of (3.18) can be simplified by studying the behaviour of the frequency, ω at low and high regions. At low frequencies, $\omega \to 0$ and thus

$$Z_{Re} = R_\Omega + R_{ct} + \sigma\omega^{\frac{-1}{2}}$$
$$Z_{Im} = \sigma\omega^{\frac{-1}{2}} + 2\sigma^2 C_d$$

(3.19)

Eliminating $\sigma\omega^{\frac{-1}{2}}$, known as the Warburg impedance, from (3.19) yields

$$Z_{Im} = Z_{Re} - R_\Omega - R_{ct} + 2\sigma^2 C_d$$

(3.20)

Thus plotting Z_{Im} versus Z_{Re} gives a linear plot with unit slope at low frequencies and is characteristic of a diffusion controlled process. At high frequencies ranges, diffusion is less predominant and thus the Warburg impedance becomes negligible. This implies that the Z_w impedance in Figure 3.15 can be left out of the equivalent circuit, and thus the total impedance in the circuit will be given by

$$Z = R_\Omega - j\left(\frac{R_{ct}}{R_{ct}C_d\omega - j}\right) \qquad (3.21)$$

The real and imaginary parts are

$$Z_{Re} = R_\Omega + \frac{R_{ct}}{1 + \omega^2 C_d^2 R_{ct}^2}$$

$$\qquad (3.22)$$

$$Z_{Im} = \frac{\omega C_d R_{ct}^2}{1 + \omega^2 C_d^2 R_{ct}^2}$$

Elimination of ω from equations (3.22) and rearranging the terms gives

$$(Z_{Re} - R_\Omega - \tfrac{R_{ct}}{2})^2 + Z_{Im}^2 = (\tfrac{R_{ct}}{2})^2 \qquad (3.23)$$

which is the equation of a circle centred at $Z_{Re} = R_\Omega - R_{ct}/2$ and $Z_{Im} = 0$, and with a radius of $R_{ct}/2$. Combining the low and high frequency ranges, an impedance plot such as shown in Figure 3.16 is obtained. The plot of Z_{Im} versus Z_{Re} is called a Nyquist plot and will be exclusively used in this study for data representation.
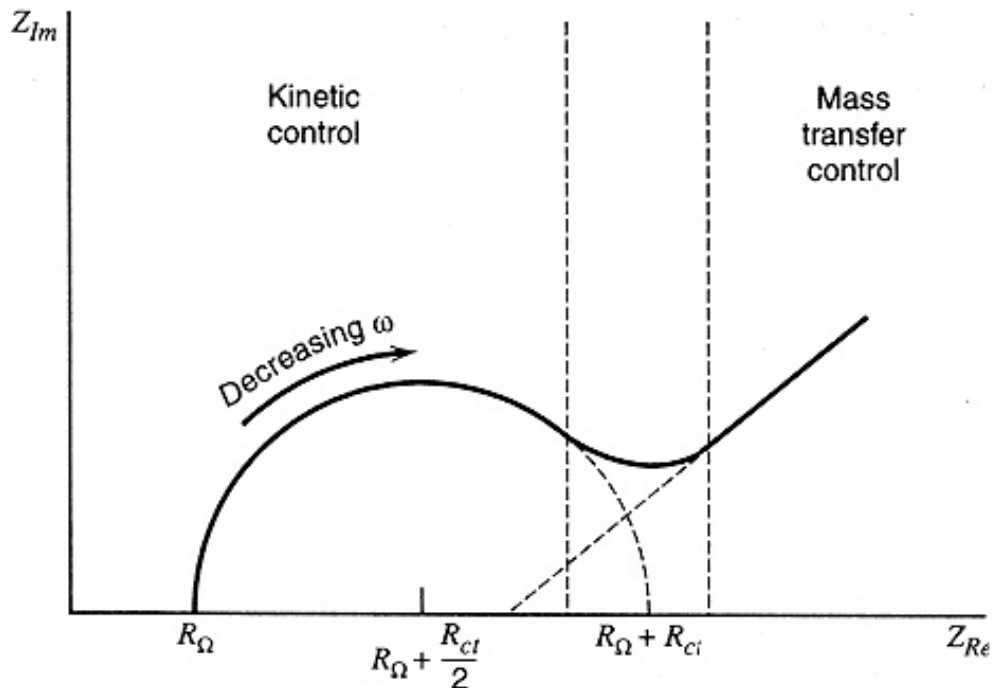
Figure 3.16: Nyquist plot for an electrochemical system [3.1, 3.29]

3.3.1.3 Instrumentation

The EIS spectra measured in this study were recorded with a Autolab PGSTAT 12/30/230 potentiostat. A two electrode configuration was used where the sensitised TiO_2 was connected as the working electrode while the platinised counter electrode of the solar cell, doubled as the reference electrode. The measurements were carried out both in the dark and under illumination at an open circuit potential of 700 mV and a scan rate of 50 mV/s.

3.3.2 Current – Voltage Characterisation

3.3.2.1 Simple Electrical Model of a Dye-sensitised Solar Cell

A solar cell can be thought of as a combination of a current source and a diode, as shown in Figure 3.17. In an ideal cell the series resistance, R_s, would be zero and the parallel or shunt resistance, R_p, indefinitely large. However, in reality this is not the case. The series resistance is composed of the electrical resistances of the different materials in the cell and the interfaces between them - the resistance of the TCO layer is the biggest contributor to the series resistance of the cell. The shunt resistance measures the resistance between the electrodes through undesirable routes, e.g. from the TiO_2 film to the electrolyte, hence in a highly efficient cell the shunt resistance must be as high as possible.
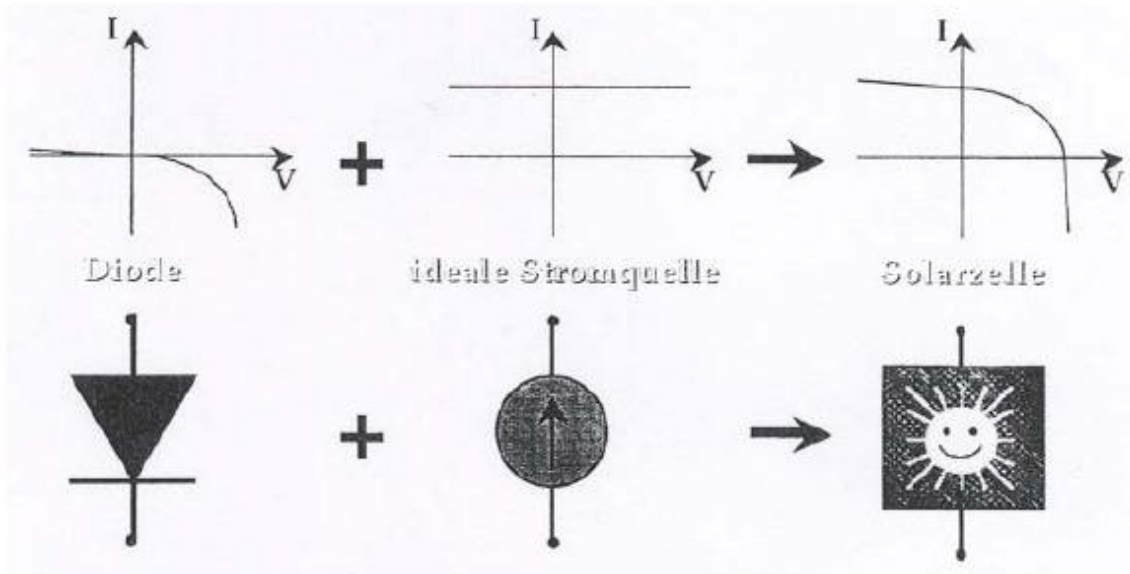
(a)
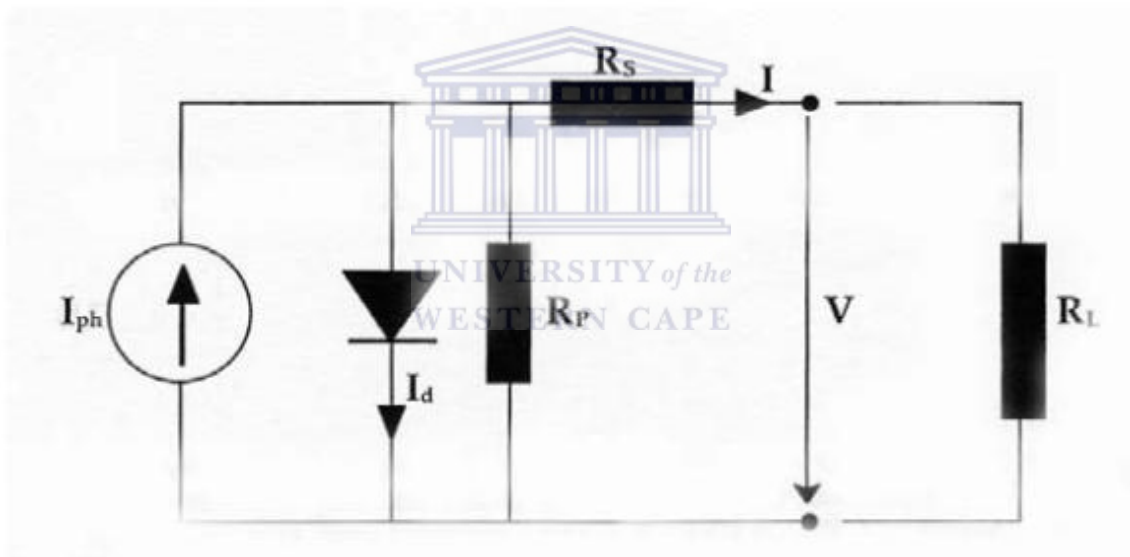
(b)

Figure 3.17: (a) Illustration that a solar cell can be represented by a current source and a diode and (b) the simple electrical circuit by which a solar cell can be modelled

3.3.2.2 I-V Characteristics of a Dye-sensitised Solar Cell

A typical current-voltage (I – V) curve of a solar cell is shown in Figure 3.18. In general the current density, defined as the current (I) per unit area, and labelled j, is plotted against the voltage. Nevertheless, the current density-voltage relationship is referred to as an I – V curve. The important feaures in Figure 3.18 are the short-circuit current density j_{sc}, the open-circuit voltage V_{oc} and the maximum power point P_{max} (or MPP) with its corresponding current-density and voltage (j_{mp}, V_{mp}).
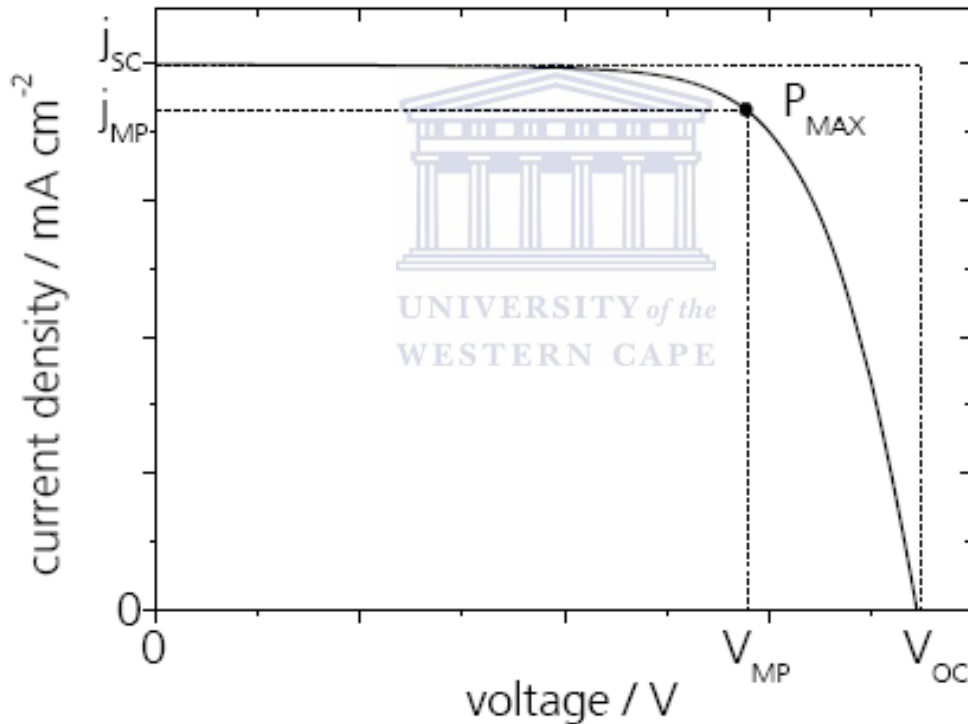
Figure 3.18: Typical I-V curve of a solar cell [3.30]

The fill factor, FF, of the solar cell is defined as "squareness" of the I-V curve and is given by

$$FF = \frac{P_{max}}{j_{sc} V_{oc}}$$

(3.24)

with P_{max} given in W/cm^2. The efficiency of the cell, η is given by

$$\eta = \frac{P_{max}}{P_{in}} = FF \times \frac{j_{sc}V_{oc}}{P_{in}}$$

(3.25)

where P_{in} is the power of the incident irradiation given in W/cm^2.

The power output of a solar cell is highly dependent on the power of the incident irradiation. Under standard reporting conditions (SRC) the cell is illuminated with AM 1.5 global light. It is equivalent to the spectrum of the sun with an incident angle, such that the light path through the atmosphere is 1.5 times longer than the path for perpendicular incident irradiation. The intensity of AM 1.5 global is 100 mW/cm² or 1000 W/m² and is also referred to as 1 sun [3.30].
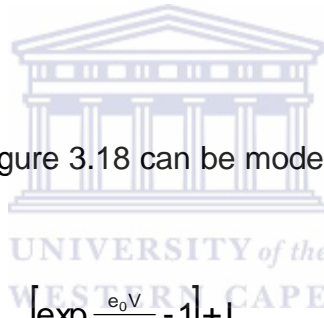
The I – V curve of Figure 3.18 can be modelled by the one-diode model, given by

$$I(V) = I_{sat}\left[\exp\frac{e_0 V}{m_D k_B T} - 1\right] + I_{sc}$$

(3.26)

where I_{sat} = the diode saturation current,

e_0 = electron charge

m_D = diode ideality factor,

k_B = Boltzmann constant and

T   = temperature

The diode ideality factor is 1 from semiconductor theory. However, real diodes deviate from the ideal diode equation where $m_D = 1$. In real silicon diodes the ideality factor is 2 for low currents and 1 for high currents. The one-diode model is sometimes also called the "standard solar cell equation". Many detailed models have been developed to describe the I – V curve of a DSC

from microscopic parameters [3.31. 3.32]. However, it is sufficient to describe the macroscopic I – V curve of a DSC by the one-diode model [3.30]. In a real solar cell the series, R_s and shunt, R_{sh} resistances have to be taken into account, as shown in Figure 3.17. The I – V curve then becomes

$$I(V) = I_{sat}\left[\exp \frac{e_0V - e_0R_sI}{m_Dk_BT} - 1\right] + I_{sc} + \frac{V - R_sI}{R_{sh}} \tag{3.37}$$

with the quantity, $\dfrac{V - R_sI}{R_{sh}}$ known as the shunt current, I_{sh}. The influence of the series and shunt resistances on the I-V curve of a solar cell is shown in Figure 3.19.
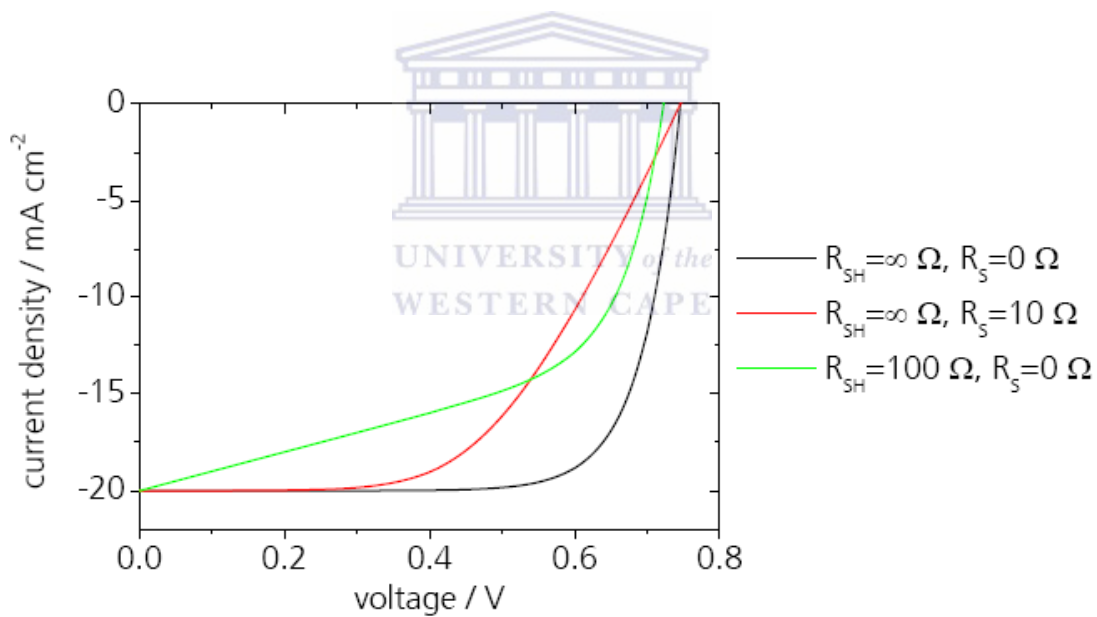
Figure 3.19: Effect of R_s and R_{sh} on the I-V curve of a solar cell [3.30]

89

It can be seen from Figure 3.19 that low shunt resistances (typically in the region of 100 Ω) increase the slope of the "flat" part of the I-V curve, whereas high series resistances decrease the slope of the "ascending" part of the curve. Hence, a direct measure of these two quantities can be obtained from calculating the inverse of the slope of the tangent line at these two parts of the I – V curve. At infinitely high shunt and zero shunt resistances, I_{sh} in equation 3.37 becomes negligible and the I – V relation tends towards that of the ideal diode, i.e. equation (3.36).

3.3.2.3 Instrumentation

The I – V characteristics of the DSCs were measured under illumination using a Keithley 2420 supply and measure unit. The devices were irradiated at 100 mW.cm^{-2} using a xenon lamp-based Sciencetech SF150 150 W solar simulator equipped with an AM1.5 filter as the white light source. The power intensity at the sample was measured with a Daystar light meter. All the photovoltaic properties were evaluated in ambient air conditions at room temperature. To eliminate the influence of diffused and back-reflected light during the I – V measurements, the DSC was covered with a black aperture mask according to the methods proposed in [3.33, 3.34].

References

[3.1]   A. Tolvanen, "*Characterisation and Manufacturing Techniques of Dye-Sensitised Solar Cells*", M.Sc. Thesis, Helsinki University of Technology, Helsinki Finland, pp. 48 – 50 (2003)

[3.2]   P. J. Goodhew and F. J. Humphreys, "*Electron Microscopy and Analysis, 2nd Edition*", Taylor & Francis, London (1988)

[3.3]   N. Yao, "*Focused Ion Beam Systems: Basics and Applications*", Cambridge University Press, New York USA, pp. 15 – 30 (2007)

[3.4]   R.F. Egerton, "*Physical Principles of Electron Microscopy: An Introduction to TEM, SEM and AEM*", Springer, USA (2005)

[3.5]   P.J. Goodhew, J. Humphreys and R. Beanland, "*Electron Microscopy and Analysis, 3rd Edition*", Taylor and Francis, London UK (2001)

[3.6]   N. Yao and Z.L. Wang, "*Handbook of Microscopy for Nanotechnology*", Kluwer Academic Publishers, New York USA (2005)

[3.7]   K.S. Birdi, "*Scanning Probe Microscopes: Applications in Science and Technology*", CRC Press LLC, Florida USA (2003)

[3.8]   S. Kalinin and A. Gruverman, "*Scanning Probe Microscopy: Electrical and Electrochemical Phenomena at the Nanoscale, Vol. 2*", Springer, NY USA (2007)

[3.9]   F.R. Cummings, "*Hot-wire Chemical Vapour Deposition of Carbon Nanotubes*", M.Sc. Thesis, University of the Western Cape, Cape Town South Africa (2007)

[3.10] B. D. Cullity, "*Elements of X-ray Diffraction*", Addison-Wesley Publishing Company, Massachusetts USA (1978)

[3.11] E. Smith and G. Dent, "*Modern Raman Spectroscopy: A Practical Approach*", Wiley and Sons Ltd, Sussex England (2005)

[3.12] B. Mwakikunga, "*Nano-size Effects on Opto-Electronic, Structural and Vibrational Properties of Vanadium and Tungsten Oxides Produced by Laser and Ultrasonic Spray Pyrolysis Techniques*" Ph.D. Thesis, University of Witwatersrand, Johannesburg South Africa (2009)

[3.13] H. Richter, Z.P. Wang and L. Ley, Sol. Stat. Commun. 39 (1981) 625

[3.14] P.M. Fauchet and I.H. Campbell, Crit. Rev. Solid. State Mater. Sci. 14 (1998) S79

[3.15] S. Balaji, Y. Djaoued and J. Robichaud, J. Raman Spec. 37 (2006) 1416

[3.16] M. Ivanda, S. Music, M. Gotic, A. Turkovic, A. M. Tonejc and O. Gamulin, J. Molec. Struct. 480 – 481 (1999) 641

[3.17] J. Zi, H. Buscher, C. Falter, W. Ludwig, K. Zhang and X. Xie, Appl. Phys. Lett. 69 (1996) 200

[3.18] A.A. Maradudin and Bernstein, Phys. Rev. 164 (1981) 1081

[3.19] S. Go, H. Bilz, and M. Cardona, Phys. Rev. Lett. 34 (1975) 580

[3.20] S. Kelly, F.H. Pollak, M. Tomkiewicz, J. Phys. Chem. B 101 (1997) 273

[3.21] M. Gotić, M. Ivanda, S. Popović, S. Musić, A. Sekulić, A. Turković, K. Furić, J. Raman. Spec. 28 (1997) 555

[3.22] D. Bersani, P.P. Lottici, T. Lopez, J. Sol-Gel Science Tech. 13 (1998) 849

[3.23] H.C. Choi, Y.M. Jung, S.B. Kim, Vibrational Spectroscopy 37 (2005) 33

[3.24] B. Liu, L. Wen, X. Zhao, Mat. Chem. Phys. 106 (2007) 350

[3.25] Y.K. Lai, L. Sun, C. Chen, C.G. Nie, J. Zuo, C.J. Lin, Appl. Surf. Science 252 (2005) 1101

[3.26] G.K. Mor, O.K. Varghese, M. Paulose, C.A. Grimes, Adv. Funct. Mater. 15 (2005) 1291

[3.27] R. Ge, W. Fu, H. Yang, Y. Zhang, W. Zhao, Z. Liu, C. Wang, H. Zhu, Q. Yu, G. Zou, Mat. Lett. 62 (2008) 2688

[3.28] M. Fox, "*Optical Properties of Solids*", Oxford University Press, New York USA (2001)

[3.29] A.J. Bard and L.R. Faulkner, "*Electrochemical Methods: Fundamentals and Applications, 2nd Edition*", Wiley and Sons, New York USA (2001)

[3.30] R. Sastrawan, "*Photovoltaic Modules of Dye Solar Cells*", Ph.D. Thesis, Albert-Ludwig University, Freiburg Germany (2006)

[3.31] J. Ferber, J. Luther, J. Phys. Chem. B 105 (2001) 4895

[3.32] R. Stangl, J. Ferber, J. Luther, Solar Energy Mat. Solar Cells 54 (1998) 255

[3.33] J. Park, H.-J. Koo, B. Yoo, K. Yoo, K. Kim, W. Choi, N.-G. Park, Sol. Energy Mater. Sol. Cells 91 (2007) 1749

[3.34] S. Ito, K. Nazeeruddin, P. Liska, P. Comte, R. Charvet, P. Péchy, M. Jirousek, A. Kay, S.M. Zakeeruddin, M. Grätzel, Prog. Photovolt: Res. Appl. 14 (2006) 589

CHAPTER FOUR
TiO$_2$ Nanotube Synthesis and Properties

In this chapter the synthesis of TiO$_2$ nanotubes by means of anodisation, as discussed in Chapter Two, as well as the crystallinity and optical properties of the nanotubes will be presented. The morphology of the nanotubes is of importance for their application in the DSC. The nanotubes were synthesised in two different electrolytes, one an aqueous solution with a low pH, and the other an organic, neutral electrolyte.

The physical dimensions, such as length, diameter and wall thickness of the nanotubes were varied by having accurate control over the anodisation parameters, namely voltage, fluoride ion concentration, time and electrode separation distance in each electrolyte.

Characterisation of the optical properties of the nanotubes is also a very important before implementation of the nanotubes in the DSC, as the presence of trapping states in the optical bandgap of the material influences the performance of the device.

4.1 Morphology

4.1.1 Effect of Electrolyte Solution on the Morphology

Figure 4.1 compares the SEM micrographs of the Ti sheets anodised in (a) the aqueous solution comprising of 0.15 M NH_4F + H_3PO_4 + H_2O with a pH of 3.4 (solution A), and (b) the organic solution consisting of 0.15 M NH_4F + 2M H_2O + ethylene glycol (EG) with pH 7.5 (solution B). The anodisation was performed at an operating voltage of 25 V for three hours.

For each experiment a fresh electrolyte solution was prepared and no agitation of the solution by means of ultra-sound or magnetic stirring was applied. This was done since the results from previous such experiments during this study showed inconsistencies in the morphology of the Ti sheet after anodisation due to the erratic interaction of the F^- ions with the Ti surface, caused by the agitation of the electrolyte solution.

The nanotubes synthesised in the acidic and organic electrolytes have an average length of approximately 500 and 1000 nm, respectively as shown by the size-distribution histograms in Figure 4.1. Closer inspection reveals that solution A yields nanotubes with rippled side-walls, whereas the walls of the tubes obtained from solution B are in general smoothed. Measurement of the respective nanotube inner diameter (or nanopores) also shows that the tubes synthesised in the former solution are greater than when anodised in the organic electrolyte.
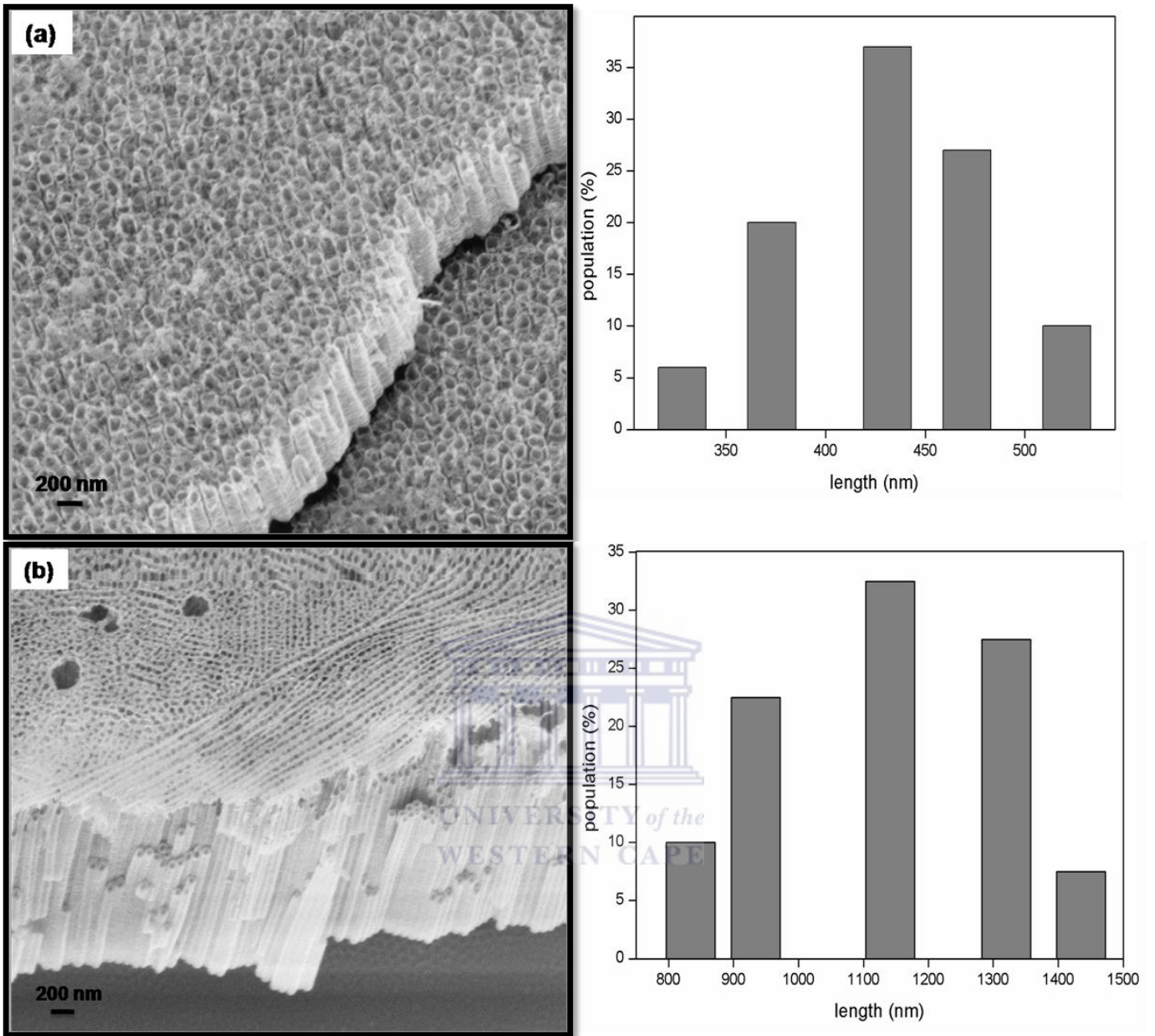
Figure 4.1: SEM micrographs and corresponding size-distributions of the nanotubes synthesised in electrolytic solutions consisting of (a) 0.15 M NH$_4$F + H$_3$PO$_4$ + H$_2$O and (b) 0.15 M NH$_4$F + 2M H$_2$O + ethylene glycol

The differences in nanotube morphology can be explained by examining the current-time transients of the respective films of tubes as shown in Figure 4.2. It is apparent that regular current oscillations occur during anodisation in

the aqueous solution. When converted to a length scale, these fluctuations in the current-time transients correspond well to the ridges in the nanotube wall; this effect has also been observed by other groups [4.1 – 4.3].
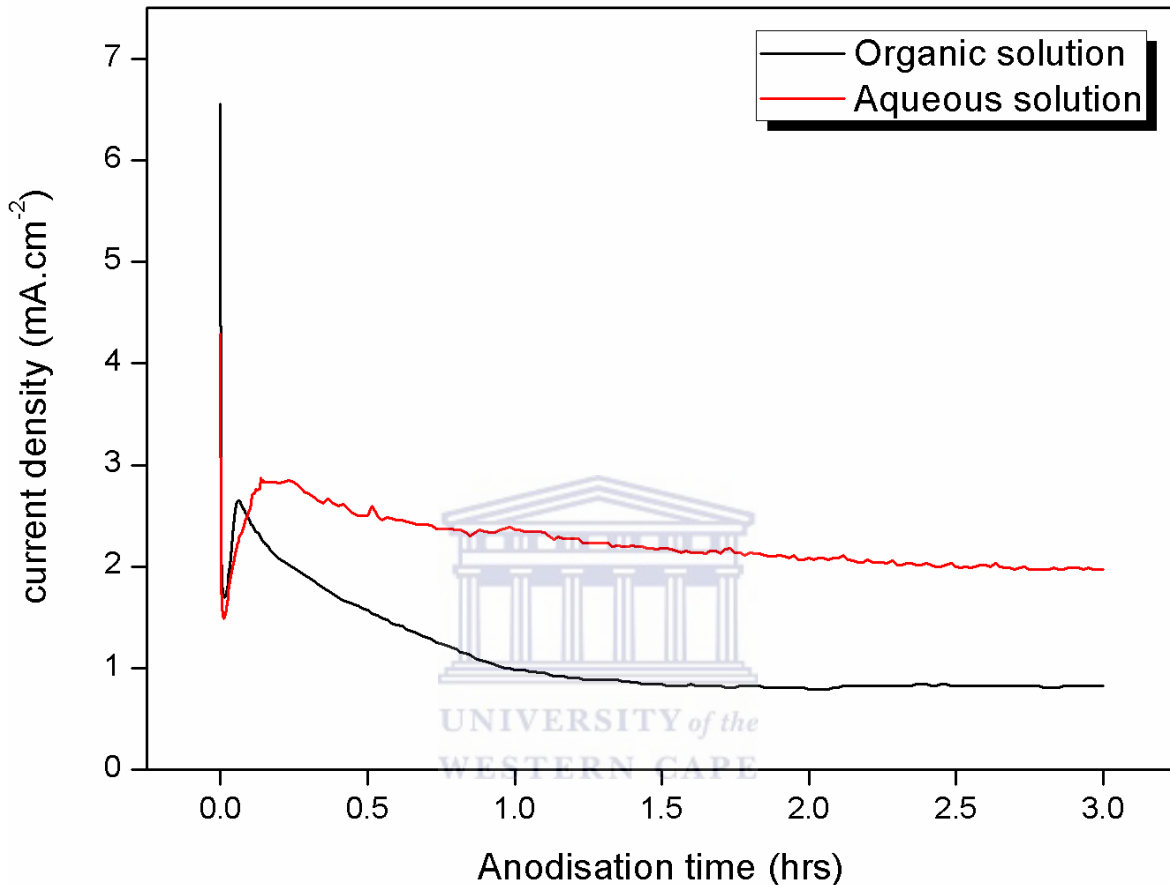
Figure 4.2: Current-density versus anodisation time curves for TiO$_2$ nanotubes synthesised in solutions A and B

The fluctuations in the red curve of Figure 4.2 can be explained by the fact that every current transient is accompanied by a pH burst at the nanopore tip [4.4]. This local acidification leads to temporary increased dissolution rate (discussed in Chapter 2.1.2) of TiO$_2$, which in turn, results in an irregular wall formation as witnessed in Figure 4.1 (a). Since diffusion is the main effect balancing local acidification, a key to suppress the pH bursts is to damp the

97

fluctuations by decreasing the diffusion constant in the electrolyte [4.4]. In this work this was achieved by using a highly viscous ethylene glycol electrolyte solution (i.e. solution B), which resulted in the synthesis of nanotubes with smoothed walls and longer lengths, as shown in Figure 4.1 (b).

As shown by the black curve of Figure 4.2 the current-time transient in solution B shows much lower current densities than that of the purely aqueous electrolyte. This is in line with a diffusion-controlled process, considering the Stokes–Einstein relation, where the diffusion constant, D, is proportional to $1/\eta$, where η is the solution viscosity [4.4]. Additionally as a result of the change in the diffusion coefficients and the improved confinement of the acidic area at the pore tip, the tubes grow now to lengths exceeding 1 μm.

The results of Figures 4.1 and 4.2 are very important for the application of the anodised TiO$_2$ nanotubes in the DSC. Anodisation in aqueous electrolytes in fluoride concentrations increased from 0.15 to 1 M and anodisation voltages between 5 and 30 V, did not yield nanotubes with lengths greater than 500 nm. In contrast, anodisation in ethylene glycol based electrolytes at voltages up to 60 V yielded TiO$_2$ nanotube films with lengths greater than 15 μm. It has been shown by various research groups that the optimum TiO$_2$ film thickness for application in DSCs is found between 10 and 15 μm [4.5]. For this reason the nanotubes were synthesised exclusively in ethylene glycol electrolytes.

4.1.2 Effect of Anodisation Voltage on the Morphology

No distinctive nanotubes could be observed after anodisation at operating voltages of 5 V and below, however the top-view micrographs of Figure 4.3 reveals well-defined porous structures after synthesis between 10 and 30 V. The cross-section of the nanotubes was viewed by bending the flexible anodised Ti foil in order to crack the intact film.

As shown in Figure 4.3 (f) the nanotubes have closed bottoms boasting a hexagonal structure. From the insets it can clearly be seen that the length of these self-organised structures linearly increase with applied voltage. At closer inspection, it was also found that the inner diameter as well as the thickness of the walls increase with increasing voltage.

Figure 4.4 (a) plots the relationships of the nanotube diameter and length as a function of the anodisation voltage. The black plot shows that the nanotube-voltage relationship can be modeled by a straight line with an intercept at approximately 20 nm. Between 5 and 30 V, Figure 4.4 shows that the diameter linearly increases from 35 nm at an applied potential of 5 V to 120 nm at 30 V. The slope of the fitted straight line is equal to two times the growth factor (f_g, discussed further in the chapter) of the anodic film, which represents the rate at which the nanotube diameter increases per applied voltage. From the equation of the black line in Figure 4.4 it was found that the diameter increased at approximately 2.3 nm/V.
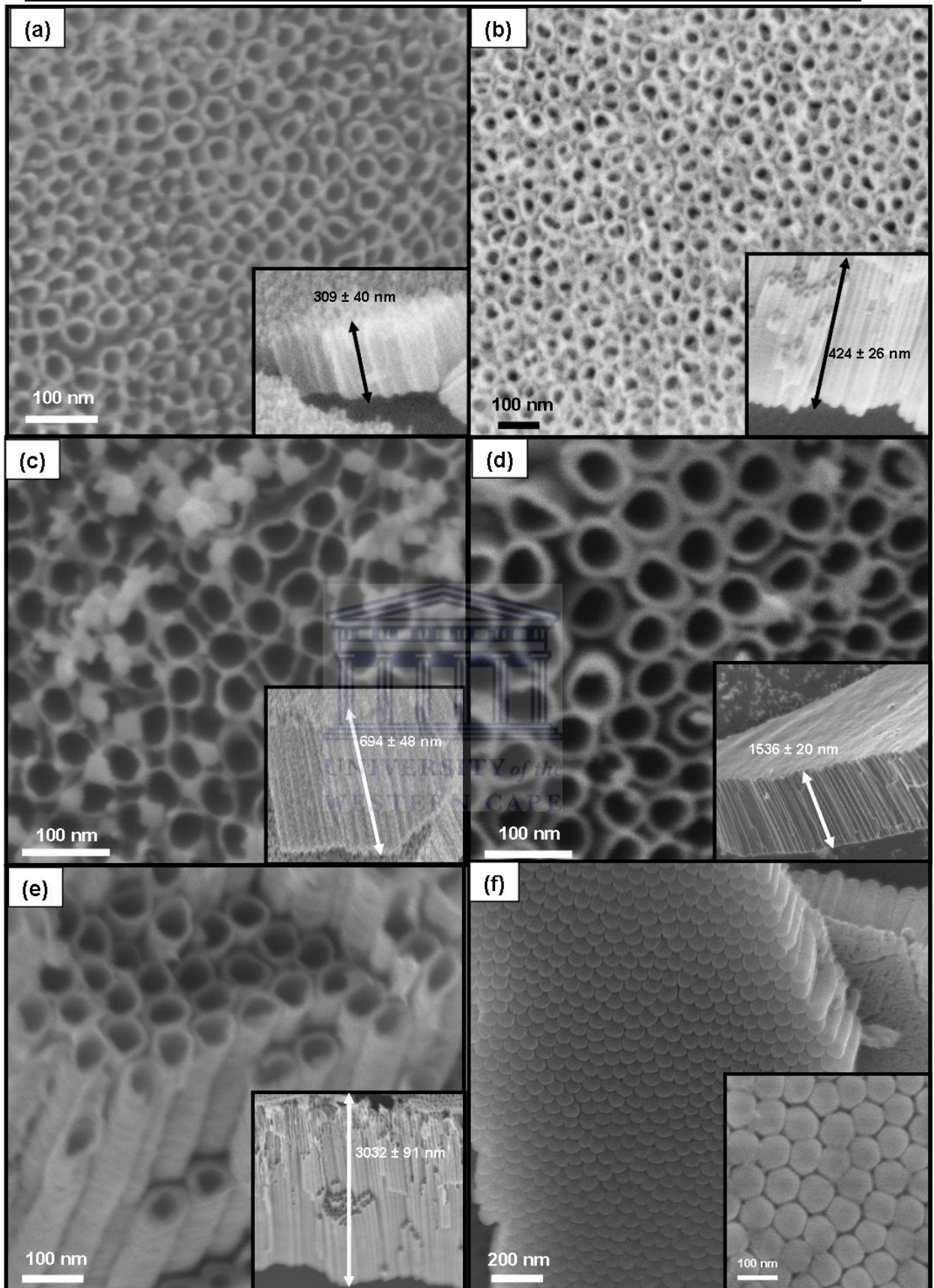
Figure 4.3: SEM micrographs of the Ti foils after anodisation for 3 hrs in an electrolyte solution consisting of 2 M H_2O + 0.3 M NH_4F + EG at (a) 10, (b) 15, (c) 20, (d) 25, (e) 30 V and (f) micrographs illustrating the hexagonally shaped nanotube bottom
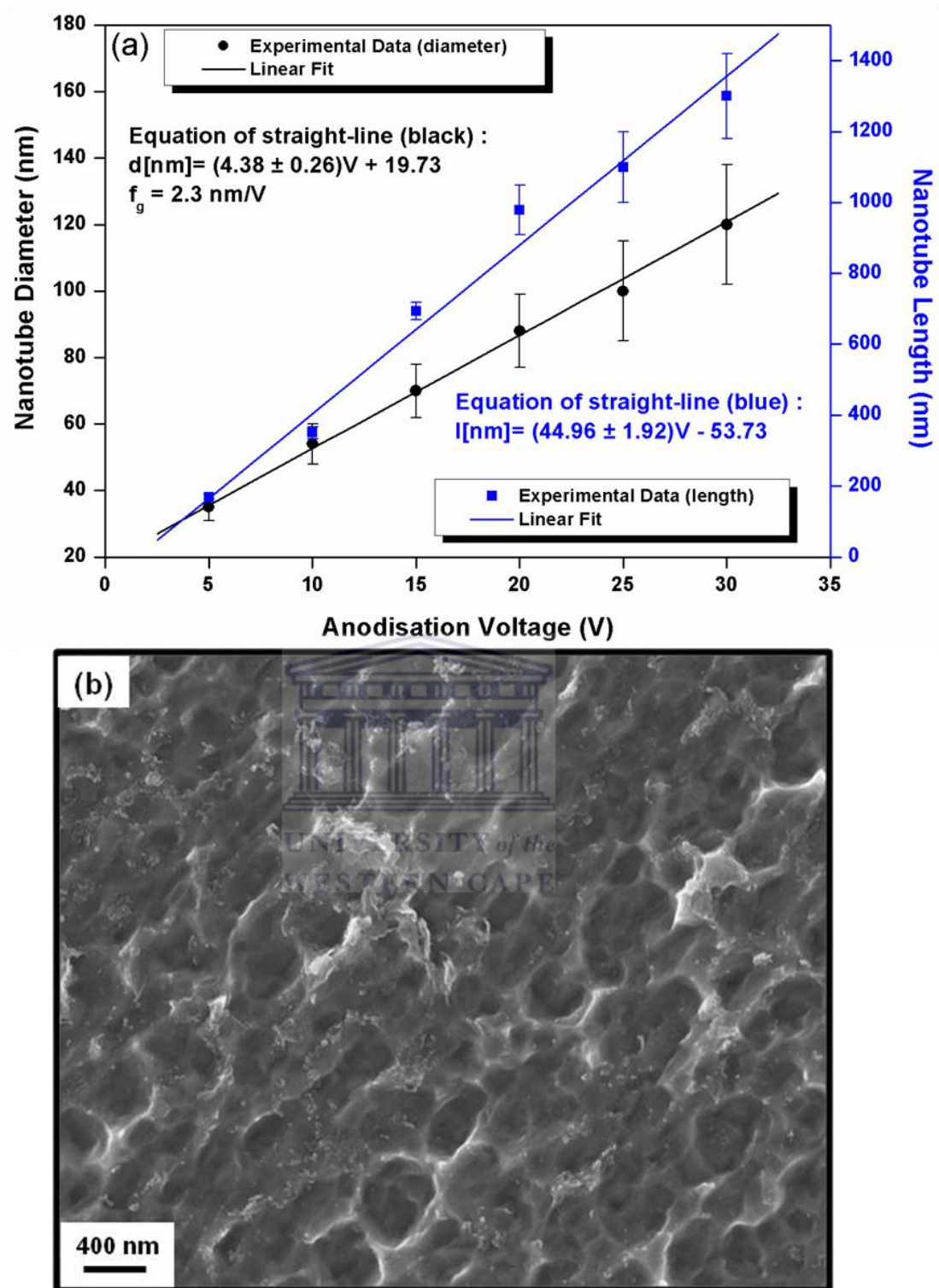
Figure 4.4: (a) Plot of the nanotube diameter and length versus the applied anodisation potential and (b) SEM micrograph of the Ti surface after anodisation at 3 V

Similarly the relationship between the nanotube length and the applied potential was modeled by a straight line (blue line in Figure 4.4) with an y-intercept at approximately -54 nm. This intercept makes sense because at applied voltages between 0 and 3 V no nanotube formation was observed, only a corroded Ti surface. This indicates oxide formation (as discussed in Chapter 2.1.2) during the initial stages of nanotube formation, but as a result of the limited driving force (i.e. potential) the F$^-$ interaction with the oxide layer was minimal and hence nominal pore and ultimately nanotube formation were observed. This is shown in Figure 4.4 (b). The slope of the blue line in Figure 4.4 (a) indicates that the nanotube length increases as a rate of approximately 45 nm per applied voltage.

Gong et al. [4.6] showed that anodisation in an aqueous electrolyte containing 0.5 wt% hydrofluoric acid (HF) at voltages increased from 3 to 20 V, results in the formation of tubular structures with pore diameters increasing from 15 to 30 nm. Bauer et al. [4.7] reported that anodisation in an electrolyte comprising of 1 M H$_3$PO$_4$ + 0.3 wt% HF at voltages between 1 and 25 V, yields nanotubes with diameters ranging between 15 and 120 nm. In a further report by Macak et al. [4.8] it was shown that anodisation of Ti foils in water/glycerol mixtures with 0.27 M NH$_4$F leads to an increased TiO$_2$ nanotube diameter, from 20 nm when operated at 2 V to 300 nm when anodised at 40 V.

From these studies it was found that the nanotube diameter, d, is related to the applied voltage, V by d (in nm) = k x V, where k = 2f$_g$; f$_g$ being the growth factor for anodic oxides and typically between 2 and 2.5 nm/V for TiO$_2$ films [4.9]. In Figure 4.4 (a) it is shown that the diameter of the nanotubes of Figure

4.3 linearly increases at a rate of about 2.3 nm per applied voltage, consistent with reported results. It is also shown that the nanotube length increases linearly at approximately 45 nm/V for the voltage range presented.

4.1.3 Effect of Anodisation Time on the Morphology

In order to explain the changes in the nanotube morphology, caused by an increase in anodisation voltage more accurately, a treatment of the formation of the nanotubes during the anodisation process is required. Figure 4.5 depicts the current density as a function of time for the Ti foil sheets anodised at the increasing operating voltages for three hours in the 2 M H$_2$O + 0.3 M NH$_4$F + EG solution. It can be seen that an increase in the anodisation voltage yields an increase in the current density and that four different parts of the curve can be identified, suggesting four different stages of growth.

A rapid decrease in the current density was observed during the initial stage of anodisation (~ 80 s), which is ascribed to the formation of a thick oxide layer between the Ti and electrolyte solution, thereby inducing a large IR drop across the electrode [4.8]. In addition, the IR drop increased with an increase in the applied voltage, suggesting an increase in the thickness of the insulating oxide layer. The SEM micrograph and EDS spectrum of Figure 4.6 (a) confirms the above by revealing areas in the Ti substrate incorporating O$^-$ ions for oxide formation after 80 seconds of anodisation.
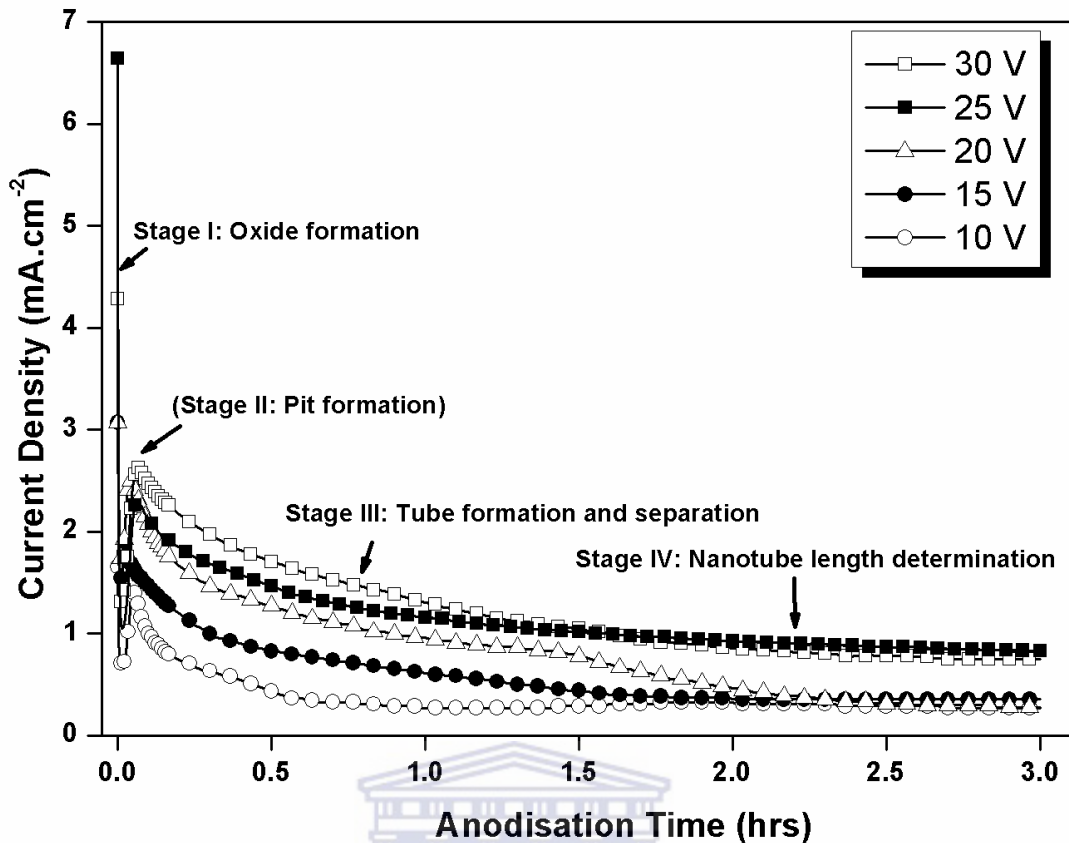
Figure 4.5: Current density vs. time curves of the Ti foil sheets anodised at the different voltages

During stage II, a steep increase in the current density profile was observed for roughly 5 minutes after the initial IR drop and is attributed to the rapid chemical dissolution of the oxide barrier by the F$^-$ ions from the electrolyte. This process results in the formation of pits (or pores) on the substrate surface as shown in Figure 4.6 (b) and form the activation sites for tube formation as shown by the micrograph of Figure 4.6 (c) and the gradual decrease in the current density curve after anodisation of about 30 minutes (stage III). The final stage determines the length of the nanotubes, with greater applied voltages yielding free-standing nanotubes of longer length, as was shown by the SEM micrographs of Figure 4.3.

As shown in Figures 4.3 and 4.4 as well as the results from the literature stated, the voltage induces increases in the nanotube length, wall thickness and diameter. However the exact mechanism describing these increases remains a topic of debate, with the most comprehensive discussion to date found in [4.10, 4.11].
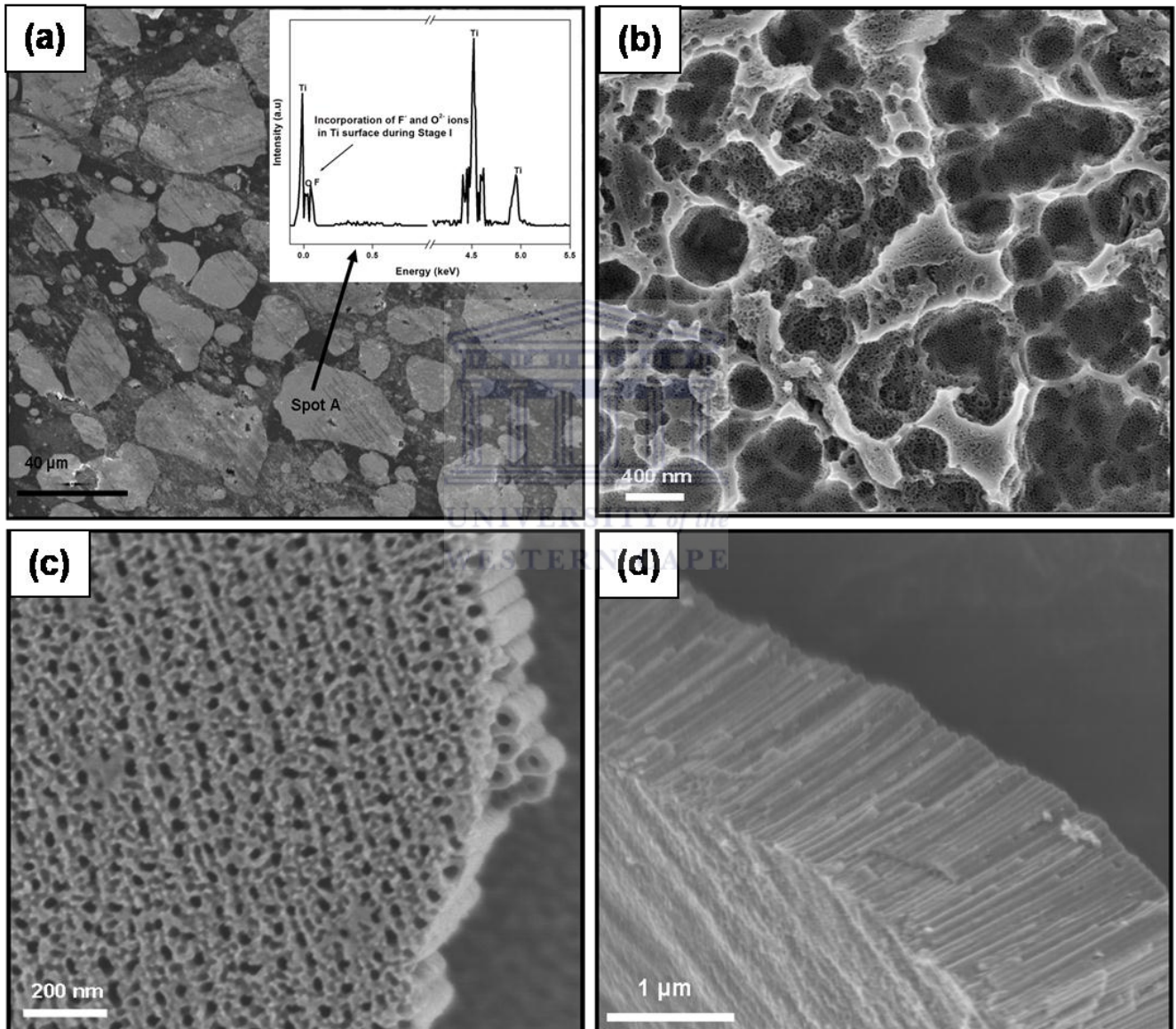
Figure 4.6: SEM micrographs of the Ti foil anodised for (a) 80 seconds along with the corresponding EDS spectrum, (b) 6 minutes, (c) 30 minutes and (d) 2 hours

4.1.4 Effect of F⁻ Concentration on the Morphology

Figure 4.7 shows SEM micrographs of the Ti foil anodised at 30 V for 3 hours at NH$_4$F concentrations increased from 0.15 M up to 1M. As shown, the average nanotube diameter at 0.15 M NH$_4$F is 20 nm and increases to 100 nm at 0.6 M NH$_4$F. At a NH$_4$F concentration of 1 mol/l the nanotube architecture breaks down, as shown in Figure 4.7 (d). The average nanotube length was 3 µm, as was the case in Figure 4.3 (e).

The current density – time curves for the nanotubes synthesised at increasing F⁻ ion concentrations are plotted in Figure 4.8. The regions of interest in Figure 4.8 occur at anodisation of roughly 5 minutes, during stage II of the growth process or, in other words, during pore formation. At the same operating voltage Figure 4.8 shows that the current density peak position shifts to longer anodisation time as the F⁻ concentration is increased. In addition, Figure 4.8 also shows that this shift is accompanied by an increase in the current density. These two striking features of Figure 4.8 explains the nanotube morphology presented in Figure 4.7.

The current density shift with increasing fluoride ion concentration suggests a greater chemical dissolution rate (reaction 2.4 of Chapter 2) of the compact oxide layer during stage I of the nanotube growth (see Chapter 2.1.2). This is to be expected seeing that more F⁻ ions interact with the compact oxide layer thereby increasing the surface activation sites, which ultimately lead to pore formation. However, pore formation is random and with the large number of F⁻ ions interacting with the activated surface, larger diameter pores may well be observed as a result of the closely located activation sites.
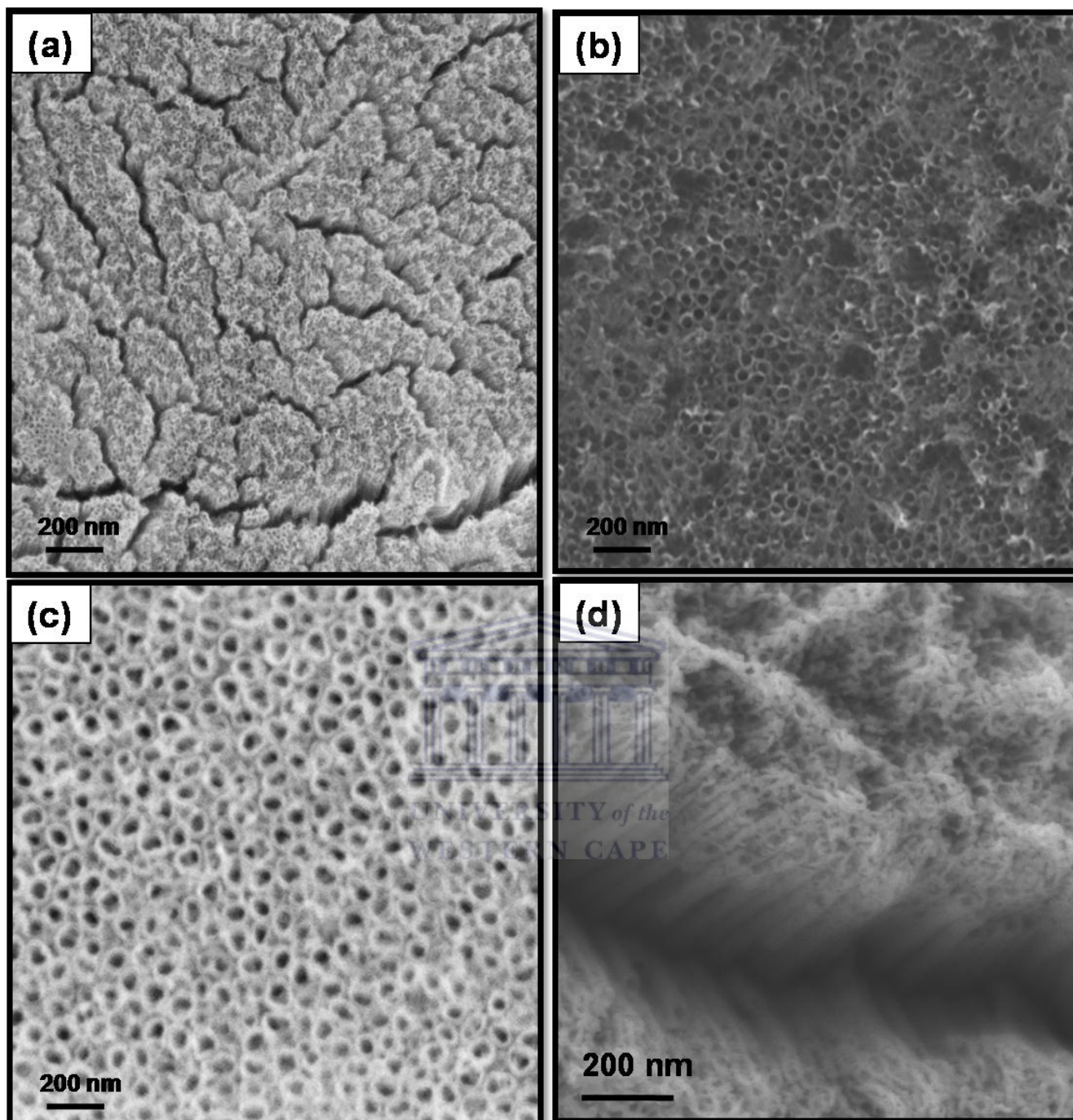
Figure 4.7: SEM micrographs of TiO$_2$ nanotubes synthesised with a NH$_4$F concentration of (a) 0.15, (b) 0.3 (c) 0.6 and (d) 1 M

This theory is further supported by the increased current density observed with an increase in the F$^-$ ion concentration. As a result of the greater pore

formation the active area of the oxide layer increases and thus the current increases [3.12]. With time, these individual pores start interfering with each other and start competing for the available current, which leads to tree-like growth of the oxide layer and formation of the nanotube structure. As Figure 4.7 suggests, at a NH₄F concentration of 1 M, the compact oxide layer is depleted at such high F⁻ ion concentrations and leads to a breakdown of the nanotube morphology.
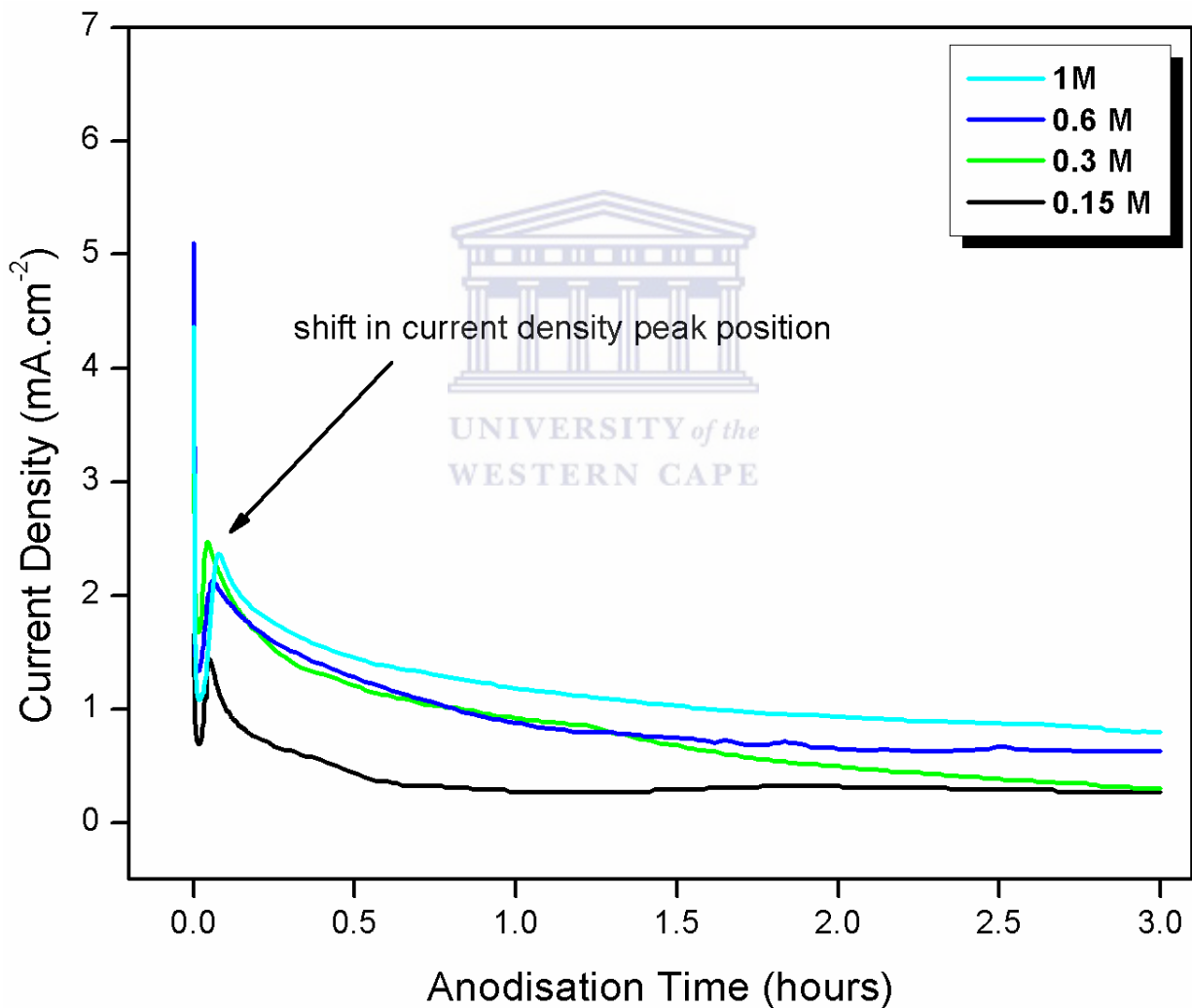
Figure 4.8: Current density vs. anodisation time curves of the nanotubes synthesised at 0.15, 0.3. 0.6 and 1 M NH₄F at 30 V for 3 hours

Based on the findings of sections 4.1.1 and 4.1.2 of this chapter, the optimum anodisation conditions for the synthesis of TiO$_2$ nanotubes arrays with an average length of 15 µm, outer diameter of 50 nm, and wall thickness of approximately 20 nm were found to be an anodisation voltage of 60 V, neutral organic electrolyte consisting of 2 M H$_2$O + 0.15 M NH$_4$F + EG and an anodisation time of 6 hours. Figure 4.9 shows a FIB-SEM micrograph of a sample synthesised at these optimised parameters. The ion-milled section was prepared as explained in Chapter 3.1.1.
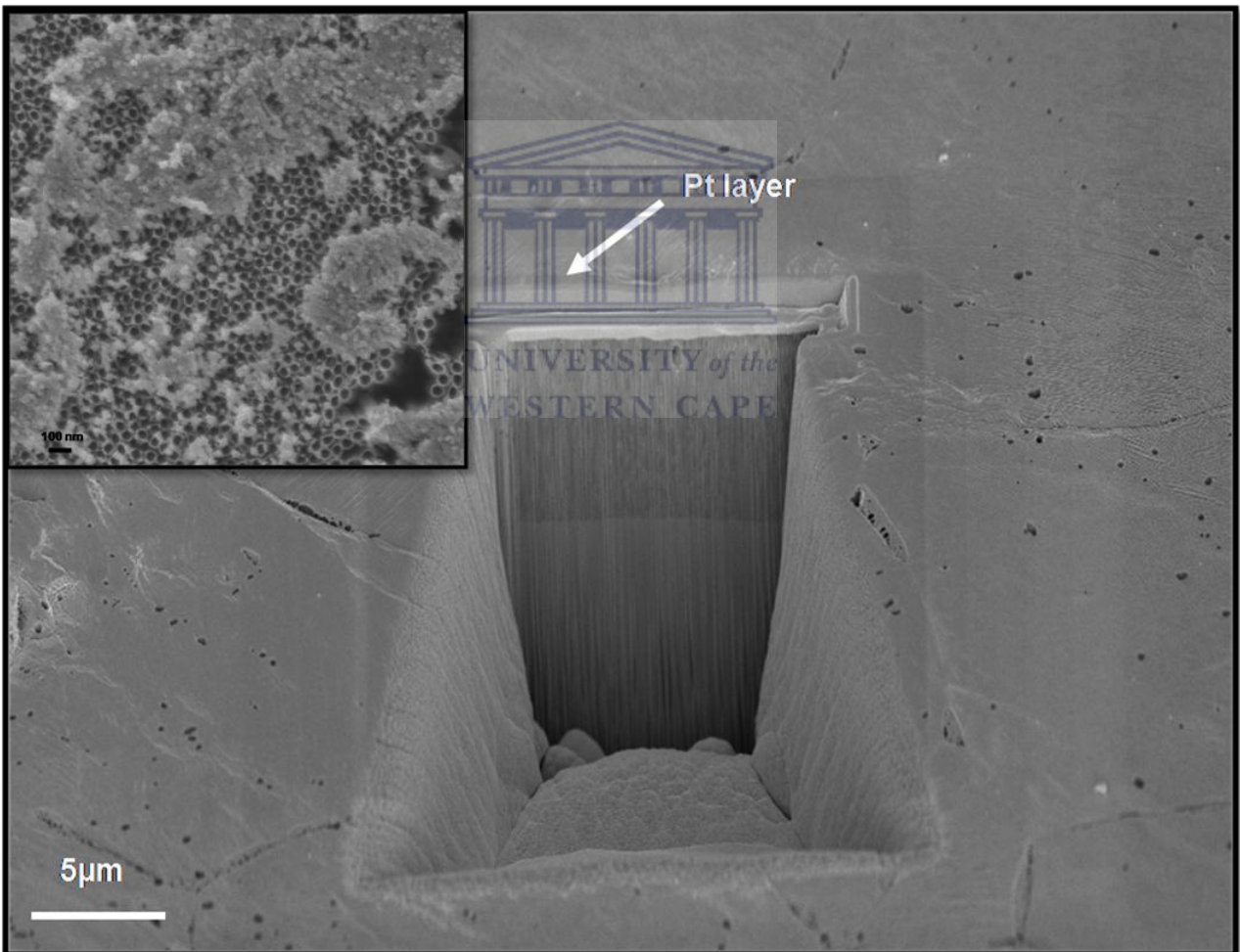
Figure 4.9: FIB-SEM micrograph of the Ti foil anodised at the optimum anodisation parameters

As shown in the micrograph, the Ti sheet is completely consumed after anodisation at the above bath conditions, with a TiO$_2$ nanotube layer in excess of 15 μm obtained. The inset in Figure 4.9 is a SEM micrograph of the top-view of the anodised sample. From this micrograph an average nanotube diameter of approximately 50 nm and wall thickness of 15 nm were obtained.

4.2 Crystallinity

Figure 4.10 shows the x-ray diffraction (XRD) patterns of the nanotubes annealed at 450 ⁰C for 2 hours in air, at atmospheric pressure. For comparison the XRD patterns of a nanotube sample without annealing and that of the commercially pure Ti substrate (before anodisation) are also included. It can be seen that the as-synthesised nanotubes are amorphous with only diffraction peaks of the Ti substrate visible. However, the annealed tubes show very interesting diffraction patterns. Closer examination reveals that they crystallise predominantly in the anatase TiO$_2$ phase. Furthermore, with an increase in operating voltage the anatase diffraction peak at 2θ ~ 25⁰ gradually increases, while the rutile peak at 2θ ~ 44⁰ decreases.

Mor et al. [4.13] showed that the rutile and anatase phases co-exist at temperatures between 430 ⁰C and 620 ⁰C for nanotubes synthesised on top of a Ti layer. However, no rutile diffraction peaks were detected when the nanotubes were synthesised on top of a glass substrate and annealed at 500 ⁰C. This showed that the rutile crystallites grow at the interface between the nanotube bottom and the thermally oxidised Ti substrate. It is also reported that the nanotube wall thickness limits crystal growth as a result of the limited area

available for nucleation site formation [4.13, 4.14]. In Figure 4.3 it was shown that the nanotube wall thickness gradually increases with an increase in applied voltage, hence the area available for nucleation formation also increased, according to the findings in [4.13]. Applying the Scherrer formulation (see Chapter 3.1.4.2) to the XRD diffractograms it was found that the grain size of the anatase crystallites indeed increased with an increase in the nanotube wall thickness (caused by an increase in voltage), while the rutile grains decreased. Figure 4.11 illustrates this phenomenon by plotting the relationships between the anatase and rutile crystallite sizes and the applied anodisation voltage. Based on these findings the evolution of the crystallinity of the nanotubes upon annealing, as presented by the XRD patterns in Figure 4.10, can be explained as follows:

The increase in the applied voltage induces an increase in the nanotube wall thickness, thereby presenting a greater area available for the formation of nucleation sites. Subsequently, anatase crystallites of greater size form upon annealing at 450 °C, as shown in Figure 4.11. An increase in the anodisation voltage also results in increased rates of breakdown of the oxide layer formed during the initial stages of anodisation [4.13], thereby reducing the area available for rutile crystallite formation at the tube bottom and hence the decrease in the rutile phase of Figure 4.10.
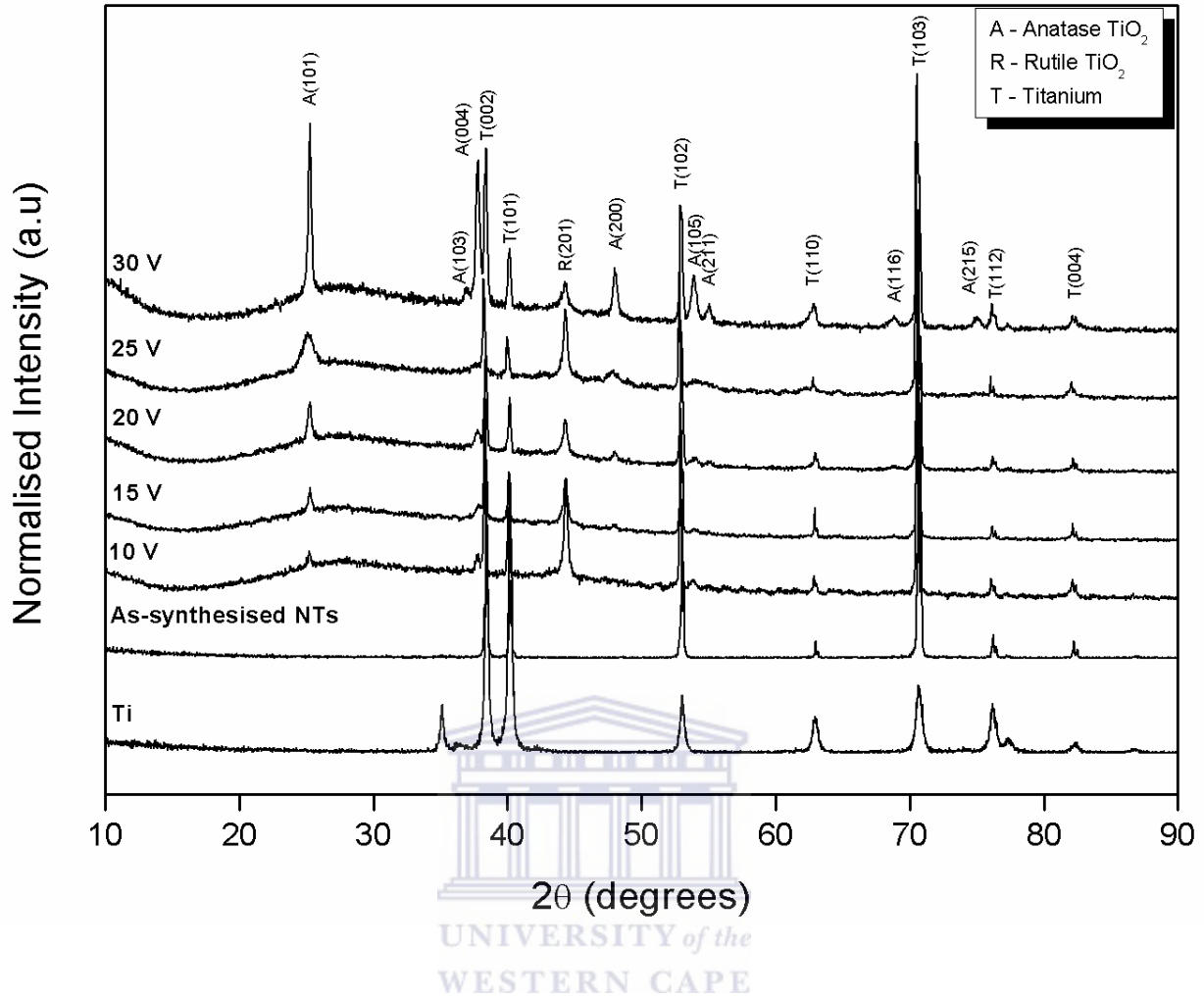
Figure 4.10: XRD patterns of the anodised TiO$_2$ nanotube films annealed at 450 °C for 2 hours in air at atmospheric pressure. For comparison, the XRD patterns of the Ti substrate and an as-synthesised Ti sheet is also included

Previous studies [4.15 – 4.18] have shown that this phase formation/transition is mainly possible upon annealing at different temperatures. However in this study it is shown that the crystallinity is directly dependent on the nanotube structure, in particular the nanotube wall thickness and the oxide layer constituting the nanotube bottom, which were controlled by the applied voltage during the anodisation process.

112
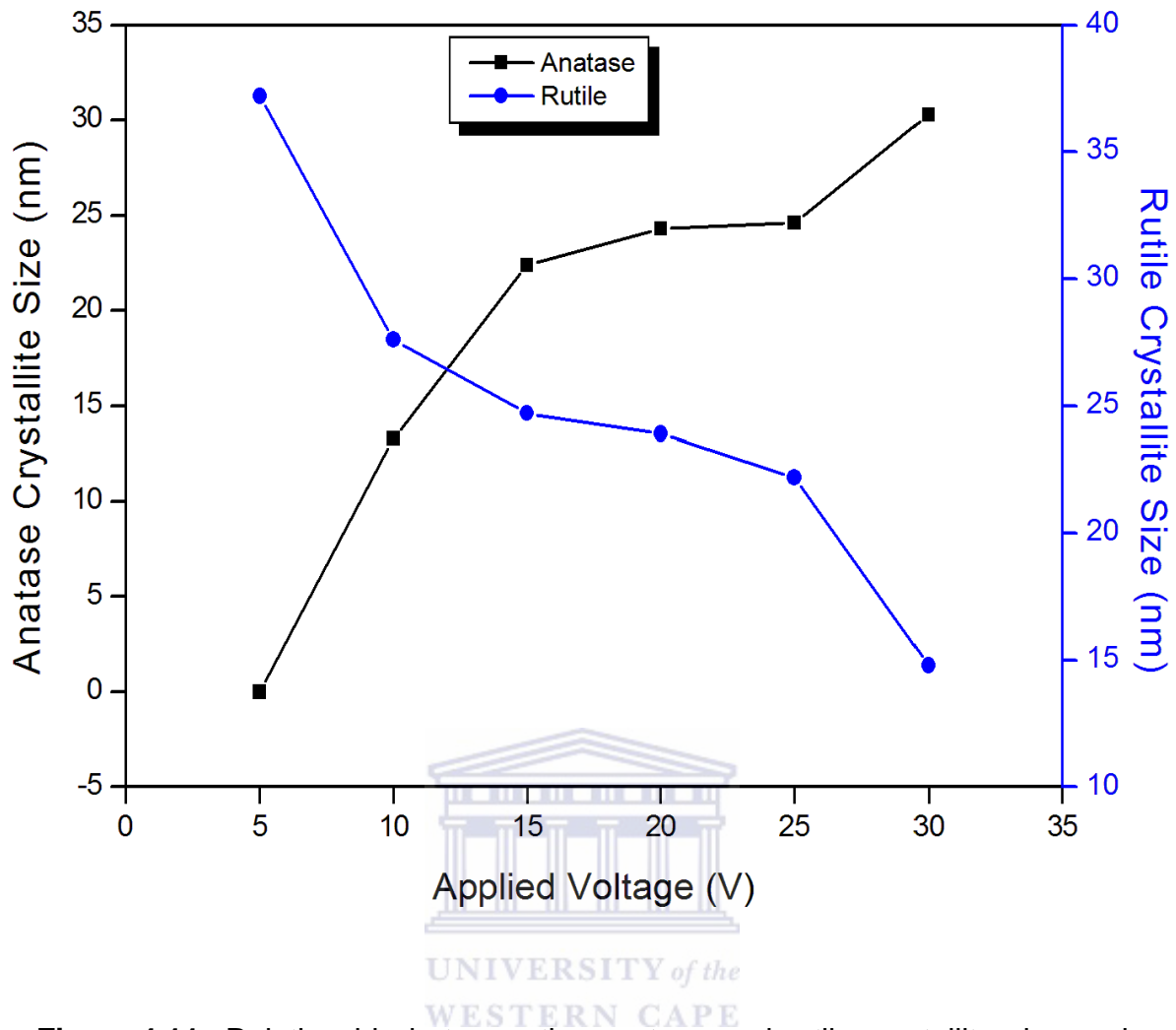
Figure 4.11: Relationship between the anatase and rutile crystallite size and the applied anodisation voltage

4.3 Optical Characterisation of the TiO$_2$ Nanotube Films

It is known that the crystallinity affects the optical properties of materials. Hence it is expected that the changes in the crystallinity, as observed in Figure 4.10, should have an influence on the measured optical spectra of the nanotubes. In this regard photoluminescence (PL) spectroscopy has proved to be an important technique in the characterisation of the optical energy bands of materials and the study of surface states, donor/acceptor states and structure-

induced trapping states present within the band gap of materials. It is also well known that PL spectra are greatly affected by changes in size of nanomaterials [4.19 – 4.22].

Figure 4.12 shows the PL spectra, recorded with an excitation wavelength of 325 nm at room temperature of the nanotubes synthesised at operating voltages of 10, 20 and 30 V, as well as the PL spectrum of P25 Degussa nanoparticles, as a comparison. A broad, asymmetric PL band, tailing towards low photon energies and peaking at approximately 380 nm, can be observed. Each of the spectra was fitted with Lorentzian functions, which revealed the presence of four PL bands. It can be seen that the Lorentzian line-shapes are a very good fit for the experimental data acquired, with a standard deviation of less than 5% obtained for all spectra. Table 4.1 captures the band energies obtained from peaks 1 to 4 of Figure 4.12.

TiO$_2$ is an indirect bandgap material and the emission peaks located around 3.53 eV (peak 1) and 3.29 eV (peak 2) for the tubes synthesised between 10 and 30 V, are attributed to the highest energy direct transition $X_1 \rightarrow X_2/X_1$ and the lowest energy indirect transition $\Gamma_1 \rightarrow X_2/X_1$ within the Brillouin zone, respectively [4.23]. TiO$_2$ is also known to be strongly ionic and as such its valence band comprises mainly of the outermost p-electrons of oxygen, whereas the bottom of the conduction band is filled with Ti 3d orbitals [4.24]. Thus for TiO$_2$ nano-crystals with enhanced surface-to-volume ratios, substantial numbers of Ti atoms are exposed at the surface region and transformed into Ti^{3+}, Ti^{2+} and Ti$^+$. Subsequently, these Ti-O dangled bonds present distorted TiO$_6$ octahedra and introduce localised energy states within the bandgap of the

material. These so-called surface states then become luminescent centers upon radiation.
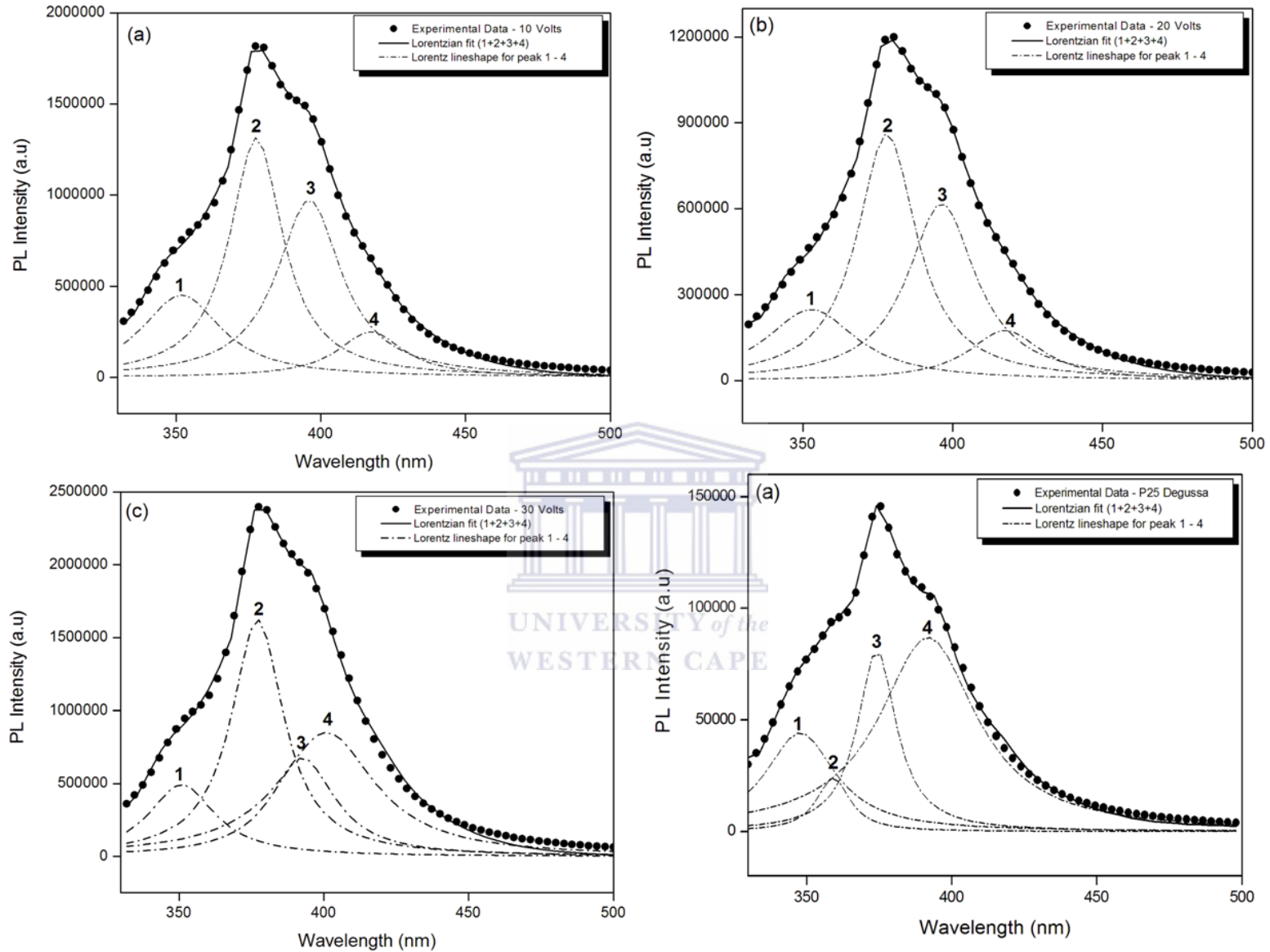
Figure 4.12: Room temperature PL spectra of the nanotubes synthesised at (a) 10 V (b) 20 V, (c) 30 V and (d) P25 Degussa

Table 4.1: PL energies and intensities as a function of the applied anodisation voltage

Peak no.	Origin	Reference	Experimental Data							
			10 V		20 V		30 V		P25 Degussa	
			Peak position (eV)	PL x 10^4 (a.u)	Peak position (eV)	PL x 10^4 (a.u)	Peak position (eV)	PL x 10^4 (a.u)	Peak position (eV)	PL x 10^4 (a.u)
1	Indirect transition	3.59 eV [3.24]	3.541	49.5	3.532	30.8	3.527	25.1	3.573	4.43
2	Direct transition	Anatase bandgap [4.24]	3.296	163	3.289	87.1	3.292	94.3	3.461	2.43
3	Shallow traps	0 – 1 eV below anatase bandgap [4.28, 4.29]	3.166	67.5	3.137	60.9	3.141	74	3.321	8.14
4	Shallow traps	0 – 1 eV below anatase bandgap [4.28, 4.29]	3.101	85.1	2.979	17.8	2.978	19.1	3.172	8.69

The luminescent centres are reportedly found at energy levels between 0 and 1 eV below the conduction band of anatase TiO$_2$ [4.25, 4.26]. Hence peaks 3 and 4 in Table 4.1 are ascribed to luminescence from these surface states that are present on the distorted TiO$_6$ octahedra. The XRD results of Figure 4.10 showed the presence of small traces of rutile in the nanotube samples therefore some uncertainty might arise in the assignment of this peak. However, it is reported [4.27] that the presence of rutile phases in nano-crystals significantly reduces the PL intensity due to its poorer photo-reactivity compared to anatase. Table 4.1 reveals no notable reduction in the PL intensity of peak 3 with an increase in the operating voltage, hence the assignment of this peak to shallow surface state traps. In addition, when compared to the PL

spectrum of the P25 Degussa, which contains a notable amount of rutile crystallites (~ 15% as obtained from the manufacturer specifications), it can be seen that the nanotubes with the predominant anatase crystallinity possess a PL intensity one order in magnitude greater, which further supports the above argument.

4.4 Quantum Confinement in the TiO$_2$ Nanotube Films

Red shift of the direct (peak 4) and indirect transitions (peak 3) of Figure 4.12 (a) to (c) is observed for the TiO$_2$ nanotubes, implying a decrease in the bandgap of the nanotube films. This fits well with the increase in the anatase crystallite size resulting from the increase in the anodisation voltage, shown in Figure 4.11, and provides evidence of quantum confinement within the TiO$_2$ nanotubes. For a detailed investigation of these effects, Raman spectroscopy was employed. This technique has proved to be an important tool not only for phase identification, but also for assessment of nano-scale structural changes when studying subtle spectral variations [4.19]. Moreover, Raman spectroscopy has been extensively used to study size-related confinement of optical phonons (known as the phonon confinement, PC, model) within TiO$_2$ nano-crystalline thin films [4.18. 4.29] and various TiO$_2$ nano-structures [4.15 – 4.17, 4.30, 4.31]. However, vigorous treatment of the problem pertaining to anodised TiO$_2$ nanotube arrays remains minimal.

Anatase TiO$_2$ belongs to the D$_{4h}$ (I4$_1$/amd) space-group and has six Raman active modes (A$_{1g}$, 2B$_{1g}$ and 3E$_g$) at wavenumbers of 142 cm^{-1} (E$_g$), 197 cm^{-1} (E$_g$), 399 cm^{-1} (B$_{1g}$), 513 cm^{-1} (A$_{1g}$), 519 cm^{-1} (B$_{1g}$) and 639 cm^{-1} (E$_g$).

Rutile, on the other hand, has a space group D$_{4h}$ (P4$_2$/mnm) giving rise to four Raman active modes (A$_{1g}$, B$_{1g}$, B$_{2g}$, and E$_g$) at Raman shifts of 143 cm^{-1}, 447 cm^{-1}, 612 cm^{-1} and 826 cm^{-1}, respectively [4.18, 4.30]. Figure 4.13 plots the Raman spectra of the TiO$_2$ nanotubes that were calibrated with a crystalline silicon <100> standard at 521 cm^{-1}. The results confirm that annealing at 450 ºC for 2 hours crystallises the amorphous nanotubes into anatase TiO$_2$, in coherence with the XRD results presented in Figure 4.10. However, no Raman active phonon modes originating from the rutile crystal structure, as previously indicated by the XRD data, were observed. This is attributed to the difference in the detection limit of the two underlying characterisation techniques. For comparison, the Raman spectrum of commercial Degussa P25 nanoparticles with negligible rutile content and a mean diameter of 30 nm is also included.

The PC model [4.32] predicts that a decrease in size of a nano-crystal results in a blue shift of the fundamental Raman active phonon mode, located around 142 cm^{-1} for TiO$_2$. In addition, it is reported [4.15] that these nano-crystals also stimulate an asymmetric broadening of the 142 cm^{-1} mode towards higher wavenumbers.
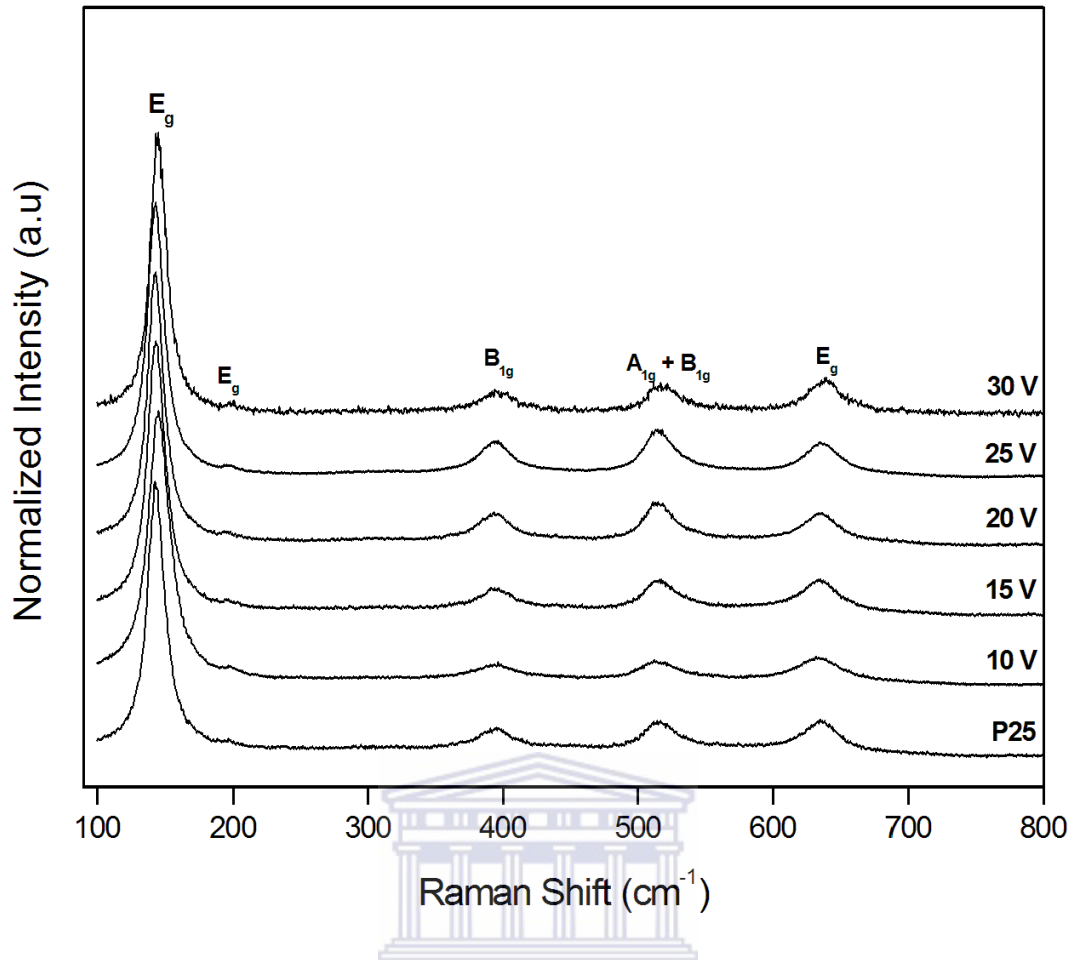
Figure 4.13: Raman spectra of the TiO$_2$ nanotubes annealed at 450 °C for 2 hours in air at atmospheric pressure and for comparison the Raman spectrum of P25 Degussa with minimal rutile content

Theoretically for low-dimensional systems the Raman line-shape is given by [4.32, 4.33]

$$I(\omega) \propto \int \frac{\left|c(\vec{q})\right|^2}{\left(\omega(\vec{q}) - \omega_0\right)^2 + \left(\dfrac{\Gamma_0}{2}\right)^2} \, d^3q \qquad (4.1)$$

where Γ_0 is the full-width at half-maximum (FWHM) of the Raman line at room temperature and $\omega(\vec{q})$ is the phonon dispersion curve. The TEM images of Figure 4.14 show that the nanotubes indeed consist of small crystallites, arranged to form the wall of the nanotube, as deduced by the XRD results in

119

section 4.2 above. As shown these crystallites are spherical, thus the function $c(\vec{q})$ of equation (4.1) may be written as [4.34]

$$\left|c(\vec{q})\right|^2 = \frac{L^6}{16(2\pi)^2\alpha^3}\exp\left(-\frac{q^2L^2}{2\alpha}\right)$$

(4.2)

where L is the crystallite size, q is the wave vector and α is a constant. Balaji et al. [4.18] used values of $\alpha = 8\pi^2$, $\Gamma_0 = 7.5$ cm^{-1} and $\omega_0 = 142.5$ cm^{-1} in their studies on PC in nano-crystalline anatase TiO$_2$ thin films.
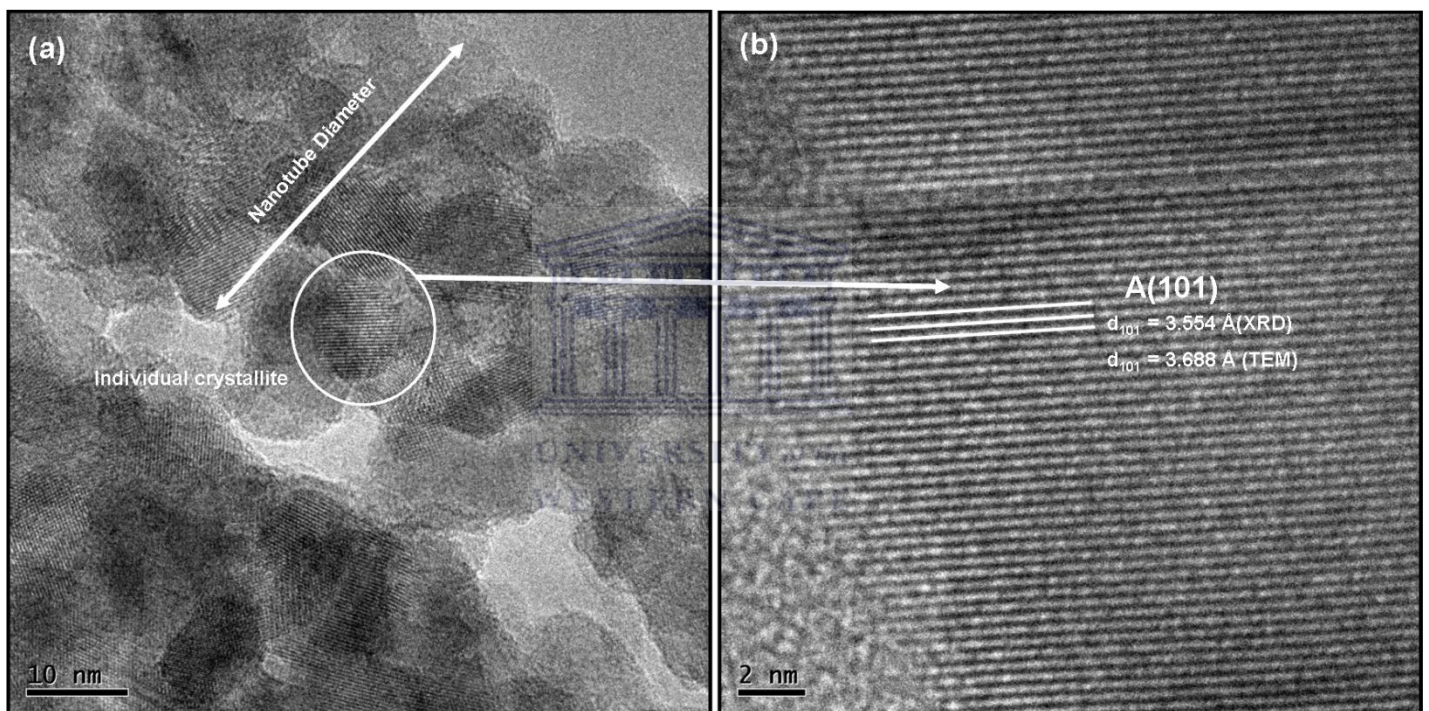
Figure 4.14: (a) TEM micrograph of a nanotube sample illustrating how the crystallites constitute the walls of the structure and (b) high-resolution micrograph showing the interplanar spacing of the anatase (101) planes. The distance obtained from the TEM micrographs is in good agreement with the d-spacing results calculated from the XRD spectra.

In order to evaluate the effect of the TiO$_2$ crystallite size on the amount of dispersion and ultimately the confinement of the phonon modes in the material, the Balaji group employed a modified version of the weighted average of phonon dispersions proposed by Ivanda et al. [4.35], given as

$$\omega(\vec{q}) = \omega_0 + \Delta \sin^2(\frac{q\pi}{x})$$

with ω_0 = 142.5 cm^{-1}, Δ = 164 cm^{-1} and x = 1.51779 was employed. The values of Δ and x determine the amount of dispersion in $\omega(\vec{q})$.

Figure 4.15 plots the shift in peak position of the 142 cm^{-1} Raman mode (ω_0) as well as the change in its FWHM (Γ) as a function of the XRD crystallite size, obtained from Figure 4.11. It can be seen that the increased particle size produces a smaller shift in peak position along with a decrease in the FWHM. Fitting of the data with the model proposed by Balaji et al. [4.18] shows that the anodised TiO$_2$ nanotube structures conform to the predictions of the PC model (equation 4.2). Thus the red shift of peak 4 in the PL spectra of Figure 4.12 can be ascribed to confinement of the optical phonon modes, subsequently yielding a larger bandgap with the decrease in crystallite size.

As can be seen the model of Balaji predicts the trends in the dispersion at low crystallite sizes between 10 nm to 20 nm fairly accurately. Conversely, at greater crystallite sizes the model varies beyond the error in the experimental dispersion data, as shown by the solid lines of Figure 4.14. This is to be expected, seeing that the model is based on the fact that confinement effects are most visible for small crystallites, usually less than 10 nm. Furthermore, in the studies presented by Ivanda, Bersani and Balaji, the TiO$_2$ nano-crystallites are present in thin films. In the case of anodised TiO$_2$ nanotubes these

crystallites are restrained to the curved walls of the nanotubes as was shown by the TEM micrographs of Figure 4.14. The data of Figure 4.11 showed that the crystallite sizes are comparable to the walls of the nanotubes, and is even considered to be dependent on these wall thicknesses. These factors are not considered in the above models and thus further theoretical work is required on these relatively new nanostructured TiO$_2$ to fully describe the dispersion and phonon confinement within the nanotubes.
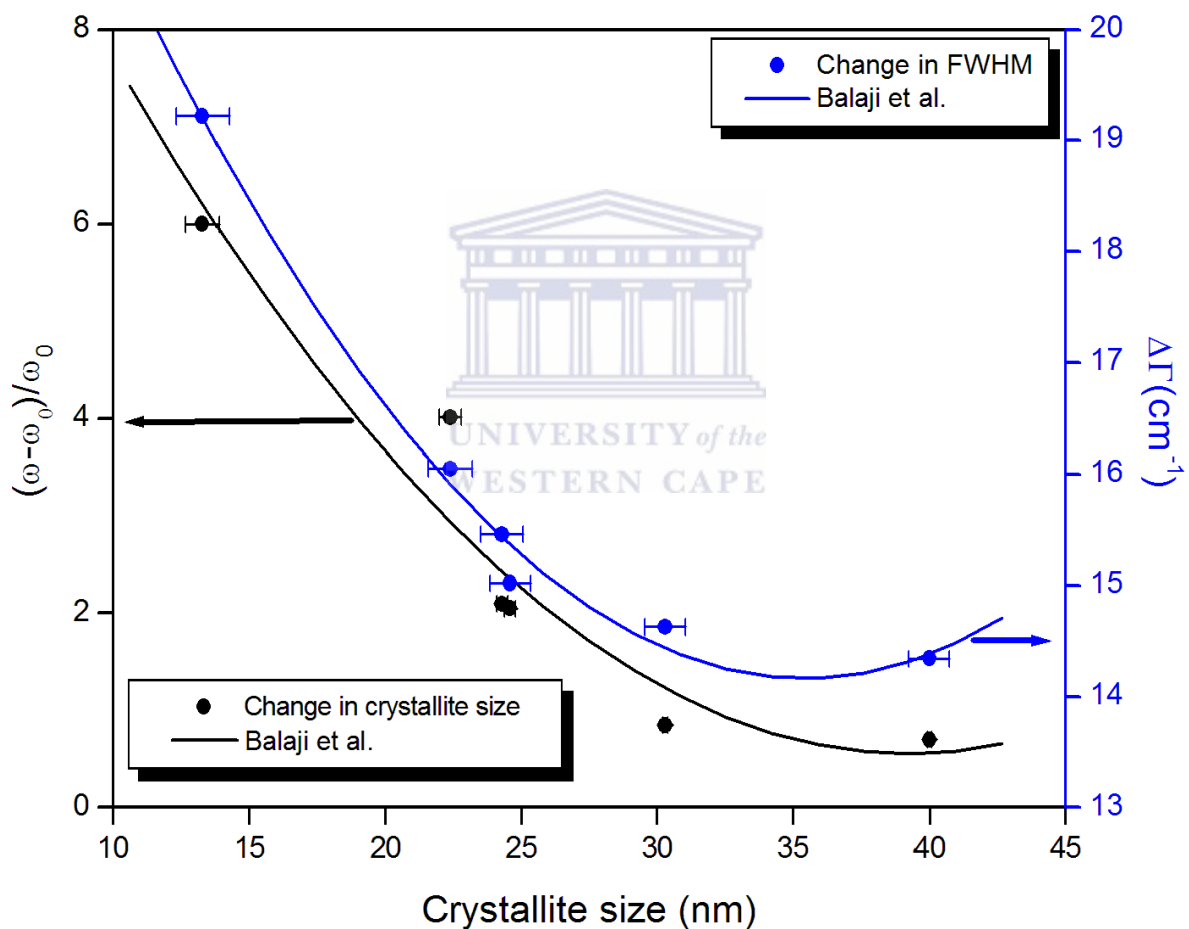
Figure 4.15: Calculated peak shift and FWHM of the 142 cm^{-1} Raman active mode of the anatase TiO$_2$ nanotubes as a function of the crystallite size. The solid lines fit the model proposed by Balaji et al. [4.18] to the experimental data

Conclusion

In this Chapter the anodisation bath conditions were optimised to synthesise TiO$_2$ nanotube arrays with an average length of 15 µm, diameter of 50 nm and wall thickness of 15 nm. Nanotubes of these dimensions were managed to be synthesised at an anodisation voltage of 60 V, neutral organic electrolyte consisting of 2 M H$_2$O + 0.15 M NH$_4$F + EG and an anodisation time of 6 hours. The anodisation voltage was increased from 5 to 60 V and it was found that the nanotube diameter, wall thickness and length linearly increased with an increase in voltage. The F- ion concentration was varied from 0.15 to 1 mol/l by increasing the concentration of NH$_4$F in the electrolyte bath. This resulted in an increase in the nanotube diameter.

The as-anodised nanotubes were found to be amorphous and as such annealed at 450 °C for 2 hours in air at atmospheric pressure. This yielded crystalline anatase TiO$_2$ nanotubes and it was found that the crystallinity of the nanotubes are dependent on physical structure of the nanotubes, in particular the nanotube wall thickness and hexagonally shaped bottom.

It was also found that the optical properties, especially the bandgap of the TiO$_2$ nanotubes are dependent the crystallinity, which in turn was dependent on the structural characteristics, such as the wall thickness, diameter and length. PL measurements, supplemented by Raman spectra revealed increased quantum confinement of the optical phonon modes of the nanotubes synthesized at low anodisation voltages, consequently yielding a larger bandgap.

References

[4.1]   R. Beranek, H. Hildebrand, P. Schmuki, Electrochem. Solid-State Lett. 6 (2003) B12

[4.2]   J.M. Macak, H. Tsuchiya, P. Schmuki, Angew. Chem. 117 (2005) 2136

[4.3]   J.M. Macak, K. Sirotna, P. Schmuki, Electrochim. Acta 50 (2005) 50

[4.4]   J.M. Macak, H. Tsuchiya, L. Taveira, S. Aldabergerova and P. Schmuki, Angew. Chem. Int. Ed. 44 (2005) 44

[4.5]   M. Grätzel, Nature 414 (2001) 338

[4.6]   D. Gong, C.A. Grimes, O.K. Varghese, W. Hu, R.S. Singh, Z. Chen, E.C. Dickey, J. Mater. Res. 16 (2001) 3331

[4.7]   S. Bauer, S. Kleber, P. Schmuki, Electrochem. Comm. 8 (2006) 1321

[4.8]   J.M. Macak, H. Hildebrand, U. Marten-Jahns, P. Schmuki, J. Electroanal. Chem. 621 (2008) 254

[4.9]   J.W. Schultze, M.M. Lohrengel, Electrochim. Act. 45 (2000) 2499

[4.10] H.E. Prakasam, K. Shankar, M. Paulose, O.K. Varghese, C.A. Grimes, J. Phys. Chem. 111 (2007) 7235

[4.11] K. Yasuda, P. Schmuki, Electrochim. Act. 52 (2007) 4053

[4.12] L.V. Taveira, J.M. Macak, H. Tsuchiya H, L.F.P. Dick and P.J. Schmuki, Electrochem. Soc. 152 (2005) B405

[4.13] G.K. Mor, O.K. Varghese, M. Paulose, K. Shankar, C.A. Grimes, Solar Energy Mat. Solar Cells 90 (2006) 2011

[4.14] J.M. Macak, H. Tsuchiya, A. Ghicov, K. Yasuda, R. Hahn, S. Bauer, P. Schmuki, Curr. Opinion Sol. State Mat. Science 11 (2007) 3

[4.15] S. Kelly, F.H. Pollak, M. Tomkiewicz, J. Phys. Chem. B 101 (1997) 2730

[4.16] M. Gotić, M. Ivanda, S. Popović, S. Musić, A. Sekulić, A. Turković, K. Furić, J. Raman. Spec. 28 (1997) 555

[4.17] D. Bersani, P.P. Lottici, T. Lopez, J. Sol-Gel Science Tech. 13 (1998) 849

[4.18] S. Balaji, Y. Djaoued, J. Robichaud, J. Raman Spec. 37 (2006) 1416

[4.19] G. Gouadec, P. Colomban, Pr. Cryst. Growth Char. Mat. 53 (2007) 1.

[4.20] W.F. Zhang, M.S. Zhang, Z. Yin, Phys. Stat. Sol. 179 (2000) 319.

[4.21] M.A. Khan, H.-T. Jung, O.-B. Yang, Chem. Phys. Lett. 458 (2008) 134.

[4.22] L.D. Zhang, C.M. Mou, Nanostruct. Mater. 6 (1995) 831

[4.23] N. Daude, C. Gout, C. Jouanin, Phys. Rev. B 15 (1977) 3229

[4.24] W.F. Zhang, M.S. Zhang, Z. Yin, Phys. Stat. Sol. (a) 179 (2000) 319

[4.25] Y.K. Lai, L. Sun, C. Chen, C.G. Nie, J. Zuo, C.J. Lin, Appl. Surf. Science 252 (2005) 1101

[4.26] N. Serpone, D. Lawless, R. Khairutdinov, J. Phys. Chem. 99 (1995) 16646

[4.27] M.A. Khan, H.-T. Jung, O.-B. Yang, Chem. Phys. Lett. 458 (2008) 134

[4.28] G.K. Mor, O.K. Varghese, M. Paulose, C.A. Grimes, Adv. Funct. Mater. 15 (2005) 1291

[4.29] L.V. Hong, N.T.H. Le, N.C. Thuan, N.D. Thanh, N.X. Nghia, N.X. Phuc, J. Raman Spec. 36 (2005) 946

[4.30] H.C. Choi, Y.M. Jung, S.B. Kim, Vibrational Spectroscopy 37 (2005) 33

[4.31] B. Liu, L. Wen, X. Zhao, Mat. Chem. Phys. 106 (2007) 350

[4.32] H. Richter, Z.P. Wang, L. Ley, Sol. Stat. Commun. 39 (1981) 625

[4.33] P.M. Fauchet, I.H. Campbell, Crit. Rev. Solid. State Mater. Sci. 14 (1998) S79

[4.34] J. Zhi, K. Zhang, X. Xie, Phys. Rev. B 55 (1997) 9263

[4.35] M. Ivanda, S. Music, M. Gotic, A. Turkovic, A. M. Tonejc, O. Gamulin, J. Molec. Struct. 480 – 481 (1999) 641

CHAPTER FIVE
Al$_2$O$_3$-Coated TiO$_2$ Nanotubes

The results of the Al$_2$O$_3$-coated TiO$_2$ nanotubes, of which the synthesis was discussed in Chapter Two, will be presented in this chapter. The nanotubes used during the dip-coating process were synthesised at the optimum anodisation bath conditions, which were found in Chapter Four to be an anodisation voltage of 60 V, electrolyte solution consisting of 2 M H$_2$O + 0.15 M NH$_4$F + ethylene glycol and an anodisation time of 6 hours. These conditions yielded nanotube arrays of an average length, diameter and wall thickness of 15 µm, 50 nm and 15 nm, respectively.

As stated in Chapter One, core-shell TiO$_2$ nanoparticles primarily reduce the recombination between electrons in the TiO$_2$ conduction band and holes in the entwined electrolyte. In particular, it has been shown that coating TiO$_2$ nanoparticles with a nanometer sized layer of Al$_2$O$_3$ minimises the reaction between the electrons and I$_3^-$ at the TiO$_2$/electrolyte interface [5.1], leading to improvement in the overall cell efficiency.

Wu et al. [5.2] showed that the Al$_2$O$_3$ coating also increases dye adsorption and decreases trap sites on TiO$_2$, thereby further increasing the DSC performance. In this chapter, the strategy of core-shell nano-structures will be applied to the nanotubes, by using a modified Yoldas dip-coating technique [5.3] as described by Palomares et al [5.1].

The chapter will commence with a discussion of the surface morphology of a layer of TiO$_2$ nanoparticles coated with the Al$_2$O$_3$ overlayer. The strategy used to coat the nanoparticles will then be applied to a layer of nanotubes and investigated. The morphology was studied using atomic force microscopy (AFM) as to characterise the as-synthesised materials without processing prior to characterisation. Focused ion beam scanning electron microscopy (FIB-SEM) analyses of a cross-section of the coated nanotubes were performed to investigate the effect of the Al$_2$O$_3$ overlayer on the morphology of the nanotubes.

The crystalline structure of the uncoated and coated nanoparticles and nanotubes will then be discussed following study of the respective x-ray diffraction (XRD) patterns, whereas transmission electron microscopy (TEM) allowed for determination of the core-shell structure nature of the different nanostructures.

The chapter will conclude with a discussion on the dye-adsorption properties of the Al$_2$O$_3$-coated TiO$_2$ materials. An important requirement of the TiO$_2$ film used in a DSC is its ability to adsorb dye molecules. By coating the TiO$_2$ surface with a layer of Al$_2$O$_3$ a concern arises on the dye adsorption ability of the Al$_2$O$_3$-TiO$_2$ film. In this regard, ultraviolet-visible (UV-vis) spectroscopy proves to be an important characterisation technique and was used to charaterise the dye adsorption properties of the different films of nanostructures.

5.1 Morphology of Al$_2$O$_3$-Coated TiO$_2$ Nanoparticles

Figure 5.1 compares 2 µm x 2 µm atomic force microscopy (AFM) micrographs of a 15 µm thick layer of TiO$_2$ nanoparticles, prepared according to [5.4], before and after coating with Al$_2$O$_3$, as explained in Chapter 2.2.3. During the synthesis it was found that dipping the TiO$_2$ layer in an aluminium butoxide precursor concentration of 1M for 30 seconds, followed by sintering at 430 ºC for 30 minutes in air at atmospheric pressure yielded the most uniform layer of Al$_2$O$_3$, exhibiting no cracks in its morphology (see Figure 2.11 of Chapter 2).

The absence of cracks in the electron transport film is a major necessity prior to manufacturing DSCs, as it has been shown that cracking of the TiO$_2$ film results in poor device performance [5.5, 5.6]. Hence, the results presented in Figure 5.1 are that of a TiO$_2$ layer coated at the above stated sol-gel conditions.

The film of uncoated TiO$_2$ nanoparticles have an average particle size of 35 nm as shown by the particle distribution of Figure 5.1 (b). Upon coating the nanoparticles with the Al$_2$O$_3$ overlayer, the average particle size increases by 10 nm to roughly 45 nm as can be seen in Figure 5.1 (d). The increase in particle size diameter suggests uniform coating of the individual TiO$_2$ nanoparticles.

Roughness analyses of the respective AFM micrographs were performed to investigate the effect of the Al$_2$O$_3$ coating on the surface topology of the TiO$_2$ film. The roughness encountered by the AFM tip is indicative of the unevenness

129

at the surface of the layer of nanoparticles. Hence, this simple technique can be used as a guide in determining (a) if the Al$_2$O$_3$ coated the individual nanoparticles or just covered the TiO$_2$ surface in a blanket fashion and (b) whether the Al$_2$O$_3$ coating decreases the porosity of the nanoparticle film.
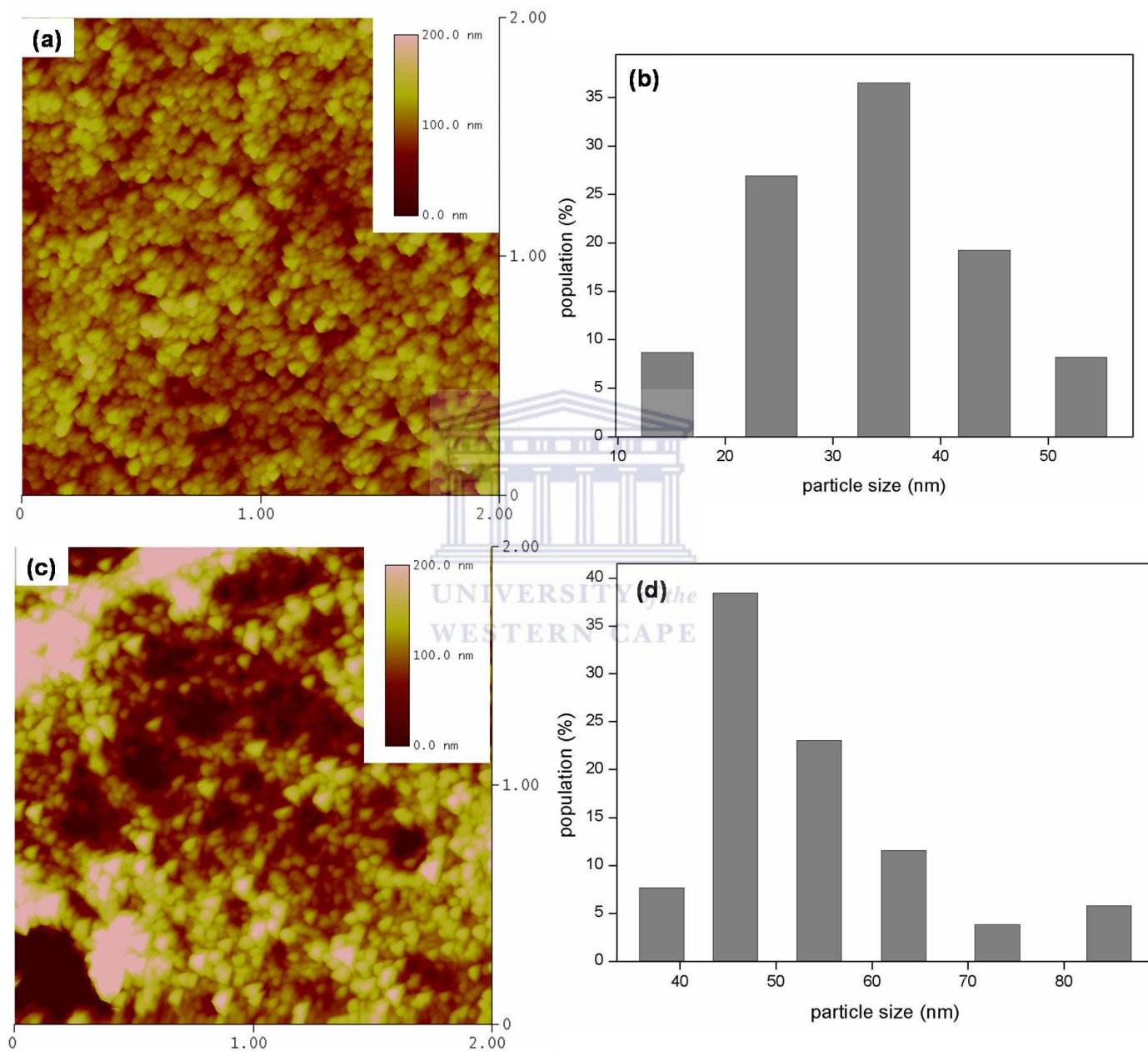
Figure 5.1: 2 μm x 2 μm AFM micrographs of a 15 μm thick TiO$_2$ nanoparticle film (a) before and (c) after coating with a layer of Al$_2$O$_3$. The respective particle distributions are shown in (b) and (d).
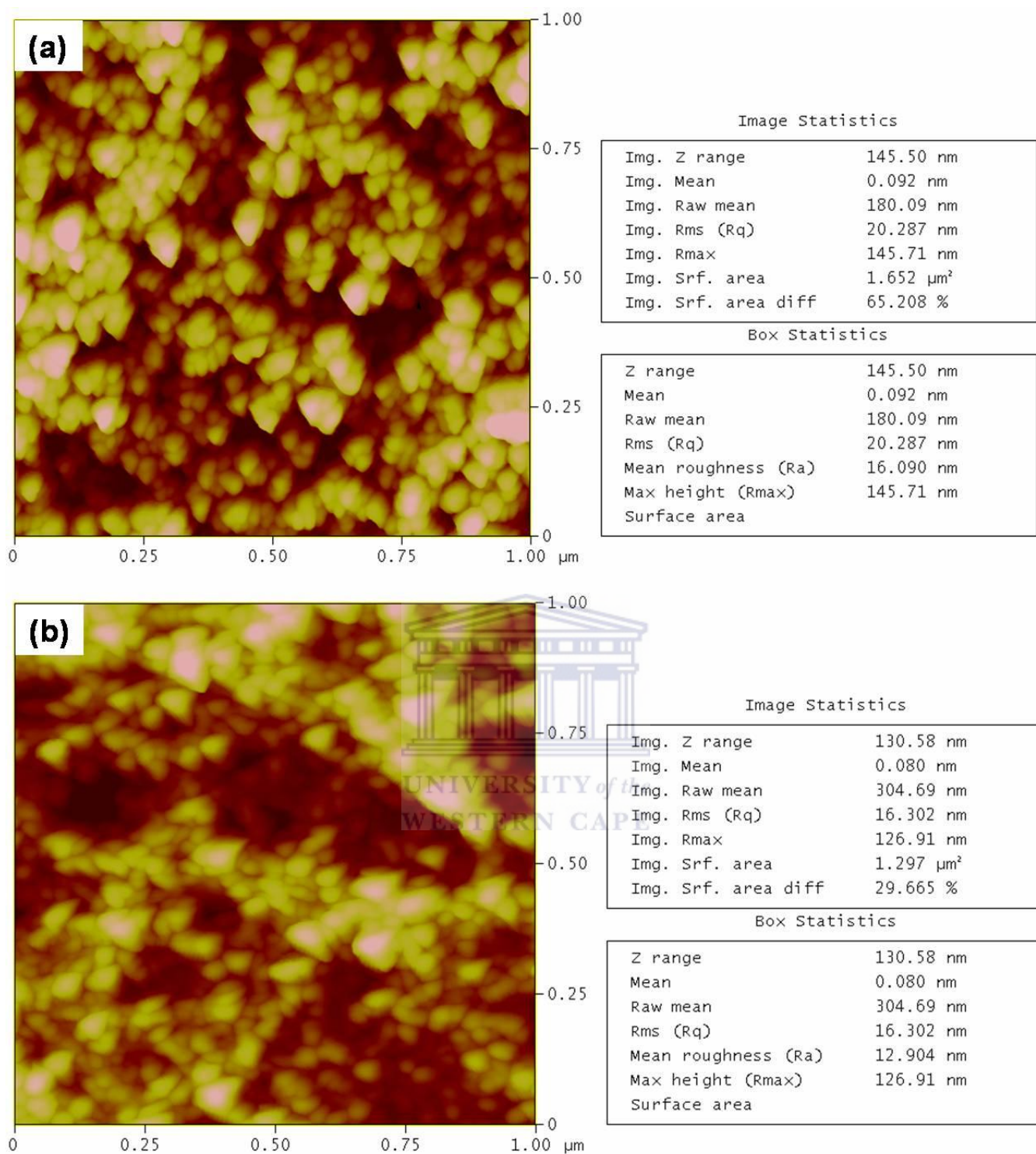
Figure 5.2: Roughness analyses of (a) the uncoated and (b) Al$_2$O$_3$-coated TiO$_2$ nanoparticles

Figure 5.2 shows the roughness analyses for the uncoated and Al$_2$O$_3$-coated layers of TiO$_2$ nanoparticles. The roughness statistics are summarised in the accompanied text boxes. The important figure to note is the root mean square (rms) roughness value in the respective text boxes. It can be seen that prior to dip-coating the TiO$_2$ nanoparticle film with an average particle size of 35 nm has a surface roughness of 20.287 nm, which decreases to 16.302 nm after dip-coating. The decrease in roughness before and after coating implies that the AFM tip encountered less troughs in between adjacent nanoparticles, which suggests that the Al$_2$O$_3$ layer filled these valleys and by so doing may decrease the porosity of the TiO$_2$ film.

TEM studies were performed on the nanoparticles to gather greater insights into the core-shell nature of the structures. Figure 5.3 shows TEM micrographs of the uncoated and coated nanoparticles. The average particle size of the uncoated TiO$_2$ nanoparticles in Figure 5.3 (a) is approximately 35 nm, in coherence with the average particle size obtained from the AFM images in Figure 5.1.

The high-resolution TEM image of Figure 5.3 (b) shows that the TiO$_2$ nanoparticles grow predominantly in the [101] direction with stacking of the anatase (101) planes, a distance of 3.54 Å apart. The set of planes intersecting the (101) planes are the (004) planes, with a d spacing of approximately 2.41 Å.
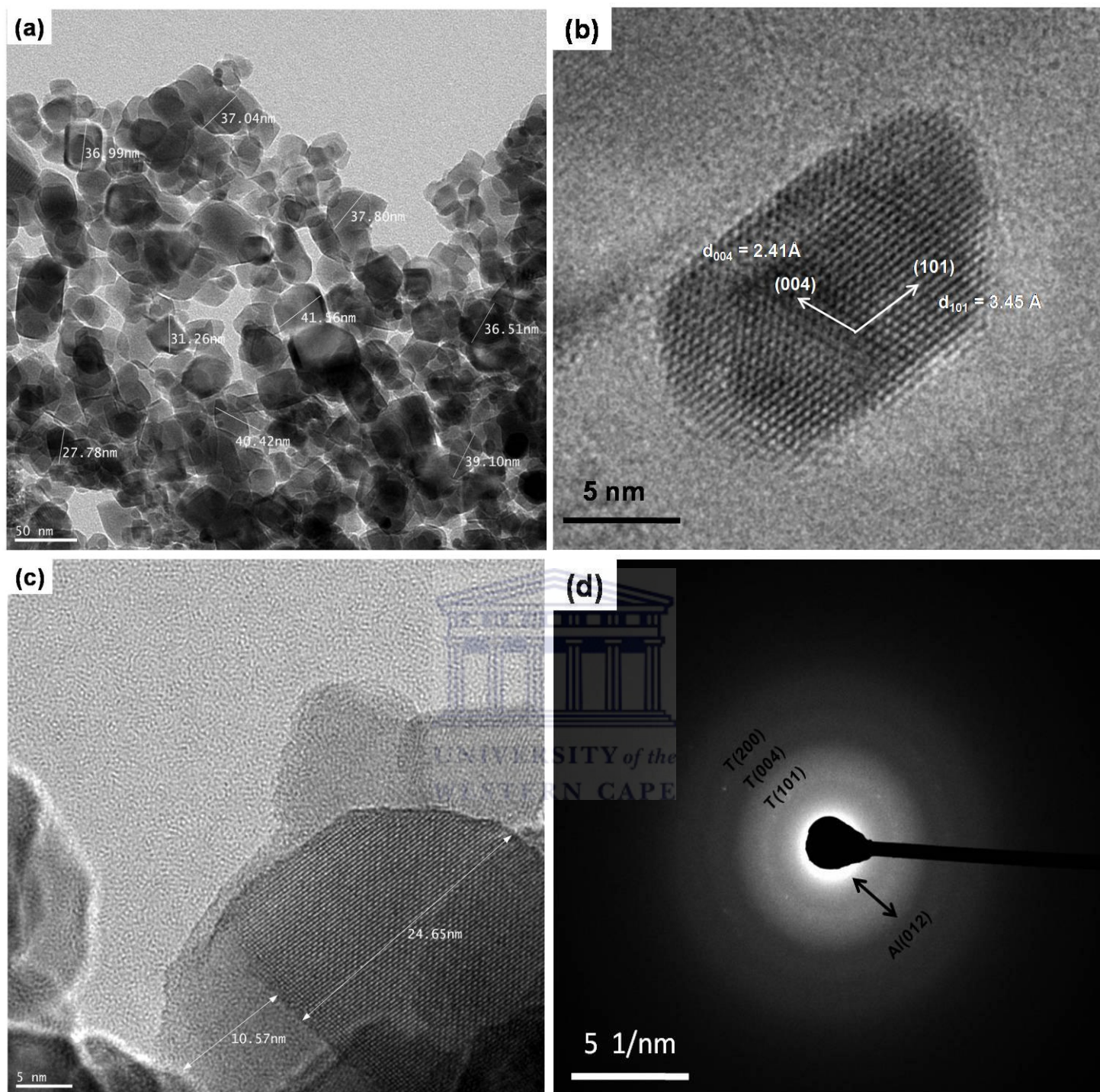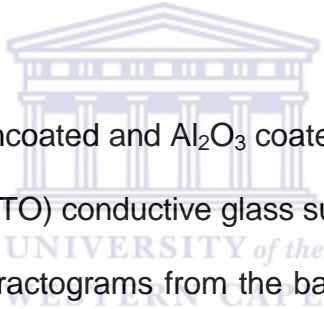
Figure 5.3: (a) TEM micrograph of a cluster of TiO$_2$ nanoparticles, prior to sol-gel dip-coating, (b) high-resolution TEM micrograph of a single TiO$_2$ nanoparticle showing that the particles grow in the (101) direction, (c) high resolution TEM micrograph of an Al$_2$O$_3$ coated TiO$_2$ nanoparticle with (d) the corresponding SAED pattern

The high resolution TEM image of a coated TiO$_2$ nanoparticle is shown in Figure 5.3 (c) with the corresponding selected area diffraction (SAED) pattern shown in Figure 5.3 (d). The micrograph shows a coating varying between of approximately 10 nm thick Al$_2$O$_3$ layer around the TiO$_2$ nanoparticle. The coating is not uniform and varies between 3 and 10 nm. Furthermore, the coating is amorphous as confirmed by the SAED of Figure 5.3 (d), with a broad diffused band detected in the diffraction pattern, indicative of distorted (012) set of planes of corundum (α - Al$_2$O$_3$, JCPDS Card No. 10-137). The diffraction from the anatase TiO$_2$ (101), (004) and (200) sets of planes at calculated at d-spacings of 3.56, 2.45 and 1.93 Å, respectively, are also visible in Figure 5.3 (d).

XRD patterns of the uncoated and Al$_2$O$_3$ coated TiO$_2$ nanoparticle films on a fluorine doped tin oxide (FTO) conductive glass substrate are shown in Figure 5.4. The figure includes diffractograms from the bare glass/FTO substrate and the glass/FTO dip-coated in the Al$_2$O$_3$ sol-gel solution. Analyses of the FTO coated glass substrate reveal diffraction primarily from SnO$_2$ crystalline phases, whereas the glass/FTO substrate dipped in the sol-gel have no crystalline features, only a broad amorphous band centred around 2θ ~ 25°. The absence of highly crystalline features at high 2θ values suggests no boehmite, γ-AlO(OH) formation and hence complete transformation into the corundum, α-Al$_2$O$_3$, phase following the sintering process. Therefore the broad amorphous band in and around 25° is suggestive of short range order from the (012) phase of α-Al$_2$O$_3$. The diffraction patterns of the coated and uncoated layer of TiO$_2$ nanoparticles on the glass/FTO substrate show only diffraction peaks from

anatase TiO$_2$ and verifies that an amorphous Al$_2$O$_3$ layer coated onto the nanoparticles.

The XRD data are in very good agreement with the SAED pattern shown in Figure 5.3 (d) and confirms that dip-coating for 30 seconds 1M aluminium butoxide sol-gel, followed by sintering at 430 °C for 30 minutes in air at atmospheric pressure yields TiO$_2$ nanoparticles coated with an amorphous Al$_2$O$_3$ coating. The results are consistent with findings published by various groups [5.1, 5.2, 5.7, 5.8].
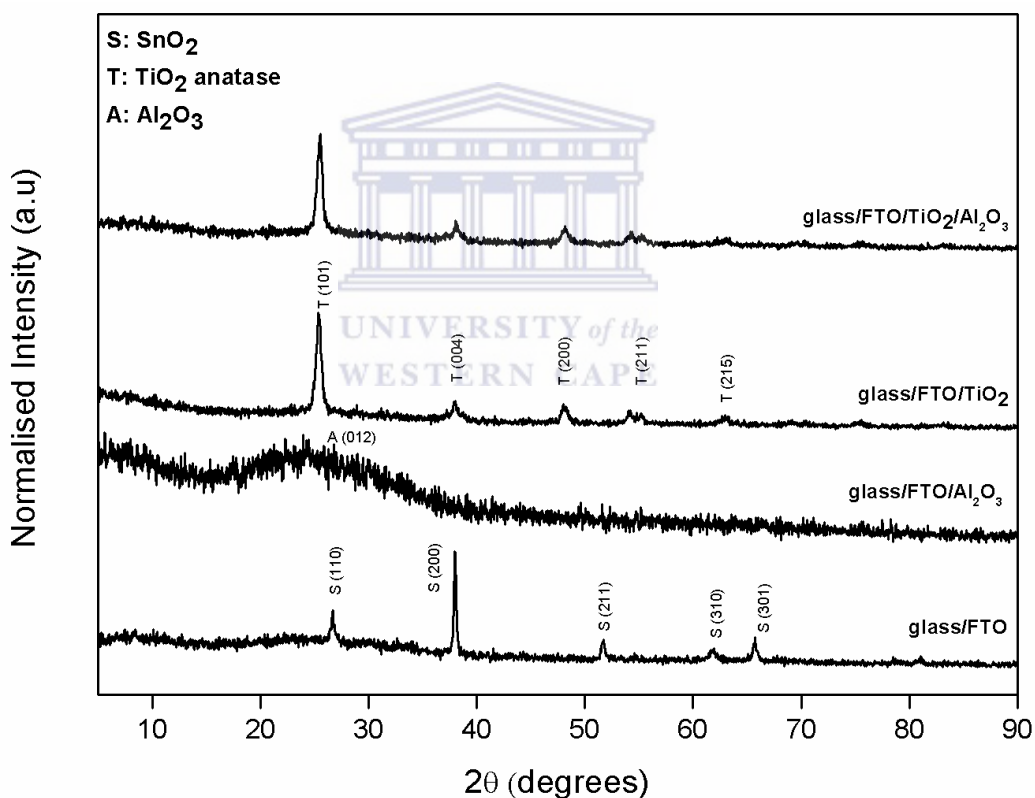
Figure 5.4: XRD patterns of the TiO$_2$ nanoparticles, before and after being coated with Al$_2$O$_3$. Included are a diffraction pattern of the glass substrate covered by a FTO layer; and the glass/FTO substrate coated with the Al$_2$O$_3$ over layer

5.2 Morphology of Al$_2$O$_3$-Coated TiO$_2$ Nanotubes

Figure 5.5 shows AFM micrographs of a bare and Al$_2$O$_3$ coated TiO$_2$ nanotube layer. The nanotube films were synthesised at the optimised anodisation conditions as found in Chapter Four. The average inner diameter size of the bare nanotube layer is approximately 45 nm, as shown in Figure 5.5 (b), whereas after Al$_2$O$_3$ coating the diameter decreases to roughly 17 nm, as shown in Figure 5.5 (d).

The decrease in nanotube inner diameter after Al$_2$O$_3$ coating is to be expected because the Al$_2$O$_3$ overlayer not only covers the outside surface of the nanotube wall, but also the interior regions, hence causing a reduction in diameter. The corresponding surface roughness analysis of the nanotube films before and after coating yields a rms surface roughness of 190 and 150 nm, respectively, suggesting a smoother surface area after coating. The same result was obtained during the Al$_2$O$_3$ coating of the layer of TiO$_2$ nanoparticles in Section 5.1 above. In this case the smoother surface is as a result of the filling of the voids created by the nanotube diameter.

TEM micrographs of the nanotube films before and after coating are shown in Figure 5.6 (a) and (c), respectively. The SAED pattern of Figure 5.6 (b) shows that the bare nanotubes are poly-crystalline with the diffraction rings clearly visible. The most intense diffraction is that of the anatase (101) sets of planes with a d-spacing measured at 5.56 Å. The outer diffraction rings are that of anatase (004) and (200) with a d-spacing of 2.47 and 1.93 Å, respectively.
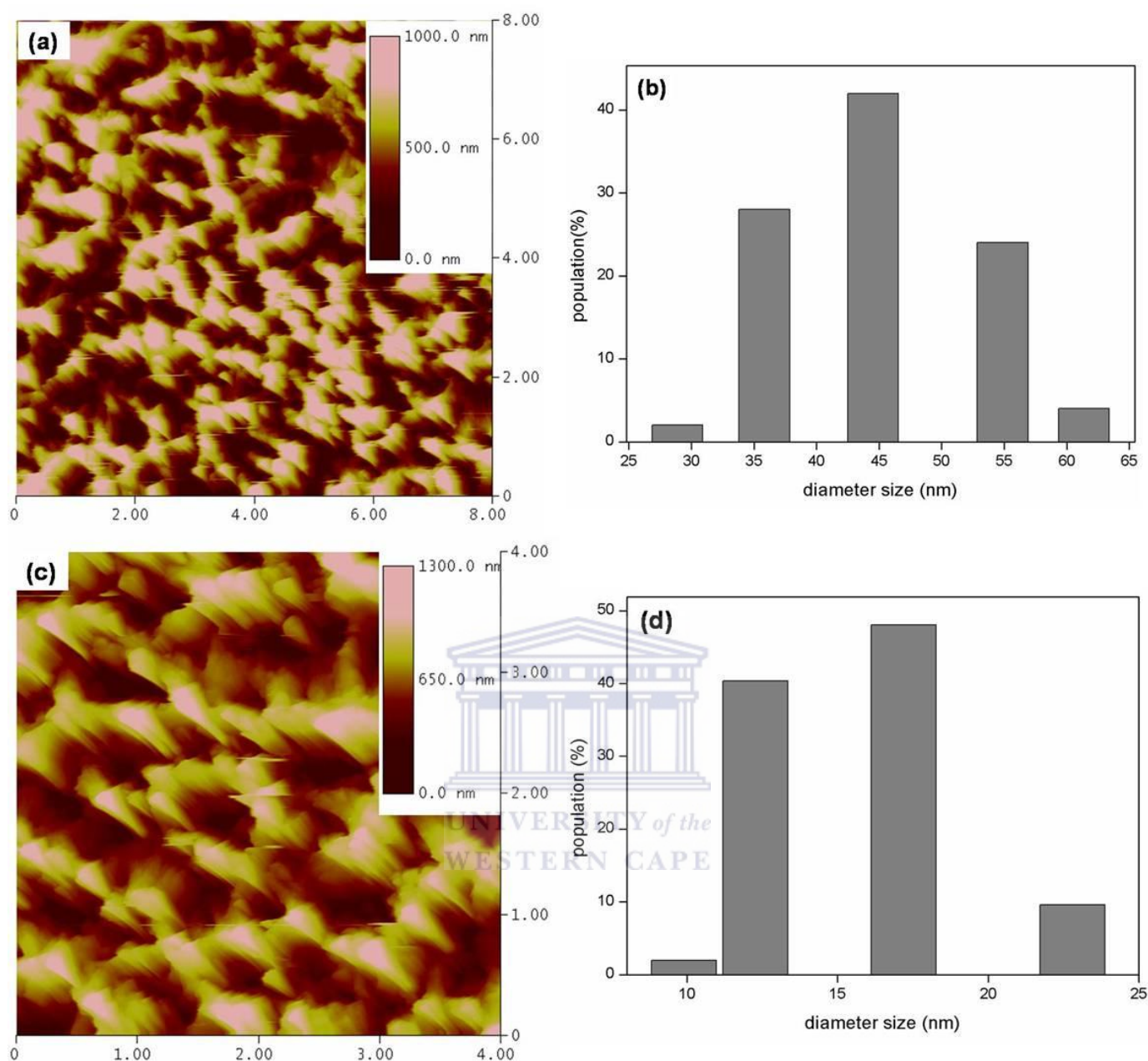
Figure 5.5: AFM micrographs of (a) bare TiO$_2$ nanotube and (c) Al$_2$O$_3$ coated TiO$_2$ nanotube film. The corresponding diameter size distributions are shown in (b) and (d).

The TEM micrograph of Figure 5.6 (c) clearly shows that the nanotubes are coated with a layer of Al$_2$O$_3$ of thickness varying between 4 and 7 nm, as measured from the high resolution inset. The corresponding SAED of Figure

5.6 (d) shows strong diffraction rings from the (004) and (200) planes, but very weak scattering from the (101) sets of planes. Instead a broad, diffused band is measured in and around the same range of the anatase (101), stemming from the amorphous Al$_2$O$_3$ phases.
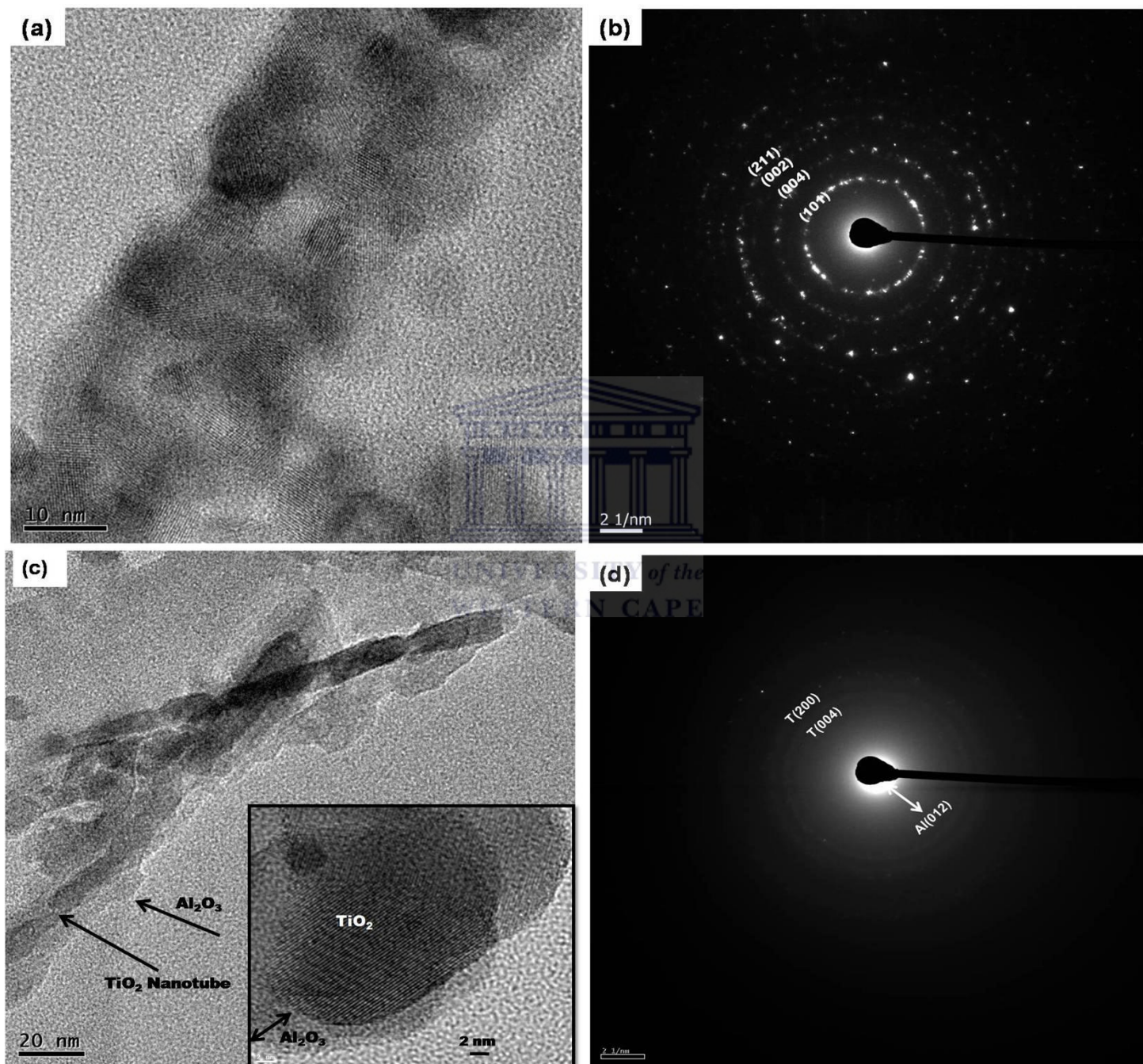
Figure 5.6: TEM micrographs of (a) bare TiO$_2$ nanotubes and (c) Al$_2$O$_3$ coated TiO$_2$ nanotubes; SAED patterns of the (b) bare and (d) coated nanotubes

Figure 5.7 compares the XRD pattern of a layer of bare nanotubes to that of a nanotube film coated with Al_2O_3. It can be seen that the bare nanotubes are crystallised in the anatase form with the most intense peak that of the (101) sets of planes, diffracting at $2\theta = 25.43°$, which equates to a d-spacing of 3.49 Å. Similarly, the (004) and (200) sets of planes are measured at $2\theta = 38.61$ and $48.55°$ yielding d-spacings of 2.33 and 1.87 Å, respectively. The diffraction pattern of the Al_2O_3 coated layer of nanotubes shows a broad hump in and around $2\theta = 25°$, which is attributed to the amorphous Al_2O_3 coating, as was detected with the TEM micrographs and SAED patterns of Figure 5.6. The XRD diffractograms are very consistent with the SAED data presented in Figure 5.6 (b) and (d) and confirm the coating of the TiO_2 nanotubes with Al_2O_3.
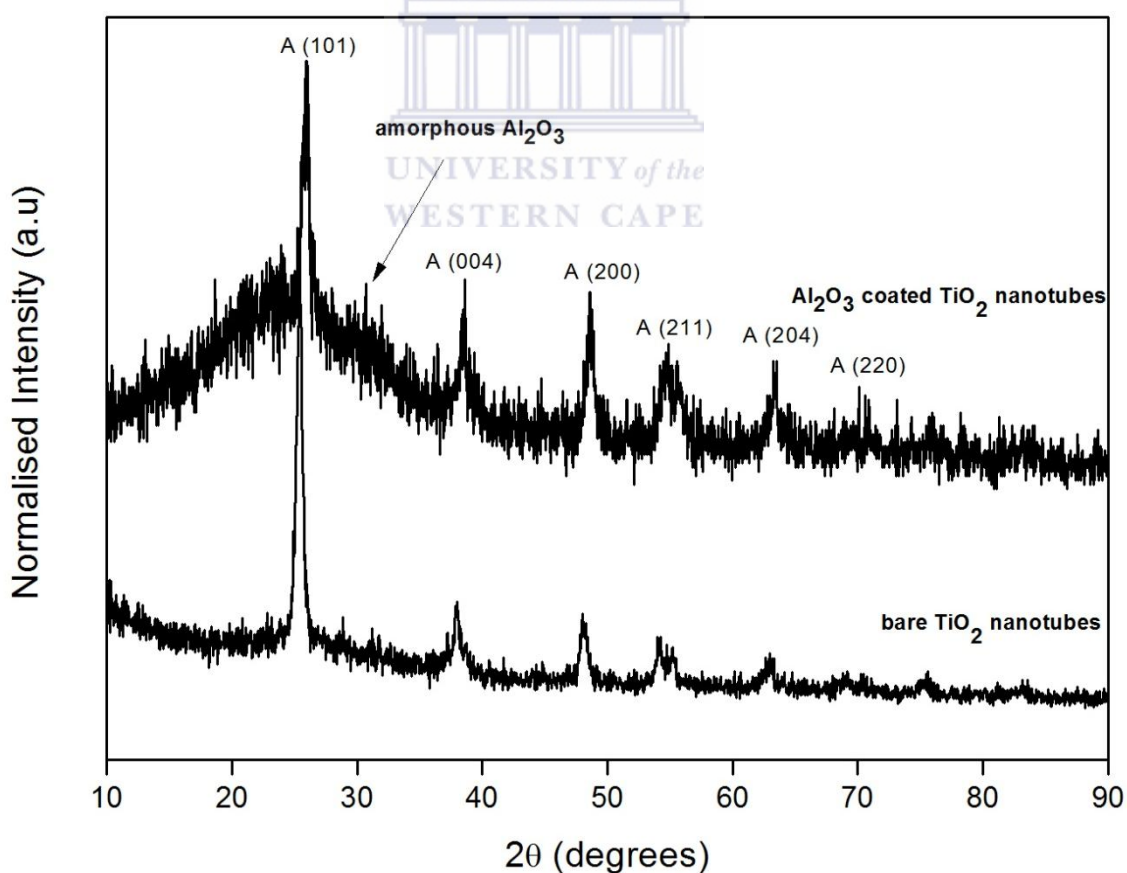
Figure 5.7: XRD patterns of a layer of bare TiO_2 nanotubes and that of a layer of tubes coated with Al_2O_3

5.3 Dye Adsorption Properties

The dye adsorption properties of the bare TiO_2 and Al_2O_3 coated electrodes were characterised by means of UV-vis absorbance spectra and the method reported by Tolvanen [5.9]. This is an important analysis because the TiO_2 nanostructured electrode acts as support for the Ru dye within the DSC and the amount of dye adsorbed onto surface is directly dependent on the TiO_2 morphology. By coating the TiO_2 nanostructures with a layer of metal-oxide, the dye-adsorption ability of the TiO_2 electrode must not be compromised.

Figure 5.8 compares the UV-vis spectra of bare TiO_2 nanoparticles and nanotubes soaked overnight in Ru N719 dye to that of the Al_2O_3-coated nanostructures immersed in N719. For all experiments, 1 x 1 cm^2 films of thickness approximately 15 µm thick were used during the dye-adsorption in order to compare and normalise the absorbance data. The dye adsorbed nanoparticle and nanotube films were then scraped from the respective glass/FTO and Ti substrates and dispersed in 1 M NaOH in accordance with [5.9].

In its ground state, the N719 dye molecule (shown in Figure 5.8) has its Ru metal in an oxidised state. Upon excitation, the Ru metal loses the extra electron(s) to the bonded carboxylate ligand(s), through a process called the metal-to-ligand ($4d$ - π^*) charge transfer (MLCT). In addition, Ru-based dyes also ligand-centered charge transfer (LCCT) transitions (π - π^*). For DSC application the $4d$ - π^* transitions are of importance because the electrons are transported during these transitions are injected via the carboxylate group to the TiO_2 [5.10].

140
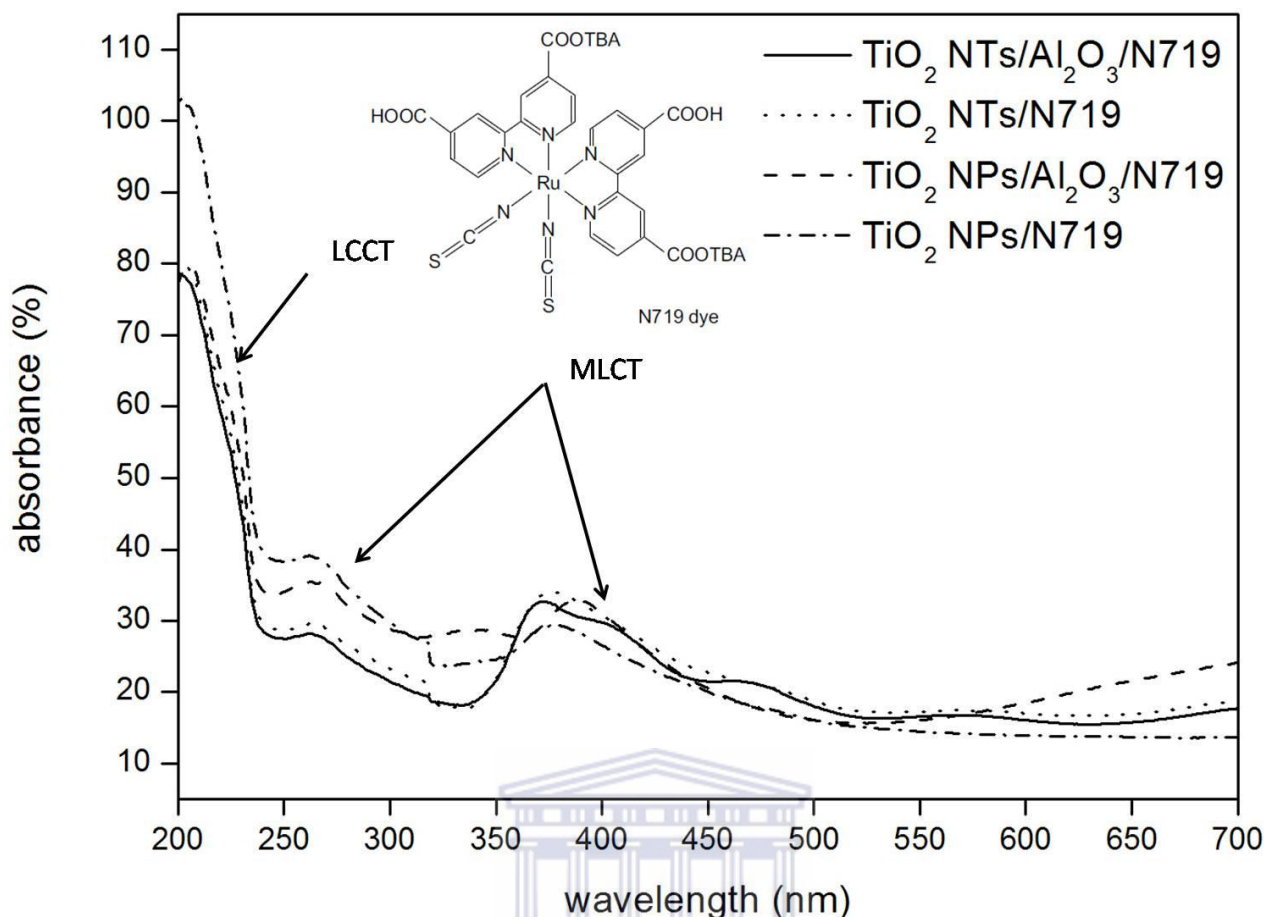
Figure 5.8: UV-Vis absorbance spectra of the N719 dye adsorbed bare and Al$_2$O$_3$ coated TiO$_2$ nanoparticle and nanotube films

Two broad absorption peaks are readily observed in Figure 5.8 in the ranges between 250 to 300 nm and 350 to 450 nm, respectively and are distinctive of 4d - π* transitions in the N719 dye during MLCT. The high energy transition observed in Figure 5.8 at wavelengths below 250 nm is characteristic of π - π* transitions during LCCT.

As shown the Al$_2$O$_3$ coated TiO$_2$ films exhibit greater MLCT characteristics and hence improved dye adsorption. Ganapathy et al [5.11] found an increase in the dye adsorption ability of TiO$_2$ nanoparticles coated with a 2 nm thick layer of Al$_2$O$_3$ deposited by means of atomic layer deposition. Wu et al [5.12] showed

that sol-gel deposited TiO$_2$ nanoparticle films followed by oxygen plasma treatment increases the dye adsorption properties of the TiO$_2$ films and similar trends have also been observed by various other groups, e.g. [5.13, 5.14]. The enhanced dye adsorption observed in Al$_2$O$_3$ coated TiO$_2$ nanostructured films is attributed to the favourable attachment of the carboxylate ligand groups of the N719 dye to the more basic surface of the Al$_2$O$_3$. In particular the greater dye adsorption is attributed to the higher isoelectric point (IEP) of Al$_2$O$_3$ compared to TiO$_2$.

At the IEP of a solid its zeta potential is zero and is found by adjusting the pH to the appropriate value. The oxide surface responds by becoming more positive as the pH is lowered by undergoing the following reaction:

$$\text{-MOH} + \text{H}^+ \rightarrow \text{-MOH}_2^+ \tag{5.1}$$

If the pH is raised the surface becomes more negative according to:

$$\text{-MOH} + \text{OH}^- \rightarrow \text{-MO}^- + \text{H}_2\text{O} \tag{5.2}$$

Therefore the surface tends to be more negative the higher the pH and more positive the lower the pH. At some intermediate pH, zeta will be zero and at that point the IEP is measured.

Figure 5.9 shows a table of the IEPs of the most common metal-oxides and it can be seen that Al$_2$O$_3$ has a greater IEP than TiO$_2$. This implies that in its natural state alumina tends to have a more negative surface than titania resulting in its more favourable bonding with the carboxylate attachment groups of the N719 dye molecule. From Figure 5.8 it can also be seen that the TiO$_2$ nanotubes films absorb, on average about 10% less radiation than the nanoparticle layers. This implies a lower dye adsorption concentration

according to [5.9], which is attributed to a lower surface area of the nanotube films compared to a layer of nanoparticle of the same thickness.

pH of the isoelectric point of various oxides

Oxide	pH of i.e.p.
Silica (SiO$_2$)	2 - 3
Titania (TiO$_2$)	5.8
Haematite (Fe$_2$O$_3$)	6.5
Alumina (Al$_2$O$_3$)	9.1

Figure 5.9: IEP values of the most common metal-oxides [5.15]
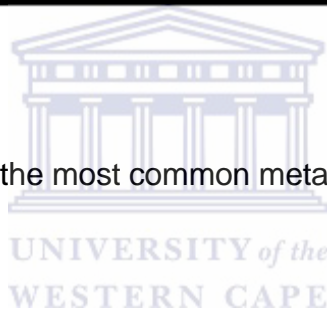
Conclusion

This chapter investigated the morphology, crystallinity and dye-adsorption properties of core-shell Al$_2$O$_3$-coated TiO$_2$ nanotubes. A simple synthesis protocol was followed based on previous work done on films of TiO$_2$ nanoparticles. AFM micrographs showed that the average particle size of a film of TiO$_2$ nanoparticles increases after coating with the Al$_2$O$_3$. Similarly it was found that the average nanotube diameter increased post sol-gel deposition, and served as the first indications that the nanotubes indeed are coated with a layer of Al$_2$O$_3$.

HR-TEM, SAED and XRD analyses confirmed the coating of the nanotube walls with a thin layer of amorphous Al$_2$O$_3$ of thickness between 4 and 7 nm. To the best of our knowledge and based on published literature, this is the first time that a simple sol-gel dip-coating process has been successfully applied to uniformly coat anodised TiO$_2$ nanotube layers. In addition, UV-vis absorbance spectra showed that the dye-adsorption ability of the nanotubes are enhanced by the Al$_2$O$_3$ coating and hence is a viable material for DSC application.

UNIVERSITY *of the*

WESTERN CAPE

References

[5.1]   E. Palomares, J.N. Clifford, S.A. Haque, T. Lutz and J.R. Durrant, Chem. Commun. (2002) 1464

[5.2]   S. Wu, H. Han, Q. Tai, J. Zhang, S. Xu, C. Zhou, et al. J. Power Sources 182 (2008) 119

[5.3]   B.E. Yoldas, J. Mater. Sci. 10 (1975) 1856

[5.4]   H.-J. Koo, J. Park, B. Yoo, K. Yoo, K. Kim, N.-G. Park, Inorg. Chim. Acta 361 (2008) 677

[5.5]   S. Ito, P. Chen, P. Comte, M. K. Nazeeruddin, P. Liska, P. Péchy and M. Grätzel, Prog. Photovolt: Res. Appl. DOI : DOI: 10.1002/pip.768

[5.6]   S. Ito, T. Takeuchi, T. Katayama, M. Sugiyama, M. Matsuda, T. Kitamura, et al. Chem. Mater. 15 (2003) 2824

[5.7]   X. Zhang, I. Sutantoa, T. Taguchia, K. Tokuhiroa, Q. Menga, T. Rao, et al. Sol. Energy Mat. Solar Cells 80 (2003) 315

[5.8]   M. Jayasankar, S. Ananthakumar, P. Mukundan, W. Wunderlich and K.G.K. Warrier, J. Sol. State Chem. 181 (2008) 2748

[5.9]   A. Tolvanen, "*Characterisation and Manufacturing Techniques of Dye-Sensitised Solar Cells*", M.Sc. Thesis, Helsinki University of Technology, Helsinki Finland, pp. 48 – 50 (2003)

[5.10] N. Hirata, J. Lagref, E. Palomares, et al. Chem. Eur. J. 10 (2004) 595

[5.11] V. Ganapathy, B. Karunagaran, S.-W. Rhee, J. Power Sources 195 (2010) 5138

[5.12] S. Wu, H. Han, Q. Tai, et al. J. Power Sources 182 (2008) 119

[5.13] E. Palomares, J.N. Clifford, S.A. Haque, T. Lutz, J.R. Durrant, J. Am. Chem. Soc. 125 (2003) 475

[5.14] P. Qu, G.J. Meyer, Langmuir 17 (2001) 6720

[5.15] R. Greenwood and L. Bergstroem, J. European Ceram. Soc. 17 (1997) 537

CHAPTER SIX
Photovoltaic Properties

This chapter will discuss the application of the bare and Al_2O_3 coated TiO_2 nanoparticles and nanotubes, reported in Chapter 5, in the dye-sensitised solar cell (DSC). The DSCs under investigation were constructed as discussed in Chapter 2.3 and their performance measured by means of photocurrent density versus voltage (I – V) graphs, as reported in Chapter 3.3.2. The I – V curve data will be discussed in conjunction with electrochemical impedance spectroscopy (EIS) measurements of the respective devices, as detailed in Chapter 3.3.1.

In the first instance the DSC performance of the bare and Al_2O_3 coated TiO_2 nanoparticles will be compared. The I – V data will be analysed and a theoretical model will be constructed based on the data obtained from the respective equivalent circuit fits to the EIS data. This methodology will then be applied to DSCs constructed with bare and Al_2O_3 coated TiO_2 nanotubes.

The chapter will conclude with a comparison of the photovoltaic data and electrical circuits of the four respective solar cells. A detailed discussion of the mechanisms responsible for the I – V characteristics, based on the conclusions drawn from the previous sections, will follow and possible future studies on the subject will also be addressed.

6.1 Application of Bare and Al$_2$O$_3$-Coated TiO$_2$ Nano-particles in DSCs

Figure 6.1 compares the I – V curves of DSCs fabricated with 15 μm thick bare and Al$_2$O$_3$-coated TiO$_2$ nanoparticle films as the electron transport media of the working electrodes. The I – V data presented are the averaged data of four DSCs of each type. As was discussed in Chapter Three, the real life I – V relationship of the DSC can be modeled by equation 3.37, given as

$$I(V) = I_{sat}\left[exp\frac{e_0 V - e_0 R_s I}{m_D k_B T} - 1\right] + I_{sc} + \frac{V - R_s I}{R_{sh}}$$

(6.1)

with I$_{sat}$ the diode saturation current, e$_0$ the electron charge, m$_D$ the diode ideality factor, k$_B$ the Boltzmann constant, T the room temperature, R$_s$ the series and R$_{sh}$ the shunt resistance and I$_{sc}$ the short circuit current density. The entity, $\frac{V-R_s I}{R_{sh}}$ is known as the shunt current, I$_{sh}$ and is a measure of the resistance between the two working electrodes of the DSC through undesirable routes. Hence a low shunt current and conversely high shunt resistance is desirable in a solar cell. The light-to-current conversion efficiency, η, is calculated from the I – V curve and is given by

$$\eta = \frac{P_{max}}{P_{in}} = FF \times \frac{I_{sc} V_{oc}}{P_{in}}$$

(6.2)

where P$_{max}$ is the maximum power point on the I - V curve, P$_{in}$ the incident power flux and V$_{oc}$ the open circuit voltage.

The critical data obtained from the curves of Figure 6.1 are tabulated and presented in the accompanying table in Figure 6.1. It can readily be seen that the Al$_2$O$_3$-coated TiO$_2$ DSC is more efficient than a conventional cell constructed with a bare TiO$_2$ nanoparticle film, with an increase in η from 6.54

148

to 7.26%. To deduce the reasons for this increase in efficiency, a discussion on the individual quantities contributing to the total device efficiency is required. From equation (6.2) it can be seen that these factors are I_{sc}, V_{oc} and the fill factor, FF. However, FF is given by the ratio of P_{max} and $I_{sc} V_{oc}$ and as such much of the discussion around I_{sc} and V_{oc} will also be related to the changes in FF.

It is noticeable from Figure 6.1 that the Al_2O_3-TiO_2 DSC has a greater I_{sc} compared to the bare TiO_2 cell. In Chapter 5.3 it was found that the Al_2O_3 coating increases dye adsorption onto the metal-oxide surface, thereby increasing the metal-to-ligand charge transfer (MLCT) within the N719 dye, as a result of the higher isoelectric point (IEP) of Al_2O_3 compared to TiO_2 [6.1, 6.2]. Furthermore, in Chapter 1.5 it was explained that the total incident-photon-current-conversion efficiency (IPCE) of the DSC is given by the product of the efficiencies for light harvesting (η_{lh}), electron injection from the dye to the TiO_2 conduction band (η_{ei}), electron transport through the TiO_2 nanostructured film (η_{et}) and electron collection at the TCO (η_{ec}), or mathematically

$$IPCE = \eta_{lh} \times \eta_{ei} \times \eta_{et} \times \eta_{ec} \qquad (6.3)$$

The short circuit current density serves as a measure of IPCE given in equation 6.3 [6.3]. The N719 dye molecule has the highest light harvesting efficiency of the commercial dyes, hence a very high η_{lh} [6.3]. The increased MLCT on the surface of the core-shell material leads to greater electron injection from the dye to the TiO_2 conduction band, thus the Al_2O_3 coated TiO_2 working electrodes have a greater η_{ei}. The electron collection efficiency, η_{ec},

at the FTO of the DSCs was increased by coating the FTO/glass substrates with a dense TiO_2 "blocking layer" in accordance with [6.4].
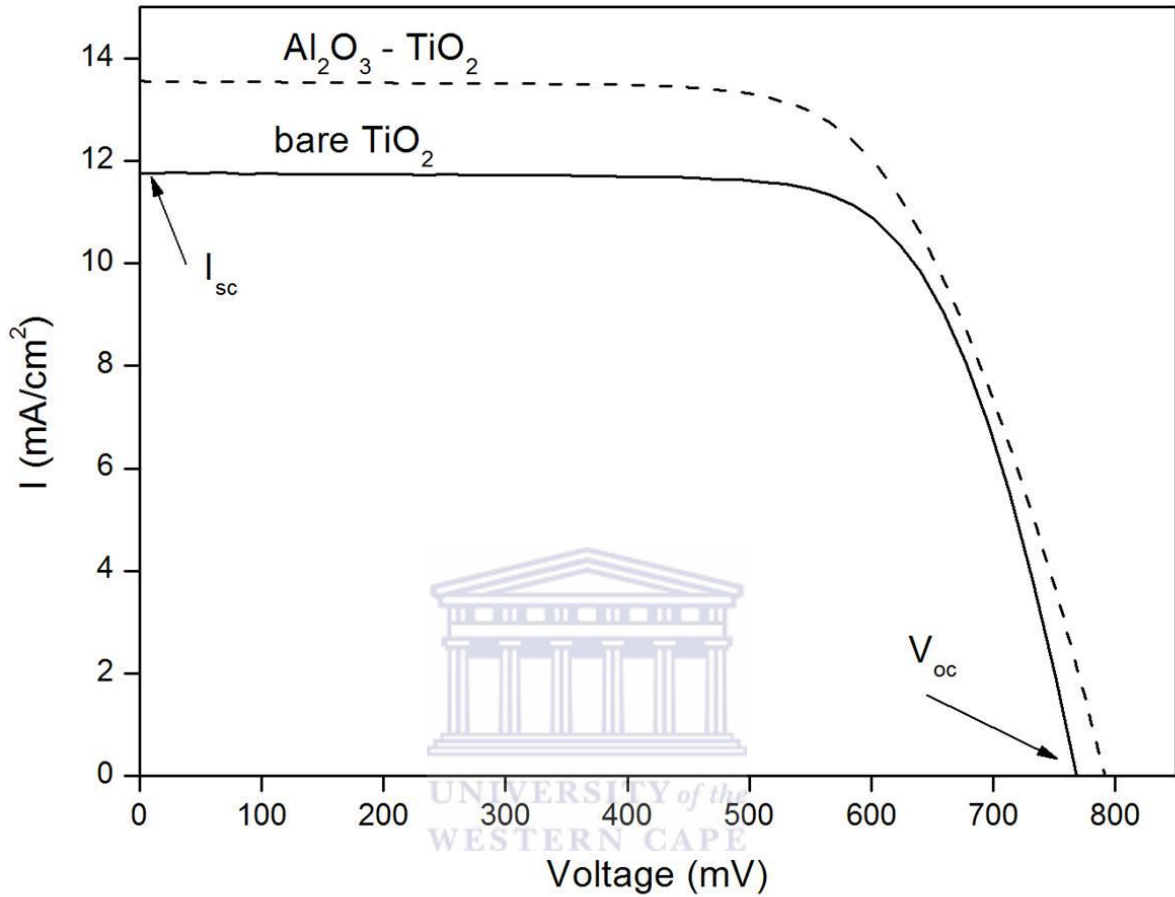
Cell	V_{oc} (mV)	I_{sc} (mA/cm²)	FF (%)	R_{series} (Ω)	R_{shunt} (kΩ)	V_{max} (mV)	I_{max} (mA)	P_{max} (mW)	η (%)
Bare TiO_2	768.448	11.755	72.41	20.8	0.966	603.0	4.458	2.688	6.54
Al_2O_3-TiO_2	791.109	13.557	67.64	24.3	5.73	584.0	5.28	3.083	7.26

Figure 6.1: I – V curves of DSCs incorporating bare and Al_2O_3 coated TiO_2 nanoparticles; the critical data obtained from the I – V curves are tabulated in the accompanying table.

The electron transport properties through the bare TiO_2 and Al_2O_3-TiO_2 films (i.e. η_{et}) will be discussed in conjunction with EIS plots and equivalent

circuits. However, based on the increased I_{sc} it is quite evident that an Al_2O_3 coated TiO_2 nanoparticle film produces a solar cell with greater electron generation and injection (or separation) properties than a DSC with bare TiO_2 as the working electrode. Similar results have been reported by various authors [6.5 – 6.7].

Figure 6.1 also shows that the coated TiO_2 DSC has a higher V_{oc} than a bare TiO_2 cell. O'Regan et al. [6.8] states that there are three ways in which a surface coating can cause an increase in the V_{oc} of a DSC. In the first instance, the insulating nature of the coating material implies that photo-injected electrons in the TiO_2 conduction band can only recombine with a positive charge in the electrolyte or hole conductor by tunneling through the insulator (shown in Figure 1.9). This is known as the "tunnel barrier" effect. The barrier causes a decrease in the "per electron" recombination rate constant for a given electron population. If, at 1 sun illumination, the flux of injected electrons from the dye is unchanged, then the electron concentration at V_{oc} will be higher for the cell with the coating. In Chapter 1.4 it was shown that V_{oc} is given by the difference between the Fermi energy level in the semiconductor film and the redox potential of the electrolyte. Hence, a larger electron concentration in the TiO_2 means a more negative Fermi level and thus a larger V_{oc}.

The second possible cause for an increase in the V_{oc} is known as the "surface dipole" effect and does not cause a decrease in the recombination rate constant. Instead, the surface coating changes the distribution of charge across the TiO_2/electrolyte interface relative to the uncoated TiO_2. If the coating results

in more negative charge closer to the TiO_2 surface and more positive charge closer to the electrolyte, then the resulting electric field will increase the band offset between the two materials. This charge redistribution will not directly cause a decrease in the recombination rate constant at V_{oc}, so there will be no change in the concentration of electrons in the TiO_2 at V_{oc}, instead the increased band offset is the source of the increase in V_{oc}.

In the third case the coating removes, or moves out of the optical bandgap of the TiO_2 , a significant fraction of the surface states at potentials near V_{oc} so that the total density of states at these potentials is reduced. This might directly reduce the recombination rate constant if recombination occurred through surface states. However, various authors have argued that there are strong indications that recombination is not limited by surface-state density, but rather by transport [6.9, 6.10]. Thus, no change in the recombination rate constant for this case can be expected as well. The population of electrons in the TiO_2 film at V_{oc} will stay unchanged, but the same 1 sun V_{oc} population of electrons will fill states closer to TiO_2 conduction band, resulting in a larger Fermi level offset and thus larger V_{oc}.

In Figure 6.1 it is quite evident that there is a marked difference in the shunt resistance of the two respective cells, with R_{shunt} of the Al_2O_3-TiO_2 DSC equal to 5.73 versus 0.966 kΩ for a TiO_2 cell. This is a strong indication that the recombination pathways within the cell have been reduced. Hence, at this stage the higher V_{oc} measured in an Al_2O_3-TiO_2 DSC appears to be as a result of a decrease in recombination during the tunnel barrier effect, rather than an off-set or adjustment of the bandgap of the TiO_2.

EIS was employed to investigate the charge transport and recombination phenomena leading to the different I – V characteristics observed for the two different types of DSCs; the respective spectra of which are plotted in Figure 6.2. Electron transfer within the DSC is coupled to electronic and ionic transport. In the dark under forward bias electrons are injected in the conduction band of the nanoparticles and their motion is coupled to that of I^-/I_3^- ions in electrolyte. Illumination gives rise to new redox processes at the TiO_2/dye/electrolyte interface comprising sensitised electron injection, recombination with the parent dye and regeneration of the sensitiser.

The EIS spectra presented in the following sections were recorded with a forward bias of 0.8 V under AM 1.5 illumination. In Figure 6.2 three distinctive features can be observed. From left to right the first semi-circle (at high frequencies) is representative of the electron transport at the FTO/TiO_2 interface at the working electrode, the intermediate semi-circle is indicative of the electron injection, transport and recombination with I_3^- at the TiO_2/dye/electrolyte interface, whereas the third semi-circle at low frequencies contains information about the I^-/I_3^- redox reactions at the Pt/FTO interface at the counter electrode [6.10].

The corresponding equivalent circuit of DSC is shown by the inset in Figure 6.2. From left to right, R_{FTO} is the series resistance offered by the FTO/glass substrate, and is connected in series to the parallel connected constant phase element (CPE1) and the charge transfer element R_{TiO2}, which are the double layer capacitance and charge transfer resistance at the TiO_2/dye/electrolyte interface, respectively.
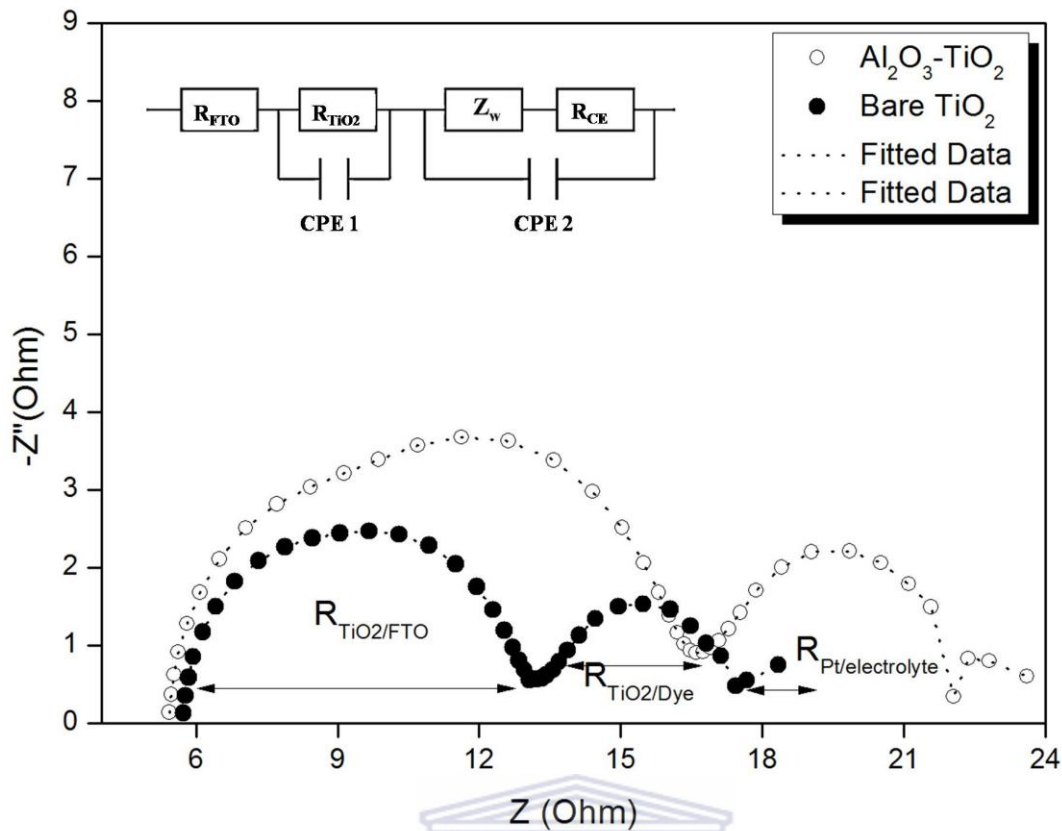
Figure 6.2: EIS spectra of the DSCs with bare TiO$_2$ and Al$_2$O$_3$ coated TiO$_2$ nanoparticle film as the electron carrier. The equivalent circuit configuration for a DSC [6.10].

The second Randles circuit in Figure 6.2 describes the diffusion of the tri-iodide in the electrolyte by means of the Warburg impedance element Z$_w$ that is connected in series to the charge transfer resistance at the platinum coated counter electrode (R$_{CE}$) and in parallel to the double layer capacitance element CPE2, which describes the charge build-up at the counter electrode. This equivalent circuit was adapted from the detailed description of a DSC under various conditions as reported in [6.10]. Table 6.1 tabulates the values obtained by fitting the equivalent circuit in Figure 6.1 to the measured EIS spectra for both types of cells. To compare the relative charge transfer resistances in the two cells, the values obtained from the equivalent circuit fits were divided by the

cell effective area, which was 0.359 cm^2 for the bare TiO$_2$ cell and 0.387 cm^2 for the Al$_2$O$_3$-TiO$_2$ cell. In addition, the electron recombination lifetime, τ_n in the TiO$_2$ films, as can be obtained from the frequency peak of the middle arc of the EIS spectrum for DSCs. This relationship is given by [6.11]

$$\text{electron lifetime} = \frac{1}{2\pi f} \qquad (6.4)$$

where f is the frequency of the peak of the intermediate semi-circle.

Table 6.1: Estimated circuit element values obtained from the fitted equivalent circuits in Figure 6.2

Cell	R$_{FTO}$ (Ω/cm^2)	CPE1 (μF)	R$_{TiO2}$ (Ω/cm^2)	Z$_w$ (mF)	R$_{CE}$ (Ω/cm^2)	CPE2 (F)	τ_n (ms)
Al$_2$O$_3$-TiO$_2$	14.65	102.89	12.07	23.91	1.09	1.01	13.05
Bare-TiO$_2$	13.57	119.29	15.46	18.35	3.90	0.60	9.42

As can be seen from Table 6.1 the electron recombination lifetime in the Al$_2$O$_3$ coated TiO$_2$ film is higher than the bare film, directly indicating a greater diffusion distance travelled prior to recombination. It can also be seen that there is a slight decrease in the charge transfer resistance (R$_{TiO2}$) when the TiO$_2$ film is coated with the layer of Al$_2$O$_3$, which is in agreement with the longer charge carrier lifetime. These results explain the higher V$_{oc}$ and R$_{shunt}$ values measured for an Al$_2$O$_3$-TiO$_2$ DSC versus a bare-TiO$_2$ cell in Figure 6.1 and proves that the electron recombination with nearby tri-iodide ions as well as oxidised parent dye molecules are reduced by the insulating overlayer. Thus the Al$_2$O$_3$ coating not only increases the dye adsorption properties of the TiO$_2$ film by increasing the MLCT characteristics of the film, but the coating also reduces recombination within the TiO$_2$ layer.

6.2 Application of Bare and Al$_2$O$_3$-Coated TiO$_2$ Nano-tubes in DSCs

Figure 6.3 plots the I – V curves for DSCs manufactured with a 15 μm thick layer of bare and Al$_2$O$_3$ coated TiO$_2$ nanotube arrays. As was found in the case of the nanoparticle films, it can be seen from Figure 6.3 that a layer of nanotubes coated with Al$_2$O$_3$ also produces a DSC with greater efficiency, with an increase from 4.56 to 4.88% measured. There is also a slight increase in I$_{sc}$ from 7.748 to 7.962 mA/cm^2 after coating the nanotube layer with the Al$_2$O$_3$.

In contrast to nanoparticle based DSCs, however, there is a slight decrease in the open circuit voltage after coating, from 821.551 to 811.814 mV. The shunt resistance, R$_{shunt}$ increases from 7.93 kΩ for a cell with a bare TiO$_2$ nanotube layer to 13.9 kΩ for a DSC with an Al$_2$O$_3$ coated TiO$_2$ nanotube layer. Furthermore it can also be seen that the series resistance, R$_{series}$ decreases and that the maximum power increases upon coating the nanotubes.

The increased short circuit current density upon coating suggests once more that the MLCT increased ion in the dye as a result of the alumina coating thereby inducing greater electron injection into the TiO$_2$ conduction band, in coherence with the UV-vis results obtained in Chapter 5. The negligible change in the open circuit voltage suggests good electron transport in both types of cells whereas the increase in shunt and decrease in series resistance upon coating imply a decrease in the electron-hole recombination at the complex interfaces within the Al$_2$O$_3$-TiO$_2$ nanotube DSC.

Cell	V_{oc} (mV)	I_{sc} (mA/cm²)	FF (%)	R_{series} (Ω)	R_{shunt} (kΩ)	V_{max} (mV)	I_{max} (mA)	P_{max} (mW)	η (%)
Bare TiO₂ NT	821.551	7.748	71.67	35.9	7.93	647.0	2.80	1.81	4.56
Al₂O₃-TiO₂ NT	811.814	7.962	75.56	22.2	13.9	658.0	3.70	2.44	4.88

Figure 6.3: I – V curves of DSCs incorporating bare and Al₂O₃ coated TiO₂ nanotubes

The EIS spectra of the respective nanotube based cells are plotted in Figure 6.4. The spectra were recorded at 1 sun (AM 1.5) illumination under forward bias of 0.8 V. Once more three distinctive arcs can be identified as a result of the FTO-TiO₂, TiO₂/dye/electrolyte and electrolyte/Pt/FTO interfaces, respectively. However, in the low frequency range, a straight line rather than a semi-circle is observed. The equivalent circuit fits are plotted in the inset of

Figure 6.4. For these spectra, purely capacitive circuit element, C1 and C2, provided a better fit, which is indicative of near perfect charge double layer build-up at the respective interfaces [6.11].
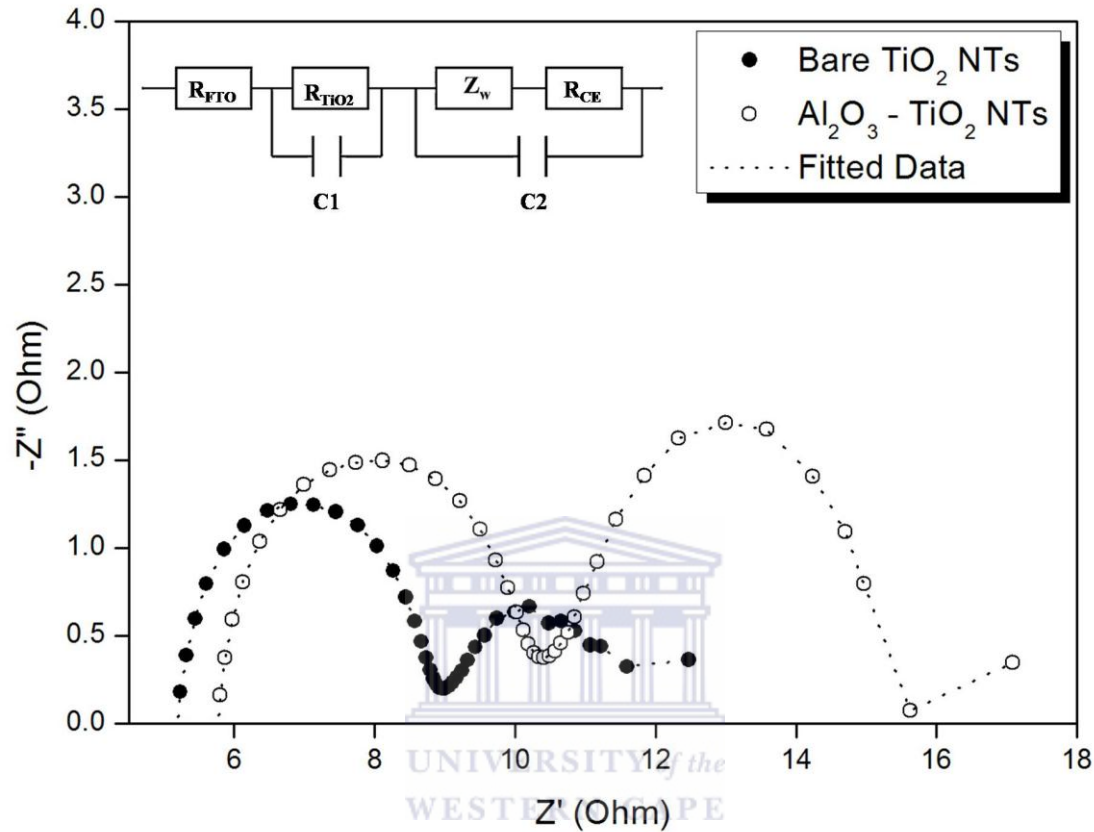
Figure 6.4:   EIS Spectra of the bare and Al_2O_3 coated TiO_2 nanotube DSCs along with the fitted equivalent circuit layout

The values obtained during the fitting of the different circuit elements are summarised in Table 6.2. Analysis of the charge transfer resistance, R_{TiO2} at the TiO_2/dye/electrolyte interface reveals a decrease upon coating with the Al_2O_3 insulating layer, similar to the case when coating the nanoparticle film. It can also be seen that there is an increase in the electron lifetime in during transport in the TiO_2 nanotube film upon coating. These results are in good agreement with the increase in R_{shunt}, as shown in Figure 6.3.

158

Table 6.2: Estimated circuit element values obtained from the fitted equivalent circuits in Figure 6.4

| Cell	R_{FTO} (Ω/cm²)	CPE1 (µF)	R_{TiO2} (Ω/cm²)	Z_w (mF)	R_{CE} (Ω/cm²)	CPE2 (F)	τ_n (ms)
Bare-TiO₂ NT	14.06	80.02	5.47	48.59	6.96	0.68	59.3
Al₂O₃-TiO₂ NT	13.95	122	12.07	22.31	4.29	1.59	82.4

6.3 Comparison between Nanotube and Nanoparticle Based DSCs

Figure 6.5 compares the I - V curves of all four types of DSCs, with the corresponding data plotted in the table inserted in Figure 6.5, where it can readily be seen that a nanoparticle based cell produces a greater current density than a nanotube based device. It is well reported that TiO_2 nanotube films suffer from low effective surface area for dye-adsorption compared to a layer of nanoparticles of size between 10 and 20 nm [6.12 – 6.14] and that this causes a decrease in the attainable photocurrents in the DSC.

In Chapter 5.3 it was found that the N719 dye adsorbed nanotube films absorb less radiation than the nanoparticle films, and subsequently had a lower MLCT character subsequently resulting in a poorer light harvesting. Shankar [6.15] showed that the light harvesting efficiency, η_{lh} in equation 6.2, is indeed directly proportional to the nanotube surface area and that longer length nanotubes produced greater efficiencies.
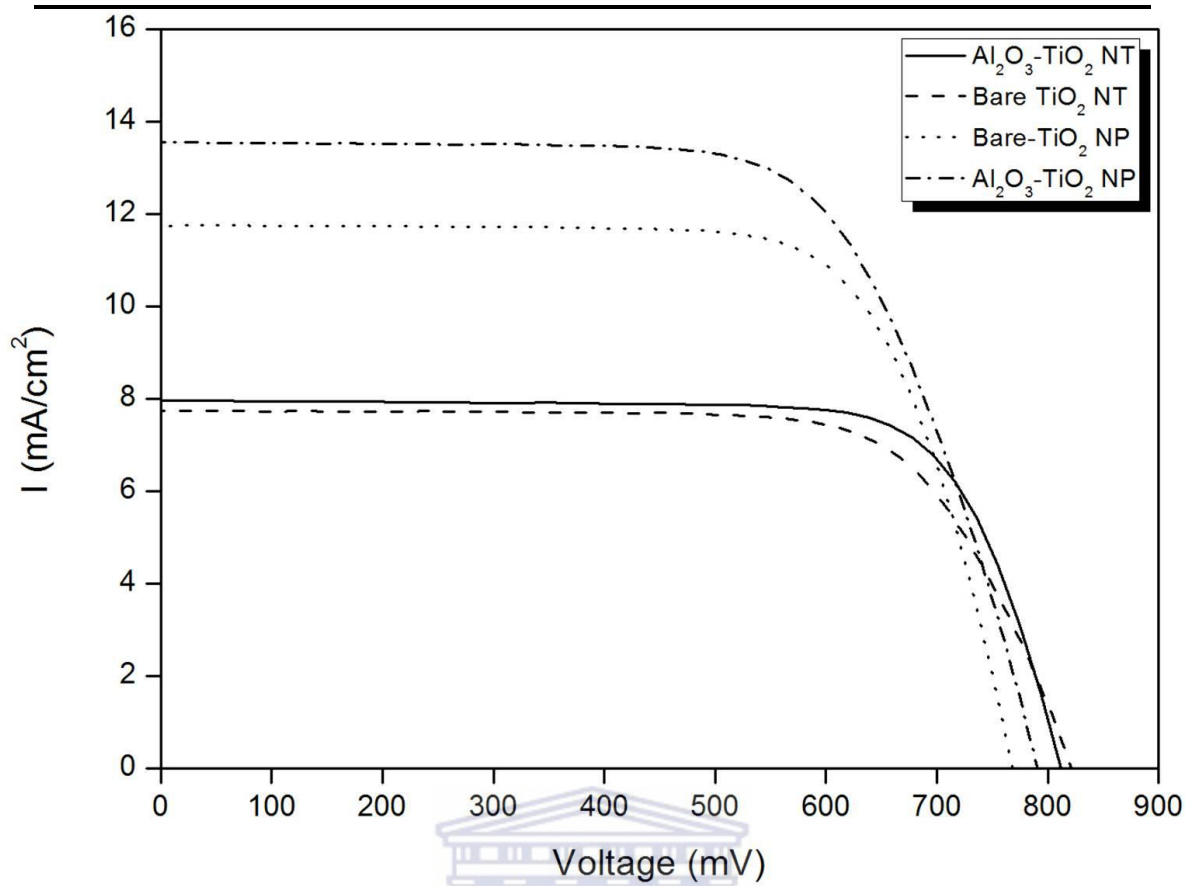
Cell	V_{oc} (mV)	I_{sc} (mA/cm²)	FF (%)	R_{series} (Ω)	R_{shunt} (kΩ)	V_{max} (mV)	I_{max} (mA)	P_{max} (mW)	η (%)
Bare TiO_2 NP	768.448	11.755	72.41	20.8	0.966	603.0	4.458	2.688	6.54
Al_2O_3-TiO_2 NPs	791.109	13.557	67.64	24.3	5.73	584.0	5.28	3.083	7.26
Bare TiO_2 NT	821.551	7.748	71.67	35.9	7.93	647.0	2.80	1.81	4.56
Al_2O_3-TiO_2 NT	811.814	7.962	75.56	22.2	13.9	658.0	3.70	2.44	4.88

Figure 6.5: Comparison of the I – V curves for the four different DSCs with the corresponding I – V data

Conversely, the open circuit voltages produced by nanotube based DSCs are greater than the nanoparticle equivalents, as shown in Figure 6.5 and fits well with the greater shunt currents measured for the different cells, suggesting

greater charge and mass transport within the nanotube based cells. Figure 6.6 shows the EIS spectra along with the values obtained for the different circuit elements of the equivalent circuit fits.
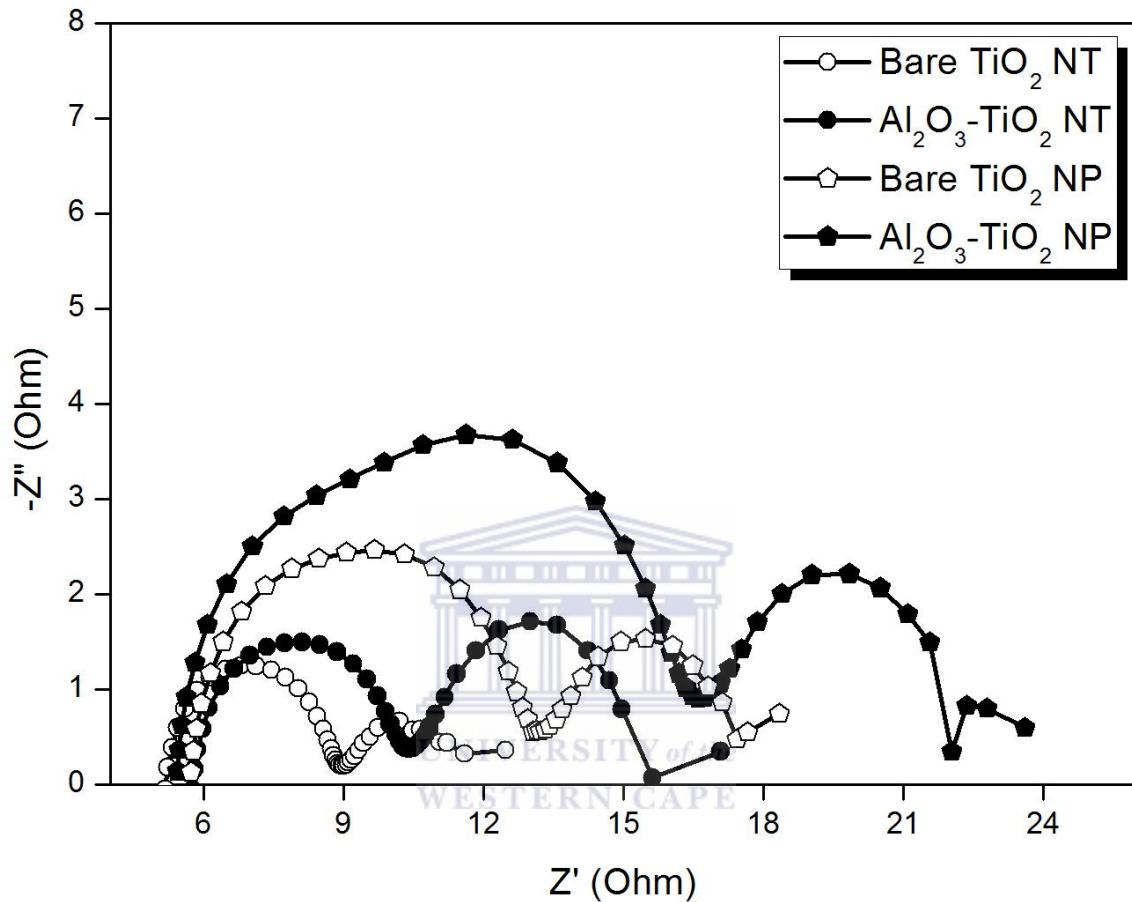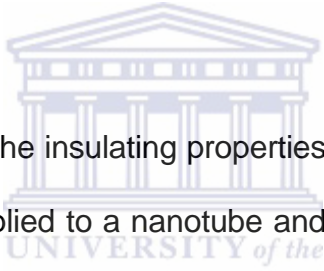
Cell	R_{FTO} (Ω/cm^2)	CPE1 (μF)	R_{TiO2} (Ω/cm^2)	Z_w (mF)	R_{CE} (Ω/cm^2)	CPE2 (F)	τ_n (ms)
Al_2O_3-TiO_2 NP	14.65	102.89	12.07	23.91	1.09	1.01	13.05
Bare-TiO_2 NP	13.57	119.29	15.46	18.35	3.90	0.60	9.42
Bare-TiO_2 NT	14.06	80.02	5.47	48.59	6.96	0.68	59.3
Al_2O_3-TiO_2 NT	13.95	122	12.07	22.31	4.29	1.59	82.4

Figure 6.6: EIS spectra of the four different cells with the values obtained for the circuit elements of the equivalent circuits

As can be seen in Figure 6.6, the electron lifetime in the TiO$_2$ nanotube films are significantly greater than is the case in the nanoparticle films. This serves as proof of the 1-D charge transport route provided by the nanotubes. In addition, it can also be seen that the lifetime is greater in the coated nanotubes compared to the uncoated nanotubes, which suggests that the coating acts as a charge suppresses the recombination pathways between the injected electron in the TiO$_2$ conduction band and the oxidised dye molecule, as well as between the TiO$_2$ and the electrolyte. As was previously shown, this fits well with the observed I-V curve data.

Conclusion

This work shows that the insulating properties of a core-shell nanoparticle structure can indeed be applied to a nanotube and that the concept is feasible for applying in a DSC. In fact, the results of Figures 6.1 to 6.6 suggests that the novel Al$_2$O$_3$-coated TiO$_2$ architecture has the potential to out-perform traditional nanoparticle based DSCs. However, for this to be overcome more work is required on the charge transport properties, in particular the relationship between the charge transport and the architecture (i.e. shape, length, crystal structure, etc.) of these arrays of nanotubes. A major obstacle encountered during this study has been the absence of incident-photon-current conversion efficiency (IPCE), photo-voltage and photo-current decay, intensity modulated photocurrent (IMPS) and photovoltage spectroscopy (IMVS) facilities and will form part of future studies in the characterisation of these novel DSCs.

References

[6.1]   E. Palomares, J.N. Clifford, S.A. Haque, T. Lutz, J.R. Durrant, J. Am. Chem. Soc. 125 (2003) 475

[6.2]   P. Qu, G.J. Meyer, Langmuir 17 (2001) 6720

[6.3]   M.K. Nazeeruddin, P. Pechy, T. Renouard, S.M. Zakeeruddin, R. Humphry-Baker, P. Comte, *et al.*, J. Am. Chem. Soc. 123 (2001) 1613

[6.4]   B. Yoo, K.-J. Kim, S.-Y. Bang, M.J. Ko, K. Kim and N.-G. Park, J. Electroanal. Chem. 638 (2010) 161

[6.5]   S. Wu, H. Han, Q. Tai, *et al.*, J. Power Sources 182 (2008) 119

[6.6]   X.-T. Zhang, I. Sutanto, T. Taguchi, *et al.*, Sol. Energy Mat. Sol. Cells 80 (2003) 315

[6.7]   V. Ganapathy, B. Karunagaran and S.-W. Rhee, J. Power Sources 195 (2010) 5138

[6.8]   B.C. O'Regan, S. Scully, A.C. Mayer, E. Palomares and J. Durrant, J. Phys. Chem. B 109 (2005) 4616

[6.9]   J. Nelson, S.A. Haque, D.R. Klug and J.R. Durrant, Phys. Rev. B: Condens. Matter Mater. Phys. 6320 (2001) 5321

[6.10] Q. Wang, J.-E. Moser and M. Grätzel, J. Phys. Chem. B 109 (2005) 14945

[6.11] J. Bisquert, F. Fabregat-Santiago, I. Mora-Seró, G. Garcia-Belmonte and S. Giménez, J. Phys. Chem. C 113 (2009) 17278

[6.12] M. Paulose, K. Shankar, O.K. Varghese, G.K. Mor and C.A. Grimes, J. Phys. D: Appl. Phys. 39 (2006) 2498

[6.13] H. Park, W.-R. Kim, H.-T. Jeong, J.-J. Lee, H.-G. Kim and W.-Y. Choi, Sol.Energy.Mater.Sol.Cells(2010),doi:10.1016/j.solmat.2010.02.017

[6.14] I.C. Flores, J.N. De Freitas, C. Longo, *et. al.*, J. Photochem. Photobio. A: Chem. 189 (2007) 153

[6.15] K. Shankar, "*Effects of Architecture and Doping on the Photoelectrochemical Properties of Titania Nanotubes*" Ph.D. Thesis, Pennsylvania State University, USA (2007)

SUMMARY

TiO$_2$ nanotubes offer a one-dimensional (1-D) transport route for generated electrons in the dye-sensitised solar cell (DSC), thereby offering a potential solution to high rates of recombination between the electrons and nearby holes within the cell. The high recombination rates result in low efficient DSCs, with the best reported efficiencies in and around 11%. This study explored the use of a novel, modified nanotube architecture, which comprised of Al$_2$O$_3$ coated TiO$_2$ nanotubes in the DSC. It is hypothesised that the insulating properties of the alumina combined with the 1-D properties of the nanotubes reduce the recombination at the interface between TiO$_2$, dye and electrolyte, while also increasing the electron lifetime within the DSC. The study was structured as follow:
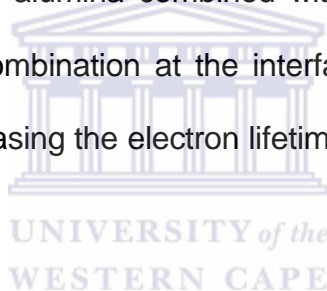
A.   Optimisation of the anodisation process for the synthesis of arrays of TiO$_2$ nanotubes

The TiO$_2$ nanotubes were synthesised by means of electrochemical anodisation, as described in detail in Chapter Two. In Chapter Three the anodisation bath conditions were optimised to synthesise TiO$_2$ nanotube arrays with an average length of 15 µm, diameter of 50 nm and wall thickness of 15 nm. The optimised anodisation bath parameters consisted of an anodisation voltage of 60 V, neutral organic electrolyte consisting of 2 M H$_2$O + 0.15 M NH$_4$F + ethylene glycol (EG) and an anodisation time of 6 hours. The anodisation voltage was increased increased from 5 to 60 V and it was found

by means of scanning electron microscopy (SEM) analysis that the nanotube diameter, wall thickness and length linearly increased with an increase in voltage. The F$^-$ ion concentration was varied from 0.15 to 1 mol/l by increasing the concentration of NH$_4$F in the electrolyte bath. This resulted in an increase in the nanotube diameter.

X-ray diffraction (XRD) patterns revealed that the as-anodised nanotubes were amorphous and as such were annealed at 450 °C for 2 hours in air at atmospheric pressure. This yielded crystalline anatase TiO$_2$ nanotubes and it was found that the crystallinity of the nanotubes are dependent on physical structure of the nanotubes, in particular the nanotube wall thickness and hexagonally shaped bottom.

It was also found by means of photoluminescence spectroscopy that the optical properties, especially the bandgap of the TiO$_2$ nanotubes are dependent the crystallinity, which in turn was dependent on the structural characteristics, such as the wall thickness, diameter and length. The PL measurements were supplemented by Raman spectra, which revealed an increased in the quantum confinement of the optical phonon modes of the nanotubes synthesised at low anodisation voltages, consequently yielding a larger bandgap.

B.   Synthesis of the Al$_2$O$_3$-coated TiO$_2$ nanotubes

Chapter Five investigated the morphology, crystallinity and dye-adsorption properties of core-shell Al$_2$O$_3$-coated TiO$_2$ nanotubes. A simple synthesis protocol was followed based on previous work done on films of TiO$_2$ nanoparticles, as detailed in Chapter Two. Atomic force microscopy (AFM)

micrographs showed that the average particle size of a film of TiO_2 nanoparticles increases after coating with the Al_2O_3. Similarly it was found via AFM that the average nanotube diameter increased post sol-gel deposition, and served as the first indications that the nanotubes indeed are coated with a layer of Al_2O_3.

High resolution transmission electron microscopy (HR-TEM), coupled with selected area electron diffraction (SAED) and XRD analyses confirmed the coating of the nanotube walls with a thin layer of amorphous Al_2O_3 with a thickness between 4 and 7 nm. To the best of our knowledge and based on published literature, this is the first time that a simple sol-gel dip-coating process has been successfully applied to uniformly coat anodised TiO_2 nanotube layers. In addition, ultraviolet-visible (UV-vis) absorbance spectra showed that the dye-adsorption ability of the nanotubes are enhanced by the Al_2O_3 coating and hence is a viable material for solar cell application.

C. Application of Al_2O_3-coated TiO_2 nanotubes in the DSC

Chapter Six investigated the photovoltaic and electrochemical properties of DSCs employing bare and Al_2O_3-coated TiO_2 nanotubes. Photocurrent – voltage (I – V) measurements showed that a DSC fabricated with a 15 μm thick layer of bare TiO_2 nanotubes has a photon-to-light conversion efficiency of 4.56%, which increased to 4.88% after coating the nanotubes with a layer of alumina. However, these devices had poorer conversion efficiencies than bare TiO_2 and Al_2O_3-coated TiO_2 nanoparticle based DSCs, which boasted with efficiencies of 6.54 and 7.26%, respectively. The low efficiencies of the TiO_2

167

nanotube based DSCs are ascribed to the low surface area of the layer of nanotubes, which yielded low photocurrent densities. Electrochemical impedance spectroscopy (EIS) showed that the electron lifetime in the alumina coated nanotubes are almost 20 times greater than in a bare layer of nanoparticles. In addition, it was also found that the charge transfer resistance at the interface of the TiO_2/dye/electrolyte is the lowest for an Al_2O_3-coated TiO_2 layer.

As future work, the charge transport mechanisms in the novel coated nanotube structures should be investigate by means of incident-photon-current conversion efficiency (IPCE), photo-voltage and photo-current decay, intensity modulated photocurrent (IMPS) and photovoltage spectroscopy (IMVS).
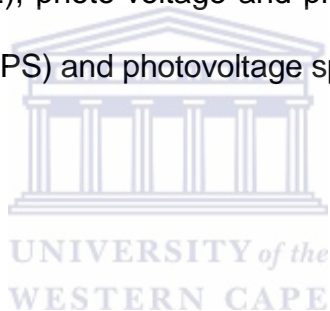
APPENDIX

List of relevant publications, proceedings, oral and poster presentations

PUBLICATIONS

F. R. Cummings, L. J. Le Roux, M. K. Mathe and D. Knoesen, "*Structure-Induced Optical Properties of Anodized TiO$_2$ Nanotubes*" Materials Chemistry and Physics 124 (2010) 234

Franscious Cummings, Lukas le Roux, Nomthandazo Mutangwa and Dirk Knoesen, "*Low-cost transparent solar cells: Potential of titanium dioxide nanotubes in the improvement of these next generation solar cells*", Proceedings from Science Real and Relevant: The CSIR Biennial Conference, Pretoria, South Africa, 31 August – 01 September 2010 (http://researchspace.csir.co.za/dspace/handle/10204/4508)

F. R. Cummings, L. J. Le Roux, N. J. Mutangwa and D. Knoesen, "*Investigation of the photovoltaic performance of dye-sensitised solar cells employing TiO$_2$ nanotubes*" Proceedings from the 55th Annual South African Institute of Physics Conference, Pretoria South Africa, 27 September - 1 October 2010

F.R. Cummings, L. J. Le Roux and D. Knoesen, "Application of TiO$_2$ nanotube arrays in dye-sensitised solar cells", Proceedings from the 49th Annual Microscopy Society of South Africa Conference, Pretoria South Africa, 5 – 9 December 2011

L. J. Le Roux, S. Hietkamp and F. R. Cummings, "*Dye-Solar Cells: A Different Approach to Solar Energy*" Proceedings from Science Real and Relevant: The 2nd CSIR Biennial Conference, Pretoria, South Africa, 17-18 November 2008, p5 (ISBN: 978-0-7988-5573-0)

PRESENTATIONS

F. R. Cummings, "Dye Solar Cell Research", 27 November 2009, http://researchspace.csir.co.za/dspace/simple-search?query=cummings

F. R. Cummings, "Dye Solar Cell Research", 13 November 2009, http://researchspace.csir.co.za/dspace/simple-search?query=cummings

F. R. Cummings, L. J. Le Roux and N. J. Mutangwa, "*TiO$_2$ nanotube-based dye solar cell research in South Africa*" The 4th Korea-South Africa Joint Workshop on Nanotechnology, 21 October 2009, Korea Institute of Science and Technology, Seoul South Korea
 (http://researchspace.csir.co.za/dspace/simple-search?query=cummings)

F. R. Cummings, "*Mechanistic Formation of TiO$_2$ Nanotubes via Anodisation – Effect of Operating Voltage and Time*", South African Institute of Physics (SAIP) 53nd Annual Conference, 11-13 July 2008, University of Limpopo, Polokwane, South Africa

PUBLICATIONS REVIEWED

Invited reviewer: Materials, Chemistry and Physics, "*Photodegradation of indigo carmine and recyclability of a novel TiO$_2$-strewn rubber sheet*" Manuscript No. MATCHEMPHYS-D-10-02415

Invited reviewer: Materials Science and Engineering B, "*Quasi-gel-state Ionic Liquid Electrolyte with Alkyl-pyrazolium Iodide for Dye-Sensitized Solar*", Manuscript No. MSB-D-10-01385